Advancing Supercapacitive Swing Adsorption of Carbon Dioxide through Electrode Design, Charging Protocols, and Oxygen Stability Studies

Citation

Bilal, Muhammad. *Advancing Supercapacitive Swing Adsorption of Carbon Dioxide through Electrode Design, Charging Protocols, and Oxygen Stability Studies*. 2024, https://preserve.lehigh.edu/lehigh-scholarship/graduate-publications-theses-dissertations/theses-dissertations/advancing.

Advancing Supercapacitive Swing Adsorption of Carbon Dioxide through Electrode Design, Charging Protocols, and Oxygen Stability Studies

by

Muhammad Bilal

A Dissertation

Presented to the Graduate and Research Committee

of Lehigh University

in Candidacy for the Degree of

Doctor of Philosophy

in

Chemistry

Lehigh University

May 2024

Dissertation is accepted and approved in partial fulfillment of the requirements for the PhD in Chemistry

Muhammad Bilal

April 24th, 2024
____
Defense Date

____
Dissertation Director
Kai Landskron, Ph.D.

____
Approved Date

Committee Members:

____
Kai Landskron, Ph.D.

____
Elizabeth Young, Ph.D.

____
Xiaoji Xu, Ph.D.

____
Mayuresh Kothare, Ph.D.

ACKNOWLEDGMENTS

I would like to thank Professor Kai Landskron for his continuous mentorship and support. I feel lucky to be able to spend a good part of my life doing research under his supervision. Our curious discussions on the scientific and technological aspects of supercapacitive swing adsorption were intellectually satisfying. I liked Professor Landskron's way of approaching a research problem through first principles thinking and seeing new opportunities in research problems. I had the chance to learn from him and apply the first principles thinking method during my research. I feel that switching disciplines (from chemical engineering to materials science to chemistry) and working with Professor Kai Landskron on multidisciplinary projects is the best thing I could experience to broaden my thinking perspective and be able to see things in many different ways.

I am highly grateful to my lab mate Jiajie Li for guiding me through experimental procedure and introducing the research on supercapacitive swing adsorption when I initially started the work after my fuel cell project had to be suddenly stopped. I am grateful to my friend Hao Guo from the chemical engineering department of Lehigh who taught me how to find surface area and porosity of materials. I had in-depth and insightful discussions on different research problems with my friends Daniyal Kiani (Director's fellow, NREL), Muhammad Imran (Humboldt postdoctoral fellow), and Yayati Naresh (Postdoctoral at Hokkaido).

Special thanks to my thesis committee members (Professor Elizabeth Young, Professor Xiaoji Xu, and Professor Mayuresh Kothare) for the insightful questions and valuable feedback.

I am indebted to my parents, siblings, and other relatives whose encouragement and support helped me the most during times of stress and low energy.

TABLE OF CONTENTS

List of Figures

List of Tables

ABSTRACT

The escalating levels of anthropogenic carbon dioxide in the atmosphere poses a significant challenge for our society. To address this challenge, it is imperative to swiftly develop efficient technologies that can capture and concentrate CO_2 from dilute sources in a cost-effective, environmentally friendly, and energy-efficient manner. Current strategies for carbon capture and concentration have several limitations, including sorbent toxicity, energy intensive thermal and/or pressure swings, poor cyclability, selectivity, and capacity retention. These issues are mainly due to thermal degradation, volatility, and the reactivity of sorbent materials with oxygen. To address these issues, supercapacitive swing adsorption (SSA) of CO_2 is of particular interest. SSA is an electrochemical carbon capture technology capable of capturing and concentrating CO_2 from a gas mixture upon charging and discharging of the electrodes. SSA offers significant advantages over existing carbon capture methods, including high selectivity, longer sorbent lifetime, faster charge/discharge cycles, high round-trip energy efficiency, and the use of inexpensive and environmentally benign materials. However, the CO_2 adsorption capacity of SSA reported prior to the research presented in this thesis was less than 100 $mmol.kg^{-1}$, at least one order of magnitude lower than competing carbon capture technologies. Moreover, the energetic and adsorptive performance of SSA was only investigated with 15% CO_2/85% N_2 gas mixtures, and the influence of oxygen, a major component of flue gas and air, was not known. Advancing SSA technology required the development and investigation of new materials with greatly improved CO_2 adsorption capacities, in-depth understanding of the factors necessary for performance improvements, understanding SSA performance

under different voltage windows, and monitoring SSA performance under oxygen environments.

This thesis discusses the development and characterization of new biomass and non-biomass-derived activated carbon electrodes for improved supercapacitive swing adsorption of carbon dioxide under different voltage windows with oxygen and without the presence of oxygen in the CO_2/N_2 gas mixture. Chapter 1 provides an overview of the increasing need to develop energy efficient and cost-effective CO_2 capture technologies, existing carbon capture methods (non-electrochemical and electrochemical), challenges with existing carbon capture methods, the history of supercapacitors and supercapacitive swing adsorption, and the outline of this thesis. Chapter 2 covers the fundamental principles of different physicochemical and electrochemical characterization techniques used in this research to investigate and compare the surface area, porosity, surface functionalities, capacitances, and resistances of different types of carbons. Chapter 3 reports six different types of activated carbons derived from biomass, coal, coke, and carbide sources, and provides the relationship between higher capacitance and improved CO_2 sorption capacities. Chapter 4 covers a simple, one-step synthesis procedure to prepare garlic roots derived activated carbons and investigates SSA at higher voltage windows. Chapter 5 reports the critical role of oxygen on the energetics and adsorptive performance of SSA. Chapter 6 provides the outlook and future directions to further advance SSA towards commercialization.

CHAPTER 1: INTRODUCTION

1.1 CO_2 Emissions and Global Temperature

Nineteen of the hottest years on record occurred in the last 20 years. Figure 1-1a shows the overview of earth captured by NASA from the year 1974-1978 and from the year 2017-2021. Rapidly increasing industrialization and growing population during the last five decades have resulted in an approximately 100 ppm increase in anthropogenic CO_2 emissions in the atmosphere. The positive correlation between rising CO_2 emissions and increasing global temperature was first predicted in 1896 by Swedish scientist Svante Arrhenius.[1] The monitoring of carbon dioxide (CO_2) concentrations in the atmosphere began several decades ago, with some of the earliest measurements dating back to the late 1950s.[2] Charles David Keeling, an American scientist, started the first continuous measurements of atmospheric CO_2 at the Mauna Loa Observatory in Hawaii in 1958. Since then, numerous international collaborations and initiatives have emerged to monitor CO_2 concentrations globally, involving organizations such as National Aeronautics and Space Administration (NASA), National Oceanic and Atmospheric Administration (NOAA), the European Space Agency (ESA), and others.

Figure 1-1b shows the graphical relationship between global temperature and CO_2 concentration. Currently, human activities release about 40 billion tons CO_2 each year.[3] It is expected that CO_2 concentrations can reach from current values of ~420 ppm to ~570 ppm in 2050 if the rate of increase stay the same, which can result in well above 2^{o}C increase of earth's temperature above pre-industrial levels. This could greatly threaten natural habitats, ecosystems, and all forms of life on earth.[4,5]

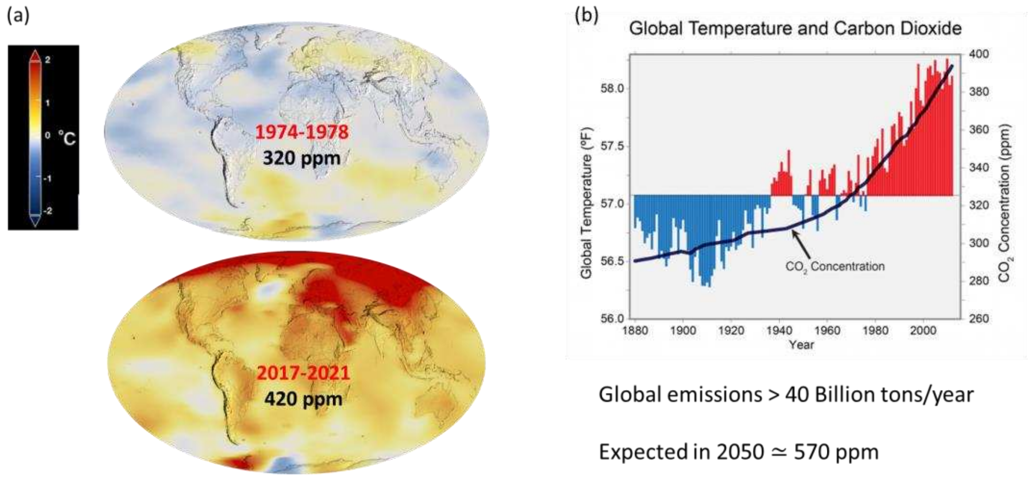

Global emissions > 40 Billion tons/year

Expected in 2050 ≃ 570 ppm

Figure 1-1 Relationship between rising CO_2 emissions and increased global temperature. (a) Overview of the earth captured by NASA from showing 100 ppm increase in atmospheric CO_2 concentrations within last five decades. (b) Graph showing rapid increase in global temperature and rising CO_2 concentrations. Data taken from NASA climate change website (https://climate.nasa.gov/climate_resources/139/video-global-warming-from-1880-to-2021/), accessed 2023-07-05.

The transition from fossil fuel powered energy to renewable, carbon-neutral energy is currently not fast enough to achieve these targets. Theres is an urgent need to develop efficient and scalable carbon capture technologies to capture CO_2 from industrial power plants and directly from the air. Figure 1-2 shows that the integration of negative-emission technologies must occur concurrently with zero-carbon technologies to achieve the ambitious targets set by IPPC.

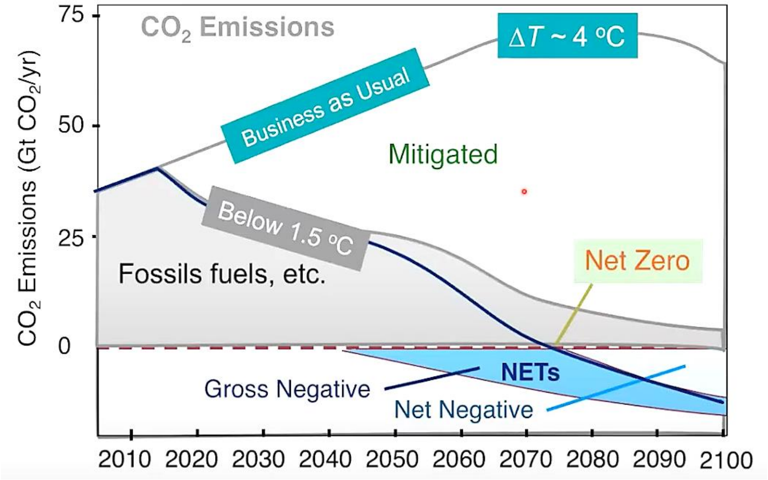

Figure 1-2 Guide to net negative emissions. The graph shows the transition from fossil fuels to renewable energy resources along with increasing deployment of carbon capture technologies is essential to achieve net negative emissions.[6]

1.2 CO_2 capture from point sources and the atmosphere

Point sources include CO_2 emissions from concentrated sources like cement industries, coal and natural gas fired power plants, and contribute around 58% towards total emissions.[7] The remaining 42% emissions come from decentralized sources like transportation, small-scale industrial processes, and agricultural activities, and contain much smaller concentrations of CO_2 (0.04-0.4%). The minimum thermodynamic work required to separate CO_2 from a gas mixture can be calculated from the equation:

$$\Delta G = -RT.ln(P_{CO2}/P_o)$$

where R is the gas constant (8.314 $J \cdot mol^{-1}K^{-1}$), T is the absolute temperature (K), P_{CO2} is the partial pressure of CO_2 in the feed gas mixture, and P_o is the pressure of the CO_2 in the concentrated gas. According to the Gibbs free energy relation, the thermodynamic minimum work necessary to separate a 15% CO_2 gas stream into pure CO_2 at room temperature and ambient pressure is around 5 kJ per mole. For separating CO_2 from gas mixture containing only 0.04% or 400 ppm CO_2, the minimum thermodynamic work required is around 22 kJ/mol. However, most commercial carbon capture technologies have high energy demands (>100kJ/mol) due to the enthalpic and entropic losses associated with the process and involve the use of toxic and corrosive chemicals. Figure 1-3 shows the technological requirements to develop an efficient carbon capture technology. The next section will provide a brief description of the existing carbon capture methods, some of which are already commercialized, and some are at different technological readiness levels.

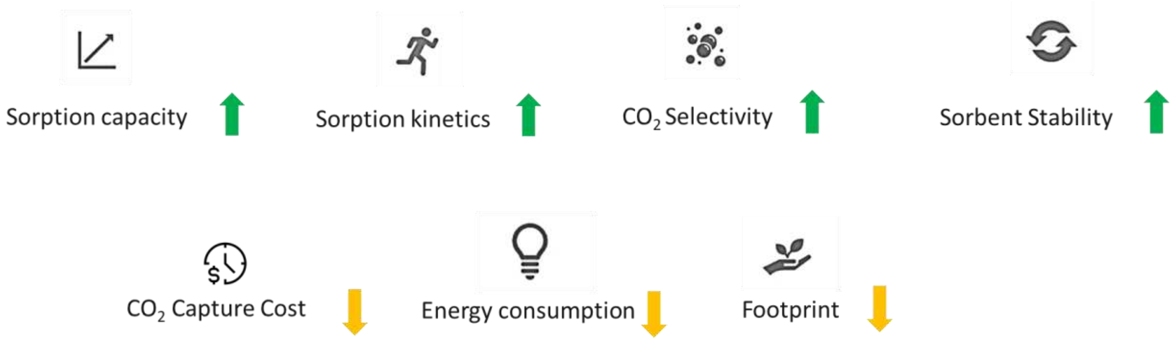

Figure 1-3 Carbon capture technology requirements

1.3 Conventional (Non-Electrochemical) CO_2 Capture Methods

Conventional CO_2 capture methods use temperature or pressure swings to capture and release CO_2 using liquid solvents or solid sorbents. The most common sorbent materials are supported amines.[8] Zeolites, porous carbons, and metal organic frameworks have also been used.[9] During temperature swing adsorption (TSA) or pressure swing adsorption (PSA), a gas mixture containing CO_2 is exposed to the sorbent. Depending upon the type of sorbent, CO_2 is either physiosorbed or chemisorbed to the sorbent at low temperature or high pressure. The sorbed CO_2 is released in concentrated form at high temperature or low pressure. Energy-intensive temperature or pressure gradients are a major challenge associated with these techniques. Moisture swing sorption is another important non-electrochemical CO_2 capture technique that uses anion exchange resin to capture and release CO_2 in dry and wet conditions. The technique is weather sensitive and performs best in hot and dry climates.

CO_2 capture in amines and alkalis using TSA/PSA has already been commercially used by few companies. A brief description of these processes is provided below.

1.3.1 Aqueous and supported amines for CO_2 capture

CO_2 capture using aqueous amine absorption or supported amine adsorption can occur via carbamate/protonated amine pairs or bicarbonate formation depending on the type of amine. The typical reactions involve carbamate formation, where one CO_2 molecule reacts with two amine groups to form carbamate ($2R_1R_2NH + CO_2 \leftrightarrow R_1R_2NH_2^+R_1R_2NCO_2^-$, where R is an alkyl or aryl group), for primary and secondary amines, and bicarbonate formation ($R_1R_2R_3N + H_2O + CO_2 \leftrightarrow R_1R_2R_3NH^+\ HCO_3^-$), which occurs across all amine types. Amines typically exhibit high heats of reaction, ranging from approximately 60 to 90 kilojoules per mole.

Carbon capture using aqueous alkanolamines and alkanamines is the most mature technology and was first patented in the 1930s.[10] It's use for removing CO_2 from various sources such as coal power plants and natural gas facilities is currently emerging. There are several pilot and demonstration projects in operation, including Boundary Dam in Canada and Petra Nova in the USA, which are among the largest coal-fired power plants utilizing amine-based post-combustion capture. These projects aim to capture around 3000-5000 tons CO_2 per day.[11]

An alternative to using aqueous amine solutions is employing supported amines.[12] Supported amines can be utilized in membranes and do not require bulk water, which eliminates the need for a component of regeneration energy. Moreover, solids have a lower heat capacity compared to liquids, leading to reduced energy input for thermal regeneration and resulting in a lower regeneration temperature. Supported amines can be attached to various materials such as carbon, metal-organic frameworks (MOFs), zeolites, polymers, alumina, and silica.[13] Regeneration of supported amines is commonly achieved by thermal methods above approximately 75°C. Due to the poisoning effect of flue gas contaminants (SO_x and NO_x) and the non-volatility of solid adsorbents, supported amines may be better suited for Direct Air Capture (DAC).[11,14] Several companies, including Climeworks in Switzerland and Global Thermostat in the USA, utilize solid amine technologies. The current energy requirements for DAC, averaged across companies, include approximately 30-40 kJ of electrical energy per mole for blowers and controls, and approximately 200-300 kJ of thermal energy per mole (equivalent to 4.5-6.8 GJ per metric ton of CO_2) for the regeneration of the solid sorbent using steam or low-grade waste heat.[15] In flue gas conditions, typical regeneration duties range from approximately 100-150 kJ of thermal energy per mole.[16]

1.3.2 Aqueous and solid alkalis for CO_2 capture

Since the 1950s, hot potassium carbonate solutions have served as an alternative to amine scrubbing for treating process gases.[17] When potassium carbonate reacts with water, it captures CO_2 to form potassium bicarbonate according to the equation: $K_2CO_3 + H_2O + CO_2 \leftrightarrow 2KHCO_3$. A pressure swing method is employed to regenerate the carbonate. Alkaline carbonates offer advantages over amines in carbon capture technology, with lower toxicity and improved resistance to flue gas contaminants.[11] However, K_2CO_3 exhibits slow reaction kinetics, necessitating the use of rate promoters like amines to maintain manageable absorber unit sizes. Regeneration duties for K_2CO_3 are comparable to or slightly higher than those for amines, ranging from approximately 130 to 220 $kJ.mol^{-1}$ (~3-5 $GJ.t_{CO2}^{-1}$).[17]

Aqueous hydroxide solutions are also used to convert CO_2 into carbonates ($2KOH + CO_2 \leftrightarrow H_2O+K_2CO_3$) and exhibit significant resistance to flue gas contaminants.[18] Following capture, the regeneration and release of CO_2 involve three steps: (a) adding $Ca(OH)_2$ to K_2CO_3 to regenerate KOH and produce solid $CaCO_3$, (b) heating $CaCO_3$ at ~900 °C to yield CaO and release CO_2, and (c) regenerating $Ca(OH)_2$ by mixing CaO with water. Carbon Engineering, operating a DAC commercial plant in Canada with a capacity of 1 Mt-CO_2 per year, published a detailed report on this process.[19] For partial CO_2 capture from air and release at 1 bar, their facility requires 230 $kJ.mol^{-1}$ of heat from natural gas and 12 $kJ.mol^{-1}$ from electricity. Drawbacks of this method include water loss and the reliance on high-grade heat obtained through fuel combustion.

Although continued improvements in amines and alkali-based carbon capture processes is desirable, the need for high temperatures, toxicity of components, poor cyclability, and capacity fade due to thermal degradation cannot be completely avoided. Electrochemical methods for CO_2 capture, on the other hand, do not require high temperatures and offer potentially higher energy efficiency than conventional (non-electrochemical) methods. A brief history and recent developments on electrochemical CO_2 capture methods is discussed in the next section.

1.4 Electrochemical CO_2 Capture Methods

Electrochemical CO_2 capture (ECC) methods use electricity to facilitate CO_2 separation at ambient temperature and pressure. The first demonstration on ECC dates back to 1969 when Huebscher and Babinsky aimed to develop a method for separating carbon dioxide for life support systems in submarines, and for space travel.[20] In their two stage electrochemical cell setup, stage 1 consisted of a carbonation cell, where a CO_2-rich air stream (0.6% CO_2) is directed to the cathode. At the cathode, both CO_2 and oxygen (O_2) are removed (reactions shown in Scheme 1), yielding a concentrated mixture consisting of 66.7% CO_2 and 33.3% O_2 at the anode. The second stage was used for oxygen reduction and high-purity CO_2 separation. The cell was operated at around 65°C and used $\geq$ 1V each for stage 1 and stage 2, resulting in high energy consumption.

Scheme 1.1 *Reactions shown in Huebscher and Babinsky low temperature carbonation cell*

Cathodic Reactions	Anodic Reactions
$O_2 + 2H_2O + 4e^- \rightarrow 4OH^-$	$4OH^- \rightarrow O_2 + 2H_2O + 4e^-$
$CO_2 + OH^- \rightarrow HCO_3^-$	$CO_3^{2-} + H_2O \rightarrow HCO_3^- + OH^-$
$HCO_3^- + OH^- \rightarrow CO_3^{2-} + H_2O$	$HCO_3^- \rightarrow CO_2 + OH^-$

Following the first report on ECC, Wynveen and Quattrone pioneered the use of an ambient-temperature electrochemical Carbon Capture system for aircraft in 1971.[21] Winnick et al. explored this system's potential for oxygen (O_2) regeneration in manned space. Wynveen and Quattrone's technology comprised electrochemical cells operating continuously in series, each employing an aqueous cesium carbonate (Cs_2CO_3) electrolyte. The electrodes, constructed from fine mesh coated with Teflon and platinum, formed porous platinum electrodes. Similar to a fuel cell setup, the cathode and anode were separated by the electrolyte supported by a porous matrix, with gas-phase reactants supplied directly. The following reactions were used for ECC.

Scheme 1.2 *Reactions taking place in Wynveen and Quattrone's Low-Temperature ECC setup*

Cathodic Reactions	Anodic Reactions
$O_2 + 2H_2O + 4e^- \rightarrow 4OH^-$	$2H_2 + 4OH^- \rightarrow 4H_2O + 4e^-$
$CO_2 + OH^- \rightarrow HCO_3^-$	$CO_3^{2-} + H_2O \rightarrow HCO_3^- + OH^-$
$HCO_3^- + OH^- \rightarrow CO_3^{2-} + H_2O$	$HCO_3^- \rightarrow CO_2 + OH^-$

Poor ion selectivity, high energy consumption (≥ 350 kJ/mol), low energy efficiency, and multiple steps involved were some drawbacks of their technology.

In 1985, Kang et al. reported a molten carbonate electrochemical cell capable of concentrating CO_2 from 1% to 5.8% and from 0.25% to 3.4%.[22] The cell exhibited low CO_2 purities and was based on the same principle as described by Huebscher and Babinsky in 1969.

Since the first few reports on electrochemical CO_2 capture in the late 1900s, the field has significantly expanded owing to the increased urgency to develop energy efficient, environmentally benign, and scalable CO_2 capture technologies. The number of reports and reviews on ECC technologies has significantly increased during the last five years. [23–35] Figure 1-4 shows the breakdown of the electrochemical CO_2 methods into redox-based and capacitive-based CO_2 capture. Redox techniques involve bulk electron transfer reactions to capture CO_2 either through electrochemical modulation of proton concentration (pH swing),[25,35] electrochemical generation of nucleophiles by reducing redox-active organic molecules,[23,29,36] or electrochemically mediated amine regeneration (EMAR).[24,37,38] Capacitive carbon capture techniques use electrochemical double-layer[39] electrode materials to capture and concentrate CO_2 during capacitive charging and discharging of the electrochemical cell without involving electron transfer reactions.

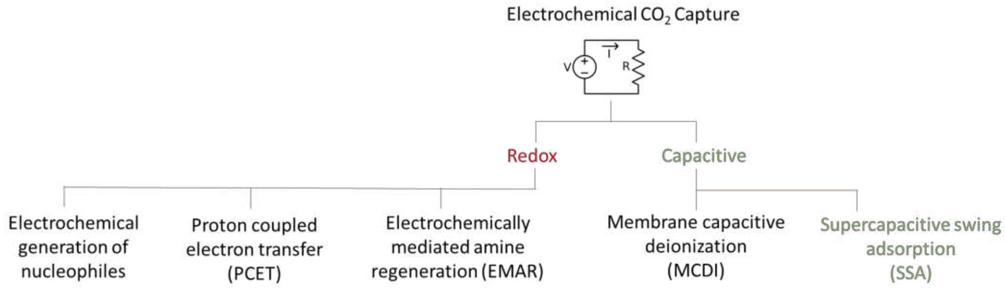

Figure 1-4 Existing electrochemical carbon capture technologies

A brief description of these CO_2 capture methods is provided in the next section.

1.4.1 Electrochemical generation of nucleophiles (EGNu)

In this method, an electrochemical cell containing a redox-active chemical is reduced during charging to produce nucleophiles that can bind with electrophilic carbon and selectively captures CO_2 molecules from a gas stream.[40] Discharging the electrochemical cell oxidizes and regenerates the redox-active chemical and releases CO_2. Most research groups working in this direction have used quinones as the redox-active chemical.[41] Other chemicals such as bipyridines and thiolates have also been explored for electrochemical capture and release of CO_2. These compounds selectively capture CO_2 in their reduced states and release it upon oxidation, similar to quinones.

1.4.2 Proton coupled electron transfer (PCET)

Proton-Coupled Electron Transfer, or pH swing, relies on the reduction and oxidation of a proton-coupled electrochemical reaction (e.g., $X + ne^- + nH^+ \rightarrow XH_n$) to adjust the pH of the sorbent between basic and acidic conditions.[35,42,43] Increase in pH of the electrochemical cell leads to the shift in $CO_2/HCO_3^-/CO_3^{2-}$ equilibrium towards HCO_3^-/CO_3^{2-} formation and CO_2 is captured. Reducing the pH in the electrochemical cell leads to CO_2 release. Figure 1-5 shows the effect of pH on $CO_2/HCO_3^-/CO_3^{2-}$ equilibrium. Membrane electrodialysis and electrolysis-based approaches are common approaches to capture CO_2 using PCET. Redox-active carriers such as quinone compounds have also been used for redox-mediated pH swing CO_2 capture.[4]

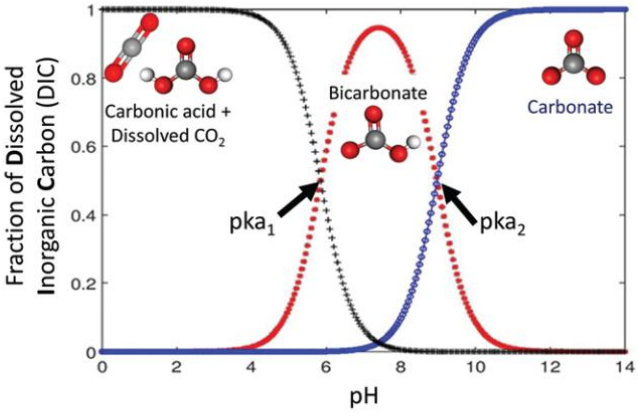

Figure 1-5 Relationship between pH and $CO_2/HCO_3^-/CO_3^{2-}$ equilibrium[4]

1.4.3 Electrochemically mediated amine regeneration (EMAR)

EMAR uses electric potentials to regenerate the amine solutions that otherwise required thermal regeneration at high temperatures.[24,37,44] This method relies on the competitive binding of CO_2 and a suitable metallic ion, such as $Cu^{2+,}$ to an amine molecule like ethylenediamine (EDA), acting as the absorbent. Initially, the amine absorbs CO_2 in a manner similar to conventional methods within the absorption column. In the next step, the CO_2-rich amine stream from the absorber is directed to the anode compartment of an electrochemical cell. Here, Cu^{2+} ions are electrochemically produced through oxidation at a Cu plate anode ($Cu^0 \rightarrow Cu^{2+} + 2e^-$) to induce amine-$CO_2$ dissociation, leading to the release of CO_2 ($Cu^{2+} + 2EDA\text{-}CO_2 \rightarrow Cu(EDA)_2{}^{2+} + 2CO_2$).

1.4.4 Membrane capacitive deionization (MCDI)

Membrane capacitive deionization uses supercapacitor electrodes and ion exchange membranes to separate CO_2 from a gas mixture during capacitive charging of the electrochemical cell.[45–48] The principle of MCDI is similar to a pH swing process described previously but without the involvement of bulk electron transfer reactions. As shown in Figure 1-6, charging the supercapacitor leads to attraction of cations including protons towards the negatively charged electrode. This increases the pH of the solution and aids in additional CO_2 storage in the form of HCO_3^- or CO_3^{2-} ions. Discharging the supercapacitor leads to decrease in pH and desorption of CO_2 takes place.

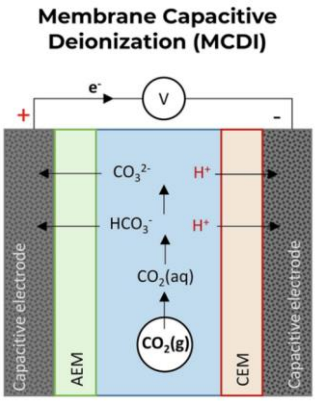

Figure 1-6 Schematic illustration of MCDI-based CO2 capture[45]

1.4.5 Supercapacitive Swing adsorption (SSA)

Supercapacitive swing adsorption (SSA) uses carbon-based electrodes and aqueous electrolytes. Charging the supercapacitor leads to CO_2 capture while discharging the supercapacitor leads to CO_2 release. Unlike MCDI, SSA does not require the use of membranes. It also does not require a three-step process in which the CO_2 is first dissolved in water using a first contactor, then the CO_2-containing solution is fed through the MCDI module, and finally the CO_2 is released from the aqueous solution using a second contactor. Both MCDI and SSA have emerged around the same time. This thesis is based on the progress made towards improving the SSA technology through novel electrode design, tuning the voltage windows, and quantifying the energetics and adsorptive performance under $CO_2/N_2/O_2$ gas mixtures. The fundamentals and historical aspects will be covered later in this chapter.

1.5 Challenges with existing electrochemical CO_2 Capture Methods

Existing electrochemical CO_2 capture methods have shown promise in terms of minimizing the toxicity of materials and avoiding the use of high temperatures or pressures. However, most existing research focusses on redox-based electron transfer reactions to drive CO_2 capture and release (e.g., PCET, EMAR). High energy losses due to overpotentials are associated with redox processes. The use of membranes and high materials cost associated with them, limited capacity retention of redox-reactions, and oxygen sensitivity are the major challenges to overcome. Capacitive techniques do not involve any bulk electron transfer reactions and offer faster charge-discharge cycles, high round-trip energy efficiency, and long cyclic stability. However, compared to redox techniques, a limited number of studies are available on capacitive carbon capture. Table 1-1 shows a summary of current challenges and needed research to improve existing electrochemical CO_2 capture methods. Among the two investigated capacitive carbon capture techniques (MCDI and SSA), SSA does not require the use of membranes and only require cheap porous carbon electrodes, aqueous electrolytes, and cellulose based separator. However, long term stability of SSA under oxygen environments is unknown. The influence of oxygen on SSA is covered in detail in chapter 5 of this thesis. The next part of this chapter covers the history of supercapacitors and supercapacitive swing adsorption technology, which is the main subject of this thesis.

Table 1-1 Summary of current challenges and needed research to improve existing electrochemical CO_2 capture methods. Electrochemical generation of nucleophiles (EGNu), proton coupled electron transfer (PCET), electrochemically mediated amine regeneration (EMAR), membrane capacitive deionization (MCDI), and supercapacitive swing adsorption (SSA) are compared.

CO_2 capture technology	Oxygen stability	Toxicity of materials	Use of membranes	Stability testing	Cost of Materials
EGNu	Not good	high	Yes	1000s of cycles	High
PCET	Not good	high	Yes	10s of cycles	High
EMAR	No	high	Yes	100s of cycles	High
MCDI	Unknown	medium	Yes	10s of cycles	High
SSA	Unknown	low	No	10s of cycles	Low

1.6 History of Supercapacitors

The principle of storing electrical energy by applying a potential difference between two metal plates was known since 1745.[49] A capacitor is a device used to store electrical charge. Capacitance (C) is the ability of a capacitor to store charges (Q) when a potential difference (V) is applied between the two metal plates separated by a dielectric. Mathematically,

$$C=Q/V$$

Charges in a capacitor are stored in a non-Faradaic manner, meaning there is no redox process associated with capacitive charge storage. Electrochemical capacitors, also known as supercapacitors, ultra capacitors, or electric double-layer capacitors, exhibit exceptionally high capacitance owing to the formation of an electric double-layer of electronic and ionic charges at the interface of a high surface area electrode and the dielectric. Supercapacitors were first used for energy storage, with records tracing back to a patent granted to Becker in 1957.[50] Robert A. Rightmire in 1966 and Donald L. Boos in 1970 at the Standard Oil Company of Ohio (SOHIO) patented the carbon based supercapacitors,[51,52] that formed the basis of many research articles and patents in the following years.

Compared to the micro-Farads of capacitance achieved by a conventional capacitor, hundreds of Farads of capacitance can be achieved by supercapacitors. The ultra-high capacitance comes from the very high surface area (≥ 1000 m^2/g) of porous carbon electrodes that can store extremely large numbers of ionic charges at the interface of electrodes surface to form an electric double layer. These Farad-size capacitors were initially used for memory back-up devices and now find applications in advanced transportation, portable electronics, emergency lighting systems, medical devices, aerospace and defense applications.[53] Modern applications of supercapacitors include water desalination by capacitive deionization and capacitive carbon capture.[54]

Besides electric double-layer capacitors, pseudo-capacitors and hybrid capacitors also exhibit very large capacitance values.[55] However, pseudocapacitors rely on fast, reversible surface redox reactions and use materials like metal oxides and conducting polymers. Hybrid capacitors are made by combining pseudocapacitors and electric-double layer capacitors. Figure 1-7 shows different types of supercapacitors and table 1-2 shows some commercial supercapacitor manufacturers.

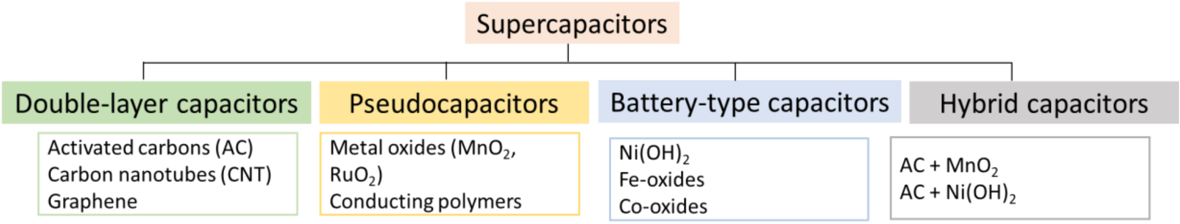

Figure 1-7 Supercapacitor types and the materials used for them[56]

Table 1-2 Some commercial supercapacitor manufacturers and performance comparisons[57]

Device Name	**Company**	**C (F)**	**V (volt)**
Supercapacitor	NEC-TOKIN, Japan	0.013-100	2.7-12
Supercapacitor	CAP-XX, Australia	0.075-2.40	2.3-5.5
Boostcap	Maxwell Tech. Inc. USA	5-3000	2.5-130
Gold Cap	Panasonic, Japan	0.015-10	2.1-5.5
Bestcap	AVX Corporation, USA	0.015-1.0	3.6-16
Capacitor modules	ESMA, Russia	107-8000	16-52
PowerStor	Cooper Bussman Electronics, USA	0.47-110	2.3-5.0
ESCap	Tavrima Canada Ltd., Canada	2.0-160	14.0-300
Ultracapacitor	LS Mtron Ltd., Korea	3-5400	2.5-84
EDLC	Nesscap Co., Ltd., Korea	5000	2.7
Capattery	Evans Capacitor Company, USA	0.033-1.5	5.5-25
KAPower	Kold Ban Int’l, USA	1000	3.0-14.5

1.7 Supercapacitive Swing Adsorption (SSA), Historical Background

The initial concept, known as electric field swing adsorption (EFSA), involved applying high electric fields and voltages to two electrolyte-free, cost-effective, high surface area carbon (HSAC) materials to facilitate the adsorption and desorption of carbon dioxide. HSAC materials function as electrically conductive sorbents with significant capacity for CO_2 capture. EFSA concept aimed to utilize high electric potentials (up to 5kV) to regulate the surface interaction between CO_2 gas molecules and the electrically conductive carbon sorbent material. Given the electron-deficient nature of CO_2, it was hypothesized that it would exhibit an affinity for an electron-rich π-system. The application of high electric potential was expected to alter the electronic structure of the carbon sorbent material, thereby enhancing, or diminishing its CO_2 adsorption properties based on the applied bias. Negative charges would increase the Lewis basicity of the sorbent surface. Additionally, the adsorptive forces could possess partial chemisorptive characteristics, resembling dative bonds between the Lewis basic π-electron system of the carbon and the Lewis acidic center of CO_2. Consequently, a negative bias would favor adsorption, while a positive bias would favor desorption. The selectivity of CO_2 over N_2, a primary component of flue gas, was anticipated to be substantial due to the absence of an electron-accepting center in nitrogen. Unfortunately, the hypothesis did not work, and no actual adsorption or desorption took place even at high voltages of 5kV. EFSA using a setup similar to a parallel capacitor did not work and the concept of using supercapacitors containing aqueous electrolyte was later introduced.[58] In contrast to a parallel plate capacitor capable to achieve very large potential differences of 5kV, supercapacitors use aqueous electrolytes and can only be charged upto ~1.23V, close to the thermodynamic potential window of water to avoid water splitting reactions.[59] Supercapacitors containing non-aqueous electrolytes can achieve higher voltages upto 3.5V, depending upon the type of electrolyte.

When a supercapacitor is charged, an electrical double layer of charges forms at the interface between the electrode pore surface and an electrolyte. The presence of this electric double layer was expected to alter the interaction of CO_2 with the electrode due to the storage of a significantly larger number of electrons and ions in the capacitor compared to a conventional parallel plate capacitor. Extremely high capacitance of electric double layer capacitors and microporous nature of activated carbon materials was realized for the implementation of supercapacitive swing adsorption for CO_2 capture. In 2014, our group published the first report on SSA using monolithic carbon electrodes and 1M NaCl electrolyte.[58] By monitoring the pressure changes during charging and discharging of the electrochemical cell, CO_2 adsorption and desorption was observed. An adsorption capacity of 40 $mmol.kg^{-1}$ at an energy consumption of 100 $kJ.mol^{-1}$ was achieved. In 2017, the second paper on SSA, reporting the design optimization and improvement in energy consumption was published.[60] The SSA module was built on the principles of coin type supercapacitors and fuel cells (Figure 1-8). An adsorption capacity of 38 $mmol.kg^{-1}$ energy consumption on 57 $kJ.mol^{-1}$ was reported. From 2017-2019, Shan Zhu published a series of papers reporting the scaled-up SSA modules with a radial flow system, and investigated different charging protocols, electrolytes concentration and composition to quantitively investigate the energetics and adsorptive performance metrics of SSA.[61–63] These fundamental and technological investigations helped in better understanding of the SSA mechanism. However, the adsorption capacity stayed below 100 mmol.kg^{-1}. Later in 2022, a group from Cambridge University reported the possibility of improving the adsorption capacity to values above 100 mmol.kg^{-1} by tuning the voltage window between -1 to +1V. From 2021 to 2024, significant progress has been made to improve the adsorption capacity values to as high as 780 mmol.kg^{-1} by investigating new materials, using higher voltages, and using oxygen in the CO_2/N_2 gas mixture. These developments will be discussed in chapter 3,4,5 of this thesis.

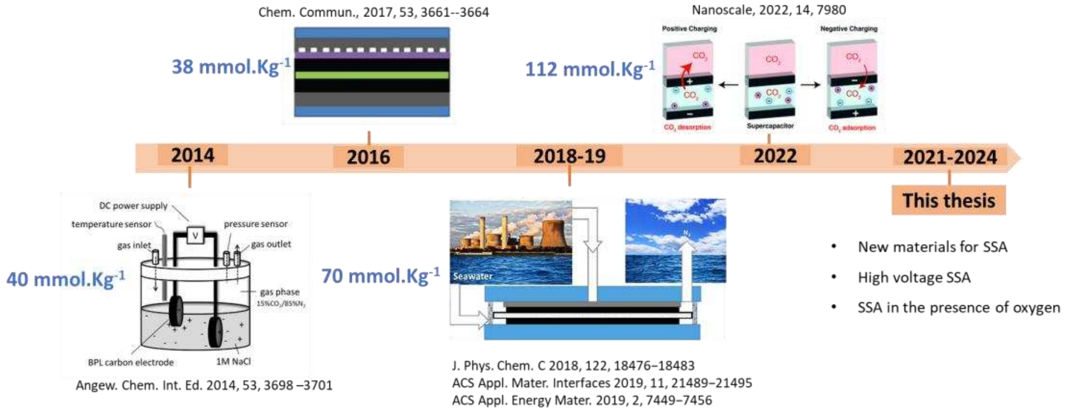

Chem. Commun., 2017, 53, 3661--3664

Nanoscale, 2022, 14, 7980

Angew. Chem. Int. Ed. 2014, 53, 3698 –3701

J. Phys. Chem. C 2018, 122, 18476–18483
ACS Appl. Mater. Interfaces 2019, 11, 21489–21495
ACS Appl. Energy Mater. 2019, 2, 7449–7456

Figure 1-8 Previous developments in supercapacitive swing adsorption

1.8 How does SSA Work?

The SSA technology relies primarily on the electrostatic adsorption of HCO_3^- and H^+ ions to the electrical double layers (EDL) of capacitively charged, porous carbon electrodes, infiltrated with an aqueous electrolyte (Figure 1-9). As the electrodes become capacitively charged, H^+ and HCO_3^- ions, generated from the dissolution and hydrolysis of carbon dioxide (CO_2) in the electrolyte, get attracted to the negative and positive electrodes, respectively, along with the anions and cations of the electrolyte. This electrostatic attraction of oppositely charged ions to the double layer lowers the concentration of HCO_3^- and H^+ ions in the bulk electrolyte, promoting additional CO_2 dissolution and hydrolysis, until chemical equilibrium is reestablished. Upon discharge of the electrodes, the process is reversed, releasing the CO_2. The adsorption is highly selective for CO_2, as only CO_2, and not N_2, O_2, and Ar, form ions in water. Since protons have a smaller size, high charge density, high mobility, and can covalently protonate electron lone pairs at heteroatoms in the activated carbon, they may preferentially adsorb at the negative electrode, and the adsorption of HCO_3^- at the positive electrode may not be necessarily needed.

In addition to the ionic liquid solid mechanism, additional CO_2 may be adsorbed to the electric double-layer at the electrodes through a molecular liquid-solid mechanism, as the solubility of molecular CO_2 in an electric double layer containing HCO_3^- ions may exceed that in free solution. CO_2 may also adhere to the hydrophobic, non-infiltrated pores, as the Fermi-level of non-infiltrated pores is altered due to the electrode charging. This is known as the gas-solid mechanism.

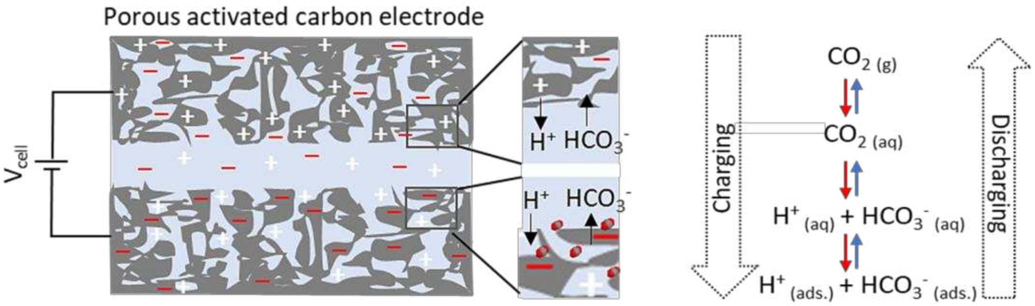

Figure 1-9 Proposed ionic liquid solid mechanism for SSA

1.9 Advantages of SSA

SSA presents several advantages that position it as a promising option for carbon dioxide capture:

1. Long Cycle Life: SC requires only the physical rearrangement of electronic and ionic charge, with no chemical changes, and can typically be cycled over a million times with minimal performance degradation. Thus, the process of adsorption and desorption can be continuously repeated.

2. Energy Recovery and Faster Charge-Discharge: The SSA method relies on the repeated capacitive charge and discharge of supercapacitors (SC), allowing the energy invested for adsorption to be principally recovered upon desorption. The charging and discharging of supercapacitor is much faster than other electrochemical devices.

3. No Temperature and Pressure Changes Required: In an SSA cycle, no temperature and pressure changes are required as adsorption and desorption are controlled solely by capacitive charge and discharge. SSA is also compatible with the temperature conditions of flue gas leaving a desulfurization unit (around 70 °C).

4. Use of Inexpensive and Environmentally Friendly Materials: Only robust, inexpensive, low toxicity, environmentally benign materials are required (ACs, aqueous solutions, carbon black, cellulose-based separators), leading to low capital cost. There are little environmental and health concerns. At the end of its lifetime, the electrodes may be used as “biochar” for agriculture, or regenerated, avoiding waste problems, and decreasing cost.

5. Selectivity and reversibility: The adsorption of CO_2 is highly selective over N_2 and requires investigation under oxygen conditions. CO_2 undergoes capacitive adsorption, primarily as HCO_3^- and H^+ ions, facilitated by electrostatic forces. This form of adsorption is easily reversible through the capacitive discharge of the electrodes.

6. Moisture insensitive: SSA operates using aqueous electrolytes. The ions in the electrolyte form a part of the electric double layer when the supercapacitor is charged. Water vapor or moisture in the gas mixture may not affect the adsorption of CO_2 and may keep the electrodes wet for long term operation.

7. Energy Storage System: SSA can serve as a dual-purpose system, providing both carbon capture and back-up energy storage for electrical grids powered by intermittent renewable energy sources like wind and solar. This approach can potentially lower the net cost of DAC, as indicated in our preliminary Techno-Economic Analysis (TEA).

8. Reduced Parasitic Load: The parasitic load associated with SSA is likely to decrease with increasing operating temperature. This is because the charge-discharge energy efficiency of supercapacitors increases with temperature due to the higher ionic conductivity.

1.10 Challenges of SSA

1. Low CO_2 adsorption capacity: The adsorption capacity of SSA prior to the start of the work presented in this thesis (before 2021) was well below 100 $mmol.kg^{-1}$. Amine based materials have an adsorption capacity $\geq$1000 $mmol.kg^{-1}$. New materials with enhanced adsorption capacities were desirable.

2. Slow adsorption kinetics: The rate of CO_2 adsorption during charging stayed around 25 $\mu mol.kg^{-1}.s^{-1}$ (< 100 $mmol.kg^{-1}.h^{-1}$). Faster sorption rates were desirable to improve the efficiency and economics of the process.

3. Performance under oxygen: SSA performance in the presence of oxygen, which is a major component of flue gas and air, was not investigated.

4. Long-term Stability: The SSA tests reported previously show less than 100 h of operation. The long-term operation of SSA (≥ 1000 hours) is needed to be investigated.

1.11 Research Aim and Scope of Thesis

This thesis covers the synthesis, characterization, and performance of biomass-and non-biomass-derived activated carbon electrodes with enhanced capacitance and enhanced CO_2 adsorption capacity. A quantitative comparison of the SSA energetics and adsorptive performance of different types of activated carbons is reported, and the critical factors contributing towards SSA performance improvements are discussed. In the next part, a modified, one-step synthesis procedure is used to synthesize micro-mesoporous garlic roots-derived activated carbon electrodes. High-voltage SSA studies were conducted to investigate how voltage window affects CO_2 adsorption capacity and what is the maximum voltage window possible for SSA with CO_2/N_2 mixtures. The last section covers the critical role of oxygen on the energetics and adsorptive performance of SSA and discusses SSA performance with 15% CO_2/5% O_2/80% N_2 gas mixtures. The long-term stability of SSA is addressed. Figure 1-10 shows a snapshot of the research presented in the later chapters of thesis.

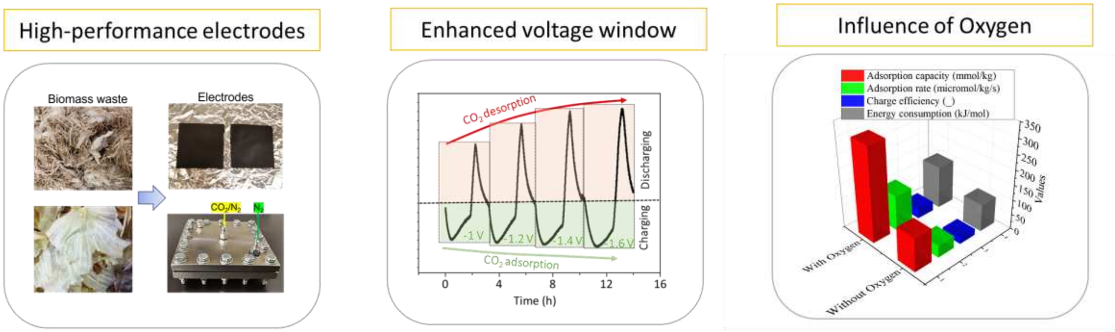

Figure 1-10 Overview of the research presented in this thesis to improve SSA performance

CHAPTER 2: CHARACTERIZATION TECHNIQUES

2.1 Introduction

This chapter covers the fundamentals of electrochemical characterization techniques used to evaluate performance of electrode materials for SSA and the fundamentals of physicochemical characterizations used to investigate the porosity, pore size, elemental composition, and surface functionalities of activated carbons.

2.2 Electrochemical Characterizations

Electrochemical characterizations used for the investigation of electrodes for SSA include cyclic voltammetry (CV), galvanostatic charge-discharge (GCD), and electrochemical impedance spectroscopy (EIS).

2.2.1 Cyclic Voltammetry (CV)

CV is a powerful technique used to investigate the behavior of an electrochemical system both qualitatively and quantitatively.[64] A typical electrochemical system consists of a working electrode (the electrode of interest), a reference electrode (provides a stable reference point for measuring the potential of a working electrode), a counter electrode (completes the electric circuit and ensure smooth flow of current). The principle of CV involves applying a potential sweep at a desired scan rate to an electrochemical system and measuring the resulting current. The potential of the working electrode (WE) changes gradually over time from the initial potential (Init E) to the highest point (High E), then it switches direction until it reaches the lowest point (Low E). After that, it switches direction again to return to the initial potential, completing one cycle of the scan (Figure 2-1). During this process, the current flowing through the electrode is measured and displayed as a function of potential.

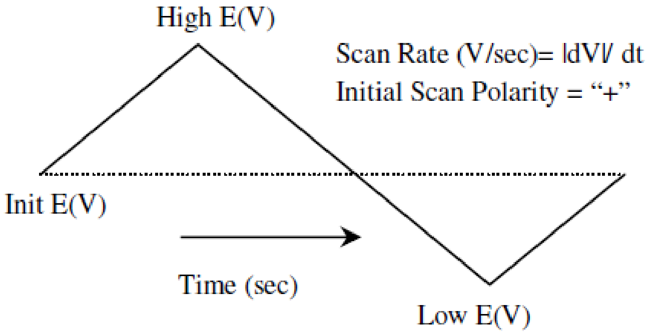

Figure 2-1 Voltage changes during cyclic voltammetry.

CVs at different sweep rates and different voltages are used to extract useful information about an electrochemical system such as its charge storage behavior, electrochemical kinetics, ions adsorption and double-layer formation, stability and reactivity of electrodes. In SSA research, CVs provide useful information regarding the capacitive behavior of different electrodes, kinetics of charge storage, contributions of double-layer capacitances and diffusion-controlled capacitances and estimates of onset voltages for faradaic reactions. Figure 2-2 shows that CV curves of different types of electrode materials result in different current vs potential profiles. Activated carbons exhibit double layer-type behavior (a), oxides like MnO_2 exhibit surface redox charge transfer and pseudocapacitive behavior (b). In both cases, the potential vs time profiles are linear (c). The intercalation type pseudocapacitive (type B) and battery type faradaic (type C) behavior results in non-linear potential vs time profiles and will not be discussed in this thesis. Most CVs in this thesis exhibit EDLC type behavior since material of interest in this research is activated carbon from different biomass and non-biomass sources.

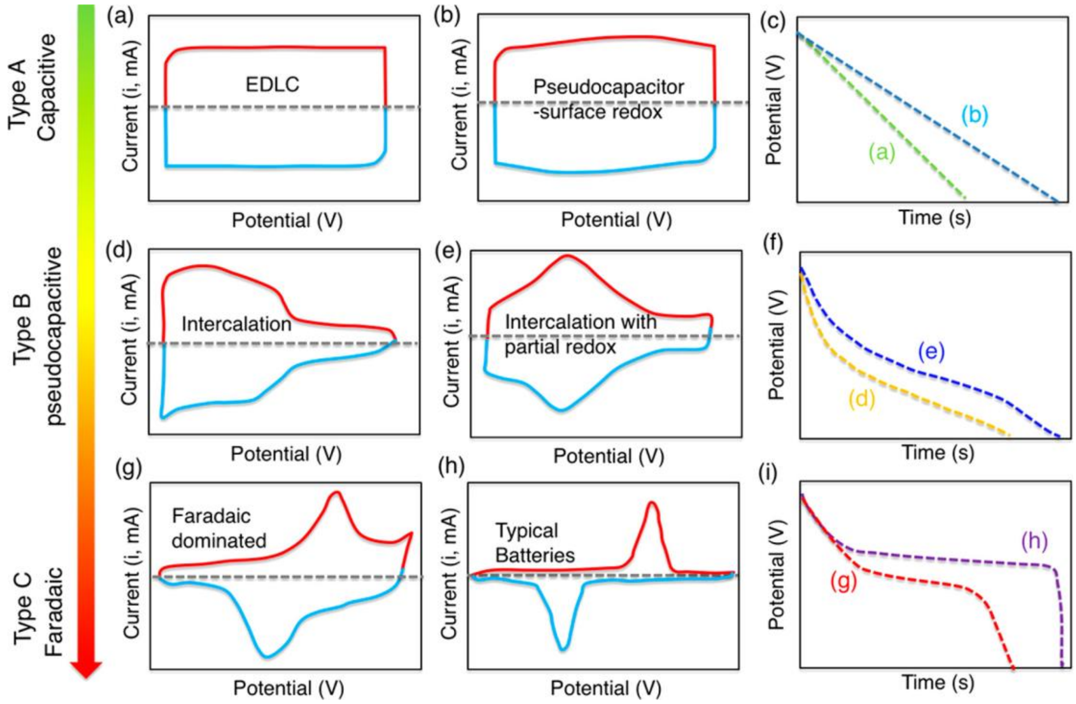

Figure 2-2 Cyclic voltammetry curves of different capacitive, pseudocapacitive, and faradaic electrodes.[65]

2.2.2 Galvanostatic charge-discharge (GCD)

The goal of this test is to consistently apply a set current to a supercapacitor electrode material, allowing it to charge and discharge within specific voltage ranges. The resulting voltage curves can be used to accurately determine the capacitance, resistance, energy efficiency, coulombic efficiency, and energy loss in a supercapacitor. Depending upon the current, capacitance values can vary. A faster charging at a higher current usually results in higher resistance. On the other hand, slower charging will result in lower resistance but takes more time to reach a specific voltage (Figure 2-3). This is due to the porous nature of activated carbon electrodes.[66] Smaller current allows more time for the efficient transport of ions from the bulk solution to the electrode micropores and mesopores, resulting in lower resistance, high energy efficiency, and higher capacitance. Typical current ranges used to charge supercapacitors vary between 50 mA/g to 500mA/g. In the ideal case, the charging and discharging chart of an EDLC supercapacitor displays linear curves, which are essentially mirror images of each other. However, battery type materials and pseudocapacitive materials display non-linear voltage profiles due to the faradaic reactions associated with them.

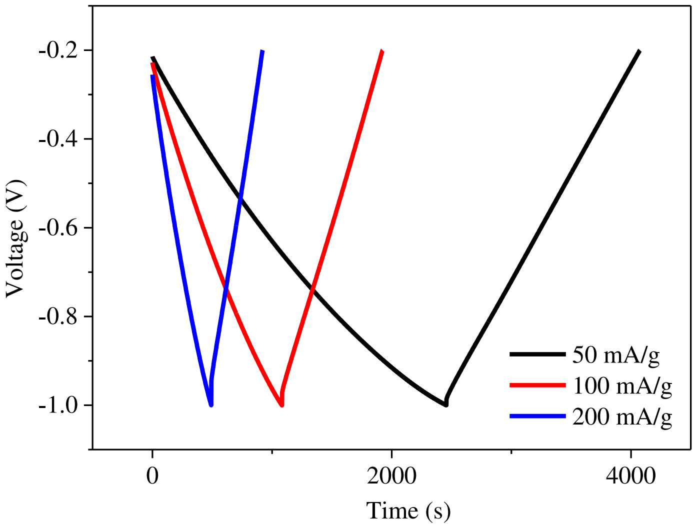

Figure 2-3 GCD profiles of a metal organic framework (MOF) supercapacitor at different current densities showing nealy linear charge and discharge curves.

2.2.3 Electrochemical Impedance Spectroscopy (EIS)

EIS is used to study the frequency dependent response of electrochemical systems. EIS involves applying a time harmonic oscillating electric potential with a small oscillation amplitude (typically less than 10 mV) around a constant "DC potential" at the electrodes surface. The collected data can be visualized through a Bode plot (showing relation between phase angle and frequency) or a Nyquist plot (showing relation between real and imaginary components of the cell's impedances on a complex plane). For supercapacitors, a Nyquist plot can provide detailed information regarding the different types of resistance (electrode resistance, solution resistance, diffusion resistance) and capacitance (real capacitance, imaginary capacitance) [67–69].

Figure 2-4 shows the Nyquist plot of a typical carbon-based supercapacitor. The x-axis represents real component of the impedance (Z_{re}) and the y-axis represents the imaginary component of the impedance ($-Z_{im}$). Z_{re} signifies the overall resistance response of the material. The smaller the Z_{re}, the smaller will be the overall resistance of the material. Z_{im} represents the capacitive component of a material. The point of the start of semi-circle represents the ohmic cell resistance including the electrode resistance and the ionic electrolyte resistance (point A), the point where the semi-circle ends represents the charge-transfer resistance and the contact resistance (point B).[70–74] The slope after the semi-circle represents ion-diffusion resistance or Warburg resistance (point C). It is the resistance faced by ions while diffusing from the electrolyte to the electrode micropores.[75] The quasi-vertical line after the Warburg slope signifies capacitance.

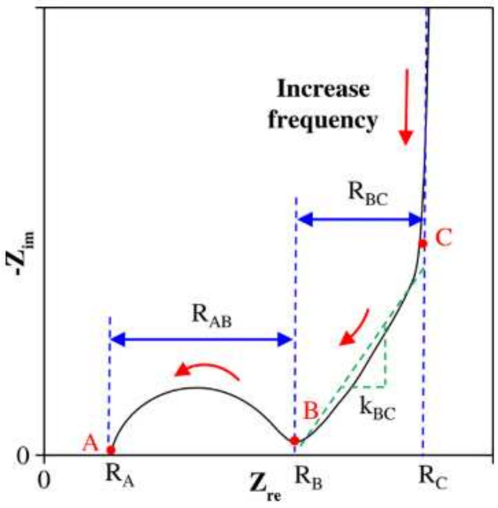

Figure 2-4 A typical Nyquist plot of activated carbon supercapacitor [68]

The real capacitance, imaginary capacitance, and total capacitance can be calculated using the following relations:[67,76]

$$C_{real} = Z''/2\pi f|Z|^2$$

$$C_{imag} = Z'/2\pi f|Z|^2$$

$$C_T = 1/2\pi f Z''$$

Here, C_{real}, C_{imag}, and C_T represent the real capacitance, imaginary capacitance, and overall capacitance of the supercapacitor. f is the frequency, Z' is real impedance, Z'' is the imaginary impedance, and $|Z|$ signifies the overall impedance of the supercapacitor. C_{real} signifies how much charge is reversibly stored in the electrode. C_{imag} represents energy dissipation/losses arising from kinetically irreversible processes/ diffusion limitations. Similar impedance plots will be discussed and compared in the next chapters of this thesis.

2.3 Physicochemical Characterizations

Physical characterization techniques assist in the analysis and understanding of chemical and morphological properties of electrodes and activated carbons. In this thesis, we used gas adsorption-desorption analysis, X-ray photoelectron spectroscopy (XPS), and in situ Raman spectroscopy. These techniques are pivotal for providing detailed insights into the surface area, pore size, composition, and structure of the electrodes. The fundamentals of these techniques is discussed in the following section.

2.3.1 Gas adsorption-desorption

Physical adsorption of a gas on a solid (gas-solid interface) is widely used for characterizing the surface and structural properties of porous materials. It enables the determination of parameters such as surface area, pore volume, and pore size distribution. This method typically involves introducing a known volume of gas (usually nitrogen) to a solid material in a sample vessel at cryogenic temperatures (typically 77K for nitrogen). At such low temperatures, weak molecular attractive forces (van der Waals forces) cause the gas molecules to adhere to the surface of the solid material. During the process, the gas (adsorbate) is incrementally added to the sample in controlled doses, and the pressure in the sample vessel is measured after each dosing. There exists a direct relationship between the pressure and the volume of gas in the sample vessel. The ideal gas law can be applied to determine the volume of gas adsorbed by the sample. The relationship between the volume of gas adsorbed and the relative pressure (pressure divided by the saturation vapor pressure of the adsorbent, denoted as P/P_0) at a constant temperature is termed an adsorption isotherm. Analysis of the isotherm allows for the derivation of the sample's surface area and pore size distribution. Adsorption isotherms exhibit various shapes, influenced by factors such as the type of adsorbent, adsorbate, and their interaction. According to the International Union of Pure and Applied Chemistry (IUPAC), adsorption isotherms are classified into six types, as shown in Figure 2-5.[77] In surface adsorption, hysteresis refers to the difference between the desorption isotherm and the adsorption isotherm (shown in type IV and type V isotherms). The hysteresis loop indicates different pore structures of the material.[78]

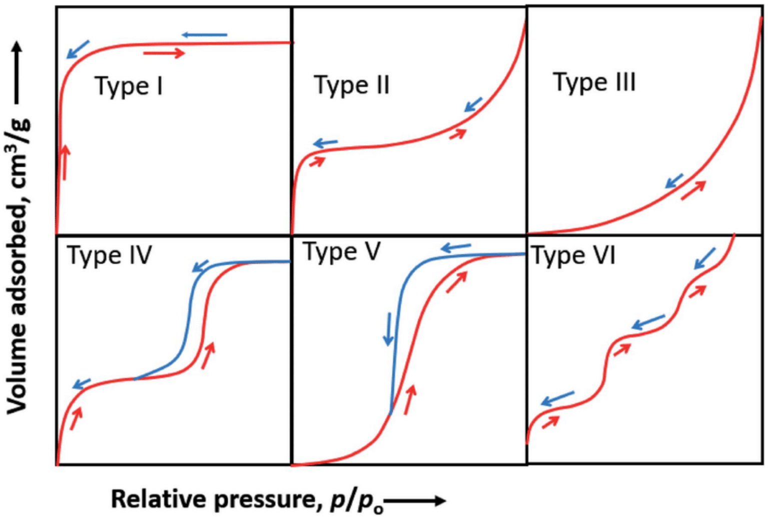

Figure 2-5 A typical Nyquist plot of activated carbon supercapacitor[77]

In scientific literature, various mathematical models describe adsorption phenomena. One of the simplest models is the Langmuir monolayer adsorption model, which assumes adsorbate molecules occupy fixed, distinct sites on the surface without interacting with each other. In 1938, Stephen Brunauer, Paul Emmett, and Edward Teller extended the Langmuir model with the BET model. This model suggests that each adsorbate molecule on the first layer can also serve as a site for adsorption onto subsequent layers. The details of the types of isotherms, types of hysteresis, Langmuir theory, and BET theory involve mathematical equations and their explanations, and not discussed further in this thesis.

Surface area measurements typically involve using inert adsorbates like N_2 or Ar, and they're usually expressed in units of area per mass of the sample (m^2/g). By determining the amount of adsorbate needed to cover the surface with a monolayer at a specific pressure, we can calculate the total surface area of the material. For characterizing the different types of activated carbons investigated in this thesis, the N_2 sorption isotherms were measured at 77 K using Micromeritics ASAP 2020 equipment.[79] The samples were degassed under 200 °C for 24 h before the analysis. The area and volume information of the micropore and mesopore were calculated from the adsorption data using the t-plot method (Carbon Black STSA model). The pore size distribution curves were obtained from the adsorption data using the non-local density functional theory (NLDFT) method. Slit type geometry of pores was used for simulation.

2.3.2 X-ray Photoelectron spectroscopy (XPS)

XPS is a method used to analyze the surface chemistry of materials. It can determine the elemental composition and the chemical and electronic state of atoms in a material.[80]

The principle of XPS is based on photoelectric effect. XPS works by directing X-rays onto a solid surface and measuring the kinetic energy of the emitted electrons from the top 1-10 nanometers of the material. A spectrum is produced by counting these ejected electrons across a range of kinetic energies. By analyzing the energies and intensities of the peaks in the spectrum, it's possible to identify and quantify all surface elements except hydrogen and helium.

In an XPS spectrum, the number of detected electrons is plotted against specific binding energies. Each element in the sample produces characteristic peaks in the spectrum, which correspond to the electron configurations within its atoms, such as 1s, 2s, 2p, 3s, and so on. The number of electrons detected in each peak directly correlates with the amount of that element present in the XPS sampling volume. To obtain atomic percentage values, the raw XPS signal for each element is corrected by dividing its intensity by a relative sensitivity factor (RSF). These corrected values are then normalized across all detected elements.

The XPS measurements of different biomass and non-biomass derived activated carbons used during SSA research were performed using a custom-built SPECS XPS instrument. All spectra were acquired using a photon energy of 1486.6 eV Al K_α, with analysis performed on electrons escaping in a direction normal to the sample surface. The pass energy for all core level scans was 20 eV and the pass energy for survey scans was 70 eV. The elemental percentages were estimated by calculating the area of each core level peak and normalizing by its Scofield cross section and mean free path.

2.3.3 Raman Spectroscopy

The Raman effect was first discovered in 1928 by an Indian scientist C.V. Raman. The Raman effect occurs when electromagnetic radiation interacts with matter, resulting in the scattering of light. This interaction causes an exchange of energy in the vibrational region of the molecules involved.[81] The fundamentals of Raman scattering differ from those of IR absorption. In IR absorption, there's direct resonance between the frequency of the IR radiation and the vibrational frequency of a specific mode. Transitions involving changes in the dipole moment of the molecule during vibration are active in IR, making it a one-photon event. Raman transitions also correspond to transitions between vibrational states, but Raman scattering involves a change in the polarizability of the molecule during vibration, making it a two-photon event. The scattered light includes both elastic radiation (Rayleigh scattering) and inelastic scattering (Raman scattering). Raman photons are shifted in frequency from the incident radiation, reflecting the vibrational energy gained or lost in the molecule. As shown in Figure 2.6, the starting point is the ground electronic state's zero vibrational level, while the end point is the ground electronic state's first vibrational level. IR absorption achieves this state change in one step, whereas Raman scattering requires two steps with photon energies, the difference of which equals the energy of the vibrational transition (a two-photon event). The photon excites the molecule, which may then relax in different ways, returning either to its original energy state or to a different energy state. If the molecule returns to its original energy state, the released energy matches the absorbed energy (elastic or Rayleigh dispersion). Occasionally, the molecule releases an energy different from what it absorbed (inelastic or Raman dispersion). Typically, the molecule ends in a more excited energy level, resulting in released energy lower than absorbed energy, reflected in a larger wavelength (lower wavenumber), known as Stokes dispersion (Figure 2-6). Conversely, if the final energy level of the molecule is lower than the original one, the molecule releases more energy than absorbed, resulting in a decrease in wavelength and an increase in frequency, known as anti-Stokes dispersion.

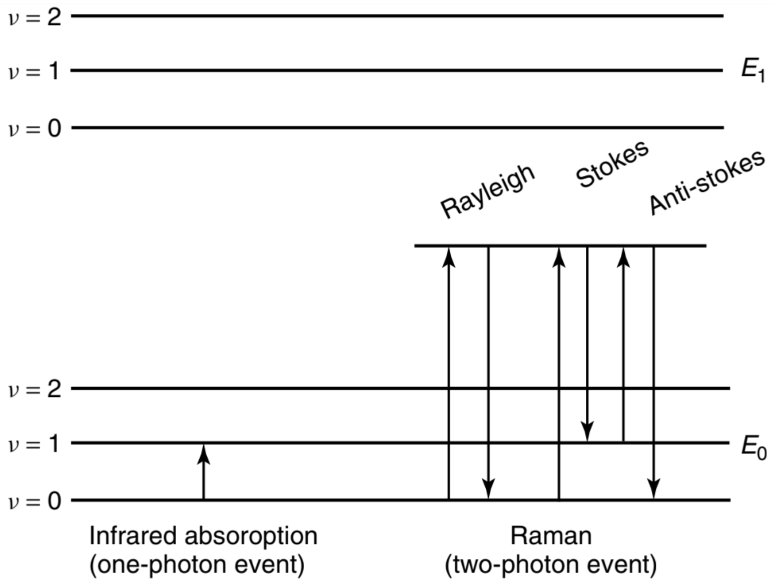

Figure 2-6 Energy level diagram showing Raman and IR comparison

In this research, *In situ* Raman spectra of activated carbon electrodes were collected on a Horiba LabRam-HR Raman spectrometer. The laser was focused through a quartz window onto the top electrode. Spectra were collected at several different voltages with and without oxygen in the gas mixture to know the changes taking place on the electrodes surface.

2.4 Conclusions

This chapter discussed the fundamental principles of different electrochemical and physicochemical characterizations. The basics of cyclic voltammetry (CV), galvanostatic charging and discharging (GCD), and electrochemical impedance spectroscopy (EIS) discussed in this chapter will be helpful to understand the analysis and comparison of different types of activated carbons presented in the next chapters. The knowledge of gas adsorption-desorption, X-ray photoelectron spectroscopy (XPS), and Raman spectroscopy will be helpful for the discussion of surface area, pore size, surface functionalities, elemental composition, and structural changes of the activated carbons and the electrodes prepared from activated carbons.

CHAPTER 3: ELECTRODE MATERIALS WITH ENHANCED SUPERCAPACITIVE SWING ADSORPTION OF CO_2

This chapter has been published as: Enhancing Supercapacitive Swing Adsorption of CO_2 with Advanced Activated Carbon Electrodes, ***Advanced Sustainable Systems****, 2300250 (2023).* *https://doi.org/10.1002/adsu.202300250*

3.1 Introduction

The escalating levels of anthropogenic carbon dioxide (CO_2) in the atmosphere has caused the earth's temperature to rise by approximately 1.2° C during the last five decades.[82] Currently, human activities release about 40 billion tons of CO_2 every year.[3] According to the intergovernmental panel on climate change (IPPC), the CO_2 emissions would need to be reduced to 20 billion tons per year to limit warming to 1.5° C compared to the preindustrial levels.[5] Industrial point sources such as coal, natural gas, and cement industries which contain CO_2 in the range of 4-20 % account for more than half of the anthropogenic CO_2 emissions.[4,83] Effective technologies that can remove CO_2 both from industrial sources and directly from the atmosphere are high in demand because the transition to renewable energy alone may be too slow in order to meet climate goals.[4,83,84]

The general requirements for an efficient carbon capture technology include high sorption capacity, low energy consumption, high selectivity for CO_2 over other gases in the mixture, facile reversibility of adsorption, fast sorption kinetics, and the use of robust, long-living, and inexpensive materials.[40,85] To date, the most widely used technology for CO_2 capture is amine scrubbing, which requires the use of corrosive, volatile, and toxic solvents.[23,86] Alternative technologies for carbon capture include pressure swing adsorption (PSA) and temperature swing adsorption (TSA) on porous sorbents such as zeolites and porous carbons. PSA and TSA tend to have relatively low CO_2/N_2 selectivity, and frequently show high sensitivity to moisture in the gas mixture.[8,87] Solid-sorbents with grafted amines have also been reported. They exhibit high selectivity for CO_2, but have high thermal energy requirements for regeneration, and limited life-time due to the oxygen-sensitivity of amines.[9,88]

Electrochemical CO_2 capture techniques have gained considerable attention in recent years.[4,11,21,29,31,32,40] They avoid the energy penalty associated with thermal and pressure cycling. Among them, supercapacitive swing adsorption (SSA) is a promising emerging technology capable of reversibly capturing and releasing CO_2 by charging and discharging supercapacitor electrodes.[39] Supercapacitors are capable of electrostatically storing a large number of charges inside the pores of high surface area electrodes in an electrical double layer.[89–91] SSA is significantly simpler than other electrochemical sorption techniques, only requiring inexpensive, robust, and environmentally benign porous activated carbons and aqueous electrolytes (e.g. NaCl, $NaHCO_3$). Supercapacitors allow for fast charge-discharge rates, have a high round-trip energy efficiency, and a long lifetime ($> 10^5$ cycles). This is an advantage over electrochemical techniques that rely on the use of redox-active sorbents or solvents (e.g. quinones, redox-active amines).[15,20,21] Redox-techniques tend to have a more limited cycle-life, and frequently involve high cost materials such as carbon nanotube-based electrodes, redox-active specialty polymers, copper, special amines, and ionic liquids. Quinones and amines tend to be oxygen-sensitive.[24,30,31,37,38] Electrochemical methods based on pH-swings, e.g. membrane-capacitive deionization (MCDI),[45] electrolysis,[93] and bipolar membrane electrodialysis (BPMED),[42] have also been reported. However, MCDI require expensive materials such as cation and anion-exchange membranes.[45] Electrolysis and BPMED capture methods also require cation and anion exchange membranes and have high energy consumption (>300 kJ.mol^{-1}).[4,11] Proton coupled electron transfer (PCET) based pH-swing process have also been explored.[25,35,94] In PCET, the increase or decrease in pH is related to reduction or oxidation of organics, or H^+ intercalation/deintercalation on metal oxides. However, PCET of organics is oxygen sensitive and requires the use of ion-selective membranes to maintain a pH gradient. PCET of Metal oxides has not been investigated for long term stability. Moreover, metal oxides have poor electrical conductivity and smaller charge/discharge cycle life compared to activated carbons.[47] Table S1 provides a comparison of different electrochemical carbon capture methods in terms of energy consumption, current density, and operation mode.

In 2014, our group first demonstrated the concept of SSA by separating CO_2 from 15 % CO_2/85 % N_2 gas mixture, with extremely high selectivity of CO_2 over N_2.[58] Subsequent work focused on the development of SSA modules that can separate CO_2 from a gas-stream in batch-mode, and the collection of fundamental adsorptive and energetic performance data as a function of the charging protocols, electrolyte concentration, and electrolyte composition.[60–63] The highest adsorption capacity achieved for SSA modules with radial gas flow was around 70 mmol.kg^{-1} at an energy consumption of about 100 kJ.mol^{-1}.[63] Recently, Forse et al reported that the adsorption capacity of SSA can be increased to 112 mmol.kg^{-1} by cycling the electrodes between -1 V and +1 V instead of -1 V and 0 V but at a very high energy penalty (751 kJ.mol^{-1}).[95] Further improvement in adsorption capacity without compromising on the energy consumption is highly desirable.

SSA is believed to function according to three mechanisms. One, the ionic liquid-solid mechanism, assumes that CO_2 hydrolyses in the electrolyte to form H^+, HCO_3^-, and CO_3^{2-} anions that can adsorb to the double-layers of the negative (as H^+) and positive (as HCO_3^-/CO_3^{2-}) electrodes, respectively. Due to their high charge-density, small radius, and high mobility, protons are preferentially adsorbed to the negative electrode, regardless of the type of ions in the electrolyte.[63] The proton adsorption leads to an increase of the pH in the bulk electrolyte which allows for more CO_2 dissolution (and subsequent hydrolysis) into the bulk electrolyte, until the chemical equilibrium is re-established. The two other mechanisms assume the adsorption of molecular CO_2 to the double-layer due to a solubility difference of CO_2 in the bulk solution and the double-layer (molecular liquid-solid mechanism), and the physisorption of molecular CO_2 to hydrophobic pores that are not infiltrated by the electrolyte (molecular gas-solid mechanism). The ionic liquid-solid mechanism of SSA suggests that increasing the specific capacitance of the electrodes could lead to enhanced adsorption capacity, and that there may be a relationship between the adsorption capacity for CO_2 and the specific capacitance of the electrodes. The previously investigated BPL carbon only shows a moderate specific capacitance of ~80 $F.g^{-1}$, indicating substantial room for improvement through the use of carbons with higher specific capacitances.

Herein, we investigate biomass- (garlic skin, garlic roots, garlic powder), coal-, coke-, and carbide-derived activated carbons as electrode materials for SSA. Garlic roots, skin, and powder were selected because of the very high specific capacitance of activated carbons reported for garlic skin-derived carbons.[76,96] For comparison, we also investigated commercially available activated carbons from different non-biomass sources, namely Y carbon (derived from silicon carbide),[97] and Supersorb carbon (derived from coke)[98]. These materials exhibit varying porosity, pore size distributions, and surface functionalities which allows for studying the influence of these variables on the SSA performance. Our previously used BPL carbon (derived from bituminous coal) was used as benchmark material.[99] Two different electrode sizes (4 cm^2 and 49 cm^2) were used to study the dependence of electrode size on the performance of SSA.

3.2 Experimental Section

3.2.1 Materials

Garlic roots from Music type Hardneck garlic (K.V. farm, Stroudsburg, Pennsylvania), garlic powder (Badia spices, Doral, Florida), and garlic skin (Spice World) were used as feedstocks for preparing the activated carbons. Coal-derived BPL 4x6 carbon (Calgon), carbide-derived Y carbon (Y-Carbon) and coke-derived Supersorb carbon (Amoco Carbon) were used as commercially produced activated carbons. 60 %

PTFE dispersion (Sigma Aldrich), conductive carbon black (VXCMAX22, Cabot Corporation), gluten (Hodgson Mill), ethanol (190 proof, Decon Labs) and DI water (18 MΩ) were used as binder, conductive agent, hydrophilic co-binder, and solvent, respectively. 1 M $NaHCO_3$ was used as an electrolyte and filter paper (Whatman Grade 2, GE Healthcare Life Sciences) was used as a separator.

3.2.2 Synthesis of activated carbons

Synthesis protocols similar to those reported for activated carbons derived from garlic skin were used.[76] The biomass precursor (e.g., garlic roots) was thoroughly rinsed, washed several times with DI water, dried in the oven at 100°C overnight and sieved to less than or equal to 350 microns particle size. The powdered samples were carbonized in a tube furnace in N_2 atmosphere. About 26 g of pulverized garlic roots were heated to 600°C at a heating rate of 5.0°C min^{-1} in a 100 x 45 x 20 mm alumina crucible. The sample was kept at 600°C for 2 hours and then cooled slowly to room temperature. The yield of carbonization was around 30-35 % for all the samples. The carbonized garlic roots sample was mixed with KOH (mass KOH : mass carbon = 4:1) and ~30 mL DI water to form a homogeneous slurry. The slurry was transferred to a custom-made nickel sample holder and heated to 800°C at 5.0°C min^{-1} under N_2 in the tube furnace. The temperature was maintained at 800°C for 2 h before the sample was cooled to room temperature. The obtained sample was dissolved in 100 mL DI water and washed with 1 M HCl (20-30 mL) around 3-4 times to remove the remaining impurities (K, K2O, KOH, and K2CO3). It was further washed with DI water until the pH reached 7. The resulting sample was dried in the oven at 120°C overnight to obtain activated carbon powder. The final yield from garlic roots and garlic powder varied between 10-15 % while no significant yield was obtained from garlic skin. For garlic skin, the carbonization and activation time were therefore reduced to 1 h and activation temperature was reduced to 700° C to obtain around 11 % yield from garlic skin. The activated carbon samples obtained from garlic roots, garlic powder, and garlic skin were named GR-AC, GP-AC, and GS-AC, respectively. The remaining carbons were named BPL-AC, S-AC, and Y-AC, respectively.

3.2.3 Characterization of activated carbons

Surface and porosity analysis: The N_2 sorption isotherms were measured at 77 K using Micromeritics ASAP 2020 equipment. The samples were degassed under 200 °C for 24 h before the analysis. Low N_2 dosing mode was carried out before the relative pressure $P/P_0 = 0.000105$ in the adsorption branch. Total surface areas were calculated from the adsorption data at $P/P_0 = 0.001 \sim 0.051$ using the Brunauer-Emmett-Teller (BET) model. Total pore volumes were calculated from the adsorption data at $P/P_0 = 0.99$. The area and volume information of the micropore and mesopore were calculated from the adsorption data using the t-plot method (Carbon Black STSA model). The pore size distribution curves were obtained from the adsorption data using the non-local density functional theory (NLDFT) method, specifically with the N2-Carbon Finite Pores, AS=6. Here, AS=6 means a 2D model of finite slit pores having a diameter-to-width aspect ratio of 6. Slit type geometry of pores was used for simulation.

X-ray photoelectron spectroscopy: Activated carbon powders were affixed to the sample plate using copper tape. Measurements were performed using a custom-built SPECS XPS instrument. Charge neutralization was invoked during the analyses using a beam of 2 eV electrons at a current of 20µA. All spectra were acquired using a photon energy of 1486.6 eV Al K_{α}, with analysis performed on electrons escaping in a direction normal to the sample surface. The pass energy for all core level scans was 20 eV and the pass energy for survey scans was 70 eV. Core level spectra were fit using pseudo-Voigt profile components comprised of approximately 20% Lorentzian and 80% Gaussian broadening. In C1s and O1s spectra, the widths of the components were constrained to be equal to one another. In spectra with doublet peaks (Si2p), the relative heights, widths, and energy separation of the peaks were constrained using library values from Thermo's Advantage software. The elemental percentages were estimated by calculating the area of each core level peak and normalizing by its Scofield cross section and mean free path.

3.2.4 Electrodes preparation and supercapacitor assembly

Figure S1 shows the scheme for the synthesis and preparation of the activated carbon electrodes. Briefly, 0.083 g of PTFE was added to 10 mL of ethanol. The solution was mixed and sonicated simultaneously for 10 min to obtain a homogeneous mixture. 0.8 g of activated carbon, 0.1 g of gluten, and 0.05 g of conductive carbon black were added to the PTFE solution. The mixture was covered with Al foil and magnetically stirred at 60-65°C for 2 h. The temperature was then increased to 80°C for 30 min to evaporate the remaining solvent. The resulting slurry was transferred onto a glass plate, pressed, and mixed with metal spatulas for 30 min. The obtained dough was processed through a pasta machine (Atlas 150 roller, Marcato) to achieve the desired thickness of the electrodes. The electrodes were cut to the desired size (4 cm^2), placed in a vacuum oven at 100º C and 25 mmHg for 12 h. The same procedure was used to prepare 49 cm^2 electrodes.

The bottom electrode was soaked in 1 M $NaHCO_3$ solution for 2 hours. For the 4 cm^2 electrodes, a 4.84 cm^2 filter paper was wetted with the electrolyte and used as a separator. A 4 cm^2 carbon cloth (AvCarb 1071 HCB) was used to cover the top electrode and served as a gas diffusion layer. The electrodes, separator, and gas diffusion layer were surrounded by an EPDM rubber gasket (9.5 cm × 9.5 cm outer area, 8 cm × 8 cm inside area, 0.15 cm thickness, Fuel cell store) and sandwiched between titanium grade 7 plates (13 cm × 13 cm, 0.95 cm thick), which served as current collectors. The resulting assembly was pressed together by evenly tightening 16 set screws connecting the Ti plates using a torque wrench to 20 in.lb of force. For 49 cm^2 electrodes, 49 cm^2 carbon cloth and 56 cm^2 filter paper were used while the dimensions of gasket and current collector stayed the same.

3.2.5 Electrochemical testing of the electrodes

The electrochemical testing was performed using a Gamry 3000 potentiostat in a two-electrode configuration. Cyclic voltammetry (CV) tests were conducted at different scan rates in the potential range of 0 V to -1 V to gain information about the charge storage behavior of the supercapacitors. The specific capacitance values from CV were calculated using the relation C = Q/(ΔV × m) where Q is total charge stored during potential sweep, ΔV is the voltage window, and m is the average mass of the electrodes.

Electrochemical impedance spectroscopy (EIS) was performed at -0.5 V DC in the frequency range from 10^5 Hz to 10^{-3} Hz. Information about the solution resistance, charge transfer resistance, Warburg diffusion resistance and capacitance were extracted from the EIS data. The real capacitance, imaginary capacitance, and total capacitance were calculated using the following relations:[67,76]

$$C_{real} = Z''/2\pi f|Z|^2 \tag{1a}$$

$$C_{imag} = Z'/2\pi f|Z|^2 \tag{1b}$$

$$C_T = 1/2\pi f Z'' \tag{1c}$$

Here, C_{real}, C_{imag}, and C_T represent the real capacitance, imaginary capacitance, and overall capacitance of the supercapacitor. f is the frequency, Z' is real impedance, Z'' is the imaginary impedance, and $|Z|$ signifies the overall impedance of the supercapacitor.

Galvanostatic charging and discharging (GCD) was performed at a constant current density of 50 mA.g^{-1} to test the gas adsorption and desorption behavior of different supercapacitor electrodes. The specific capacitance (C_s) and equivalent series resistance (R_{ES}) were found using the following relations:

$$C_s = 4It_g/m\Delta V \qquad (2)$$

$$R_{ES} = (V - V_{drop})/I \qquad (3)$$

Where I is the constant current applied during the test, t_g is the galvanostatic charging duration, m is the total mass of activated carbon in top and bottom electrodes, and ΔV is the potential window.

3.2.6 Supercapacitive swing adsorption (SSA) testing

A schematic illustration of the SSA experimental setup is shown in Figure S5, and was described in detail in a previous publication.[100] A 15 % CO_2/85 % N_2 gas mixture flows through a bubbler filled with 1 M $NaHCO_3$. The purpose of bubbler is to moisten the gas before it enters the SSA module. This would prevent the drying out of electrodes and undesired concentration changes during the SSA tests. The moistened gas passes through a mass flow controller adjusted to a flow rate of 1 sccm. The gas mixture enters the SSA module from the center inlet port (1 mm in diameter) and flows radially through the gas diffusion layer inside the module. The gas exits from the outlet port at the corner of the top Ti plate, passes through a drying tube, and is then analyzed by a CO_2 analyzer (Quantek Instruments, Model 9-6). The gas mixture was flown through the modules for 8 h without applying any bias to complete conventional CO_2 adsorption to the electrodes and conventional CO_2 absorption by the electrolyte. After that time, the concentration of the exiting gas attained a constant value of 15% showing that conventional ad/absorption was complete. The module was then charged at a rate of 50 mA/g to -1 V (the gas-exposed electrode being the negative electrode at -1 V relative to the bottom (counter) electrode. The potential was then held at -1 V for an additional 30 min to allow for complete saturation of the electrode with CO_2. After that, the module was discharged to 0 V at 50 mA/g followed by a 30 min holding step to complete the desorption of CO_2 gas from the electrode.

3.2.7 SSA energetic metrics

The SSA energetic metrics include the calculation of equivalent series resistance (R_{ES}, $\Omega.cm^2$), gravimetric capacitance (C_s, $F.g^{-1}$), areal capacitance (C_A, $F.cm^{-2}$), volumetric capacitance (C_v, $F.cm^3$), charging time (t_g, s), total charge stored during charging (Q_c, C), total charge stored during discharging (Q_d, C), coulombic efficiency (η_c, %), energy efficiency (η_e, %), and energy loss (ΔE, J). These metrics were obtained from galvanostatic charge-discharge curves.

$$R_{ES} = \frac{V_{pstat} - V_{drop}}{I}$$

$$C_s = \frac{4.I.t_g}{m.\Delta V}$$

$$C_v = C_s \times \rho$$

$$C_A = C_v \times t$$

$$Q_c = \int_0^t I \, dt$$

$$\eta_c = \frac{Q_d}{Q_c} \times 100$$

$$\eta e = \frac{E_d}{E_c} \times 100$$

$$\Delta E = E_c - E_d$$

where V_{pstat} is the potentiostatic voltage (either 0 V or -1 V), V_{drop} is the voltage at the start of the charging or discharging step, I is the constant current, t_g is the charging time, m is the total mass of two electrodes, ΔV is the charging potential window, ρ is the density of electrodes, t is the average thickness of the electrode pair, C is the absolute capacitance, E_d is the energy delivered during discharging, and E_c is the energy consumed during charging. The capacitance calculation assumes equal capacitance of two electrodes.

3.2.8 SSA adsorptive metrics

The SSA adsorptive metrics include the calculation of the number of moles of CO_2 adsorbed during the charging plus the holding step ($n_{a,\ CO2.}$, µmol), adsorption capacity with respect to mass (AC, mmol.kg^{-1}), external electrode area (AC, mmol.m^{2}), and volume (AC, mol.m^3) of the gas-exposed electrode, adsorption rate (AR, μmol.kg^{-1}.s^{-1}), productivity (P, mol.h^{-1}.m^{-2}), charge efficiency (CE, dimensionless), energy consumption (EC, KJ.mol^{-1}), and time-energy efficiency (TEE, mol.KJ^{-1}.s^{-1}).

$$n_{a,CO_2} = \frac{P}{RT}\left(\int_0^t f_i \, dt - \int_0^t f_e \, dt\right)$$

$$AC = \frac{n_{CO2\,ads.}}{m_{top}}$$

$$AC = \frac{n_{CO2\,ads.}}{A}$$

$$AC = \frac{n_{CO2\,ads.}}{V}$$

$$AR = \frac{n_{CO2\,ads.}}{m_{top} \times t}$$

$$P = \frac{n_{CO2\,ads.}}{t \times A}$$

$$CE = \frac{n_{CO2\,ads.}}{n_c} = \frac{n_{CO2\,ads.}}{Q_c} \times F$$

$$EC = \frac{\Delta E}{n_{CO2\,ads.}}$$

$$TEE = \frac{n_{CO2\,ads.}}{\Delta E \times t}$$

Where P is the pressure (1 atm), T is the temperature (296 K), R is the general gas constant, f_i and f_e are the influent and effluent gas flow rates, m_{top} is the mass of top electrode, A is the area of electrodes, V is the volume of electrodes, and t is the total charging time (including the 30 min holding step).

3.3 Results and Discusstion

3.3.1 Porosity and compositional analysis

Biomass-derived carbons were synthesized through carbonization at 600 °C and subsequent KOH activation at 800°C. The detailed synthesis procedure is discussed in the experimental section. The activated carbons show a significant N_2 uptake at $P/P_0 < 0.05$, referring to a microporous structure,[101] as seen from the type-1 N_2 sorption isotherms (Figure 3-1a). The activated carbon prepared from garlic roots (GR) and garlic skin (GS) continue to adsorb N_2 at $P/P_0 > 0.2$, indicating the presence of abundant mesopores in addition to micropores. The activated carbons obtained from garlic powder (GP), garlic roots (GR), and garlic skin (GS) exhibit high Brunauer-Emmett-Teller (BET) surface areas of 2341 $m^2.g^{-1}$, 2454 $m^2.g^{-1}$, and 2582 $m^2.g^{-1}$, respectively. Coke-derived supersorb carbon (S), coal-derived BPL carbon, and carbide-derived Y carbon exhibit surface areas of 2715 $m^2.g^{-1}$, 1023 $m^2.g^{-1}$, and 1109 $m^2.g^{-1}$, respectively. A direct relation between surface area and pore volume is observed (Figure 3-1b). However, supersorb (S) activated carbon and garlic roots (GR) activated carbon flip positions with regards to their pore volumes. A maximum pore volume of 1.41 $cm^3.g^{-1}$ is obtained for GR activated carbon. The electrode densities of biomass-derived carbons are oppositely related with surface areas and follow the sequence: GR (0.19 g.cm^{-3}) < GS (0.25 g.cm^{-3}) < GP (0.28 g.cm^{-3}) (Figure 3-1c). Commercial activated carbons exhibit higher electrode densities than biomass-derived carbons and follow the sequence: S (0.31 g.cm^{-3}) < BPL (0.48 g.cm^{-3}) = Y (0.48 g.cm^{-3}). The micropore surface areas and micropore volumes of biomass-derived carbons (GP, GR, GS) are lower than commercial activated carbons (S, BPL, Y), as shown in table S2.

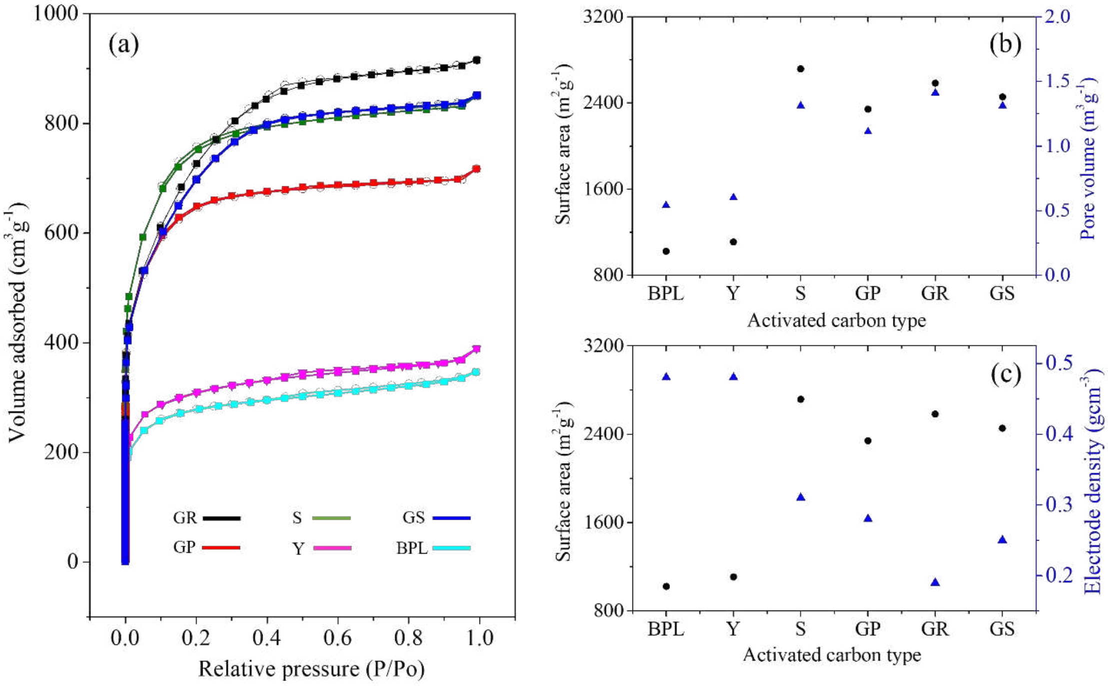

Figure 3-1 N_2 sorption isotherms of garlic powder (GP), garlic roots (GR), garlic skin (GS), coke derived supersorb (S), coal-derived (BPL), and carbide derived (Y) activated carbons (a). The desorption isotherms overlap with adsorption isotherms. Activated carbon type versus surface area and pore volume (b), and surface area and electrode density (c) show the difference in the porosities of each carbon.

Information about the surface structure and composition of activated carbons (ACs) was obtained from X-ray photoelectron spectroscopy (XPS). The survey scan of all ACs shows two main peaks at 284 eV and 532 eV, attributed to C1s and O1s (Figure 3-2a).

The N1s peaks at 400 eV are not visible in the survey spectra while small peaks at around 1000 eV are due to oxygen auger electrons. The surface chemical state of each AC was obtained by deconvoluting the high resolution C1s and O1s spectra (Figure S2 and Figure 2b). Three surface chemical states of carbon (C-C_3 sp^2, C-C_4 sp^3, sp^2/sp^3 C-$O_{x\text{-}}C_y$ (x=1,2; y =1-3)) are identified in all the samples. The percentage (atomic %) of sp^2-hybridized C-atoms is highest in GR (83.5 %) and follows the sequence GR > GS > Y > BPL > GP > S. The percentage of sp^3-hybridized C-atoms follows the sequence S > GS > Y > BPL > GR > GP. The percentage of C-O follows the sequence S > BPL > GP > Y > GR > GS. Higher sp^2 character and presence of oxygen functionalities are desirable for improving the conductivity and pseudocapacitance, respectively. The percentage of OH functionality is highest in GR (4.0 %) and follows the sequence GR > GP > GS > S > BPL > Y. Among the six carbons, GS, S, BPL, and Y contain very small amounts of C-N bonds (Figure 3-2b). The elemental percentage of C, O, N, and other elements is given in table S3.

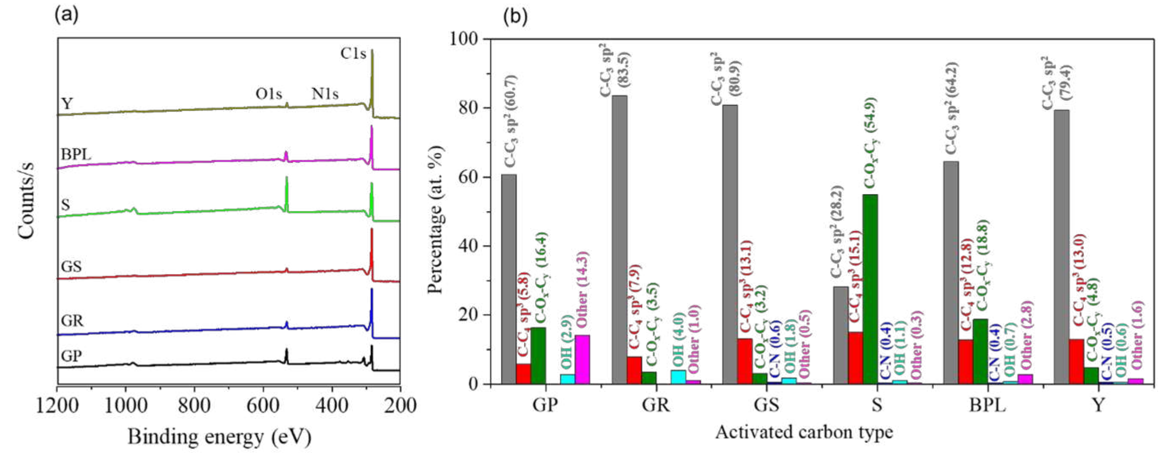

Figure 3-2 XPS survey spectra of six activated carbons (a) and percentage contribution of C-C3 sp^2, C-C4 sp^3, C-O$_x$-C$_y$, OH, C-N, and other chemical states in each activated carbon (b).

Cyclic voltammetry (CV) and electrochemical impedance spectroscopy (EIS) analysis

The cyclic voltammograms of the supercapacitors from biomass-derived and commercially available carbons show typical electrochemical double-layer (EDL) behavior at scan rate of 1 mV.s^{-1} (Figure 3-3). GP-AC, GR-AC, and BPL-AC maintain the EDL behavior and high charge storage ability also at scan rates of 3 and 5 mV.s^{-1} (Figure 3 a, b, and e). S-AC and Y-AC show deviation from ideal EDL behavior as the scan rate increases from 1 mV.s^{-1} to 5 mV.s^{-1}. GS-AC shows the maximum deviation from EDL behavior even at 1 mV.s^{-1} due to high resistance and slow charge transport kinetics of the electrodes. GS-AC was carbonized at 600° C for 1 h at a heating rate of 6.5° C.min^{-1} and activated at 700° C for 1 h at a heating rate of 5.5° C.min^{-1}. On the other hand, GP-AC and GR-AC were carbonized at 600°C for 2 h at 5° C.min^{-1} and activated at 800°C for 2 h at 5°C.min^{-1}. The synthesis conditions were modified to achieve a reasonable yield for GS-AC (~11%). GS activation at 800°C led to no yield at all. Nevertheless, GS-AC electrodes showed high specific capacitance and high adsorption capacity, comparable to GP-AC and GR-AC during the supercapacitive swing adsorption (SSA) tests (at a constant current of 50 mA.g^{-1}), as will be discussed in the later section.

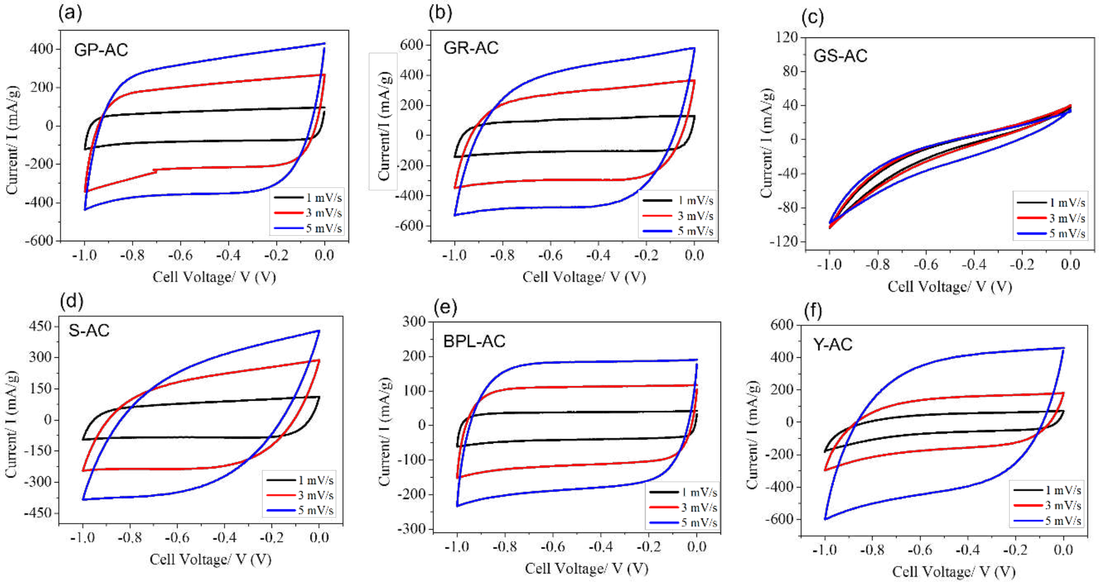

Figure 3-3 Cyclic voltammograms of garlic powder (GP), garlic roots (GR), garlic skin (GS), Supersorbed (S), BPL, and Y activated carbon (AC) supercapacitors at 1 mV.s-1, 3 mV.s-1, and 5 mV.s-1, respectively. The CVs were measured in a two-electrode configuration.

To quantify the kinetics of charge storage, surface-controlled, and diffusion-controlled capacitances were calculated using Trasatti's method [102], presented in the supporting information (Figure S3 and table S4). The best kinetic behavior was shown by the electrodes with higher double layer capacitance from outer surface (C_{DL}) and lower diffusion-controlled capacitance from the inner surface ($C_{Diffusion}$) and follows sequence from highest C_{DL} to lowest C_{DL} as; BPL-AC > GP-AC > Y-AC > GR-AC > S-AC > GS-AC. The details of the Trasatti method and calculations for capacitance contributions are discussed in the supporting information (section S1). EIS analysis was carried out to gain insights into the charge transport kinetics and contribution from different resistances

(Figure S4). The detailed quantification and analysis of solution resistance, charge transfer resistance, diffusion resistance, real capacitance, and imaginary capacitance for six different carbons is provided in section S2. The experimental setup for electrochemical testing is shown in Fig. S5.

3.3.2 Galvanostatic charging-discharging (GCD) and CO_2 adsorption analysis

Figure 3-4 shows the CO_2 concentration change with respect to time and voltage for 4 cm^2 electrodes in supercapacitive swing adsorption (SSA) experiments over five cycles. For each cycle, a decrease in concentration is initially observed as the electrodes are charged. Similarly, an increase in CO_2 concentration is observed during discharging the electrodes. At full saturation, the CO_2 concentration returns to a value of approximately 15 %, indicating the completion of adsorption/desorption half cycles. An increase in concentration somewhat above 15% near the end of the holding step at -1 V is seen for GP-AC, S-AC, and BPL-AC electrodes. This may be caused by some electro-oxidation of the activated carbon surface while the electrodes are charged during the first few cycles, forming additional CO_2. The phenomenon of carbon electro-oxidation is well-known from the related capacitive deionization technology, since the standard reduction potential for carbon oxidation is within the charging potential window.[103] The electro-oxidation effect fully disappears after twenty charging-discharging cycles (Figure S6), and the electrodes show highly reproducible adsorption-desorption behavior. The cycling of BPL carbon electrodes over 60 cycles shows consistent CO_2 adsorption-desorption behavior and stable SSA performance (Figure S7) without any measurable losses.

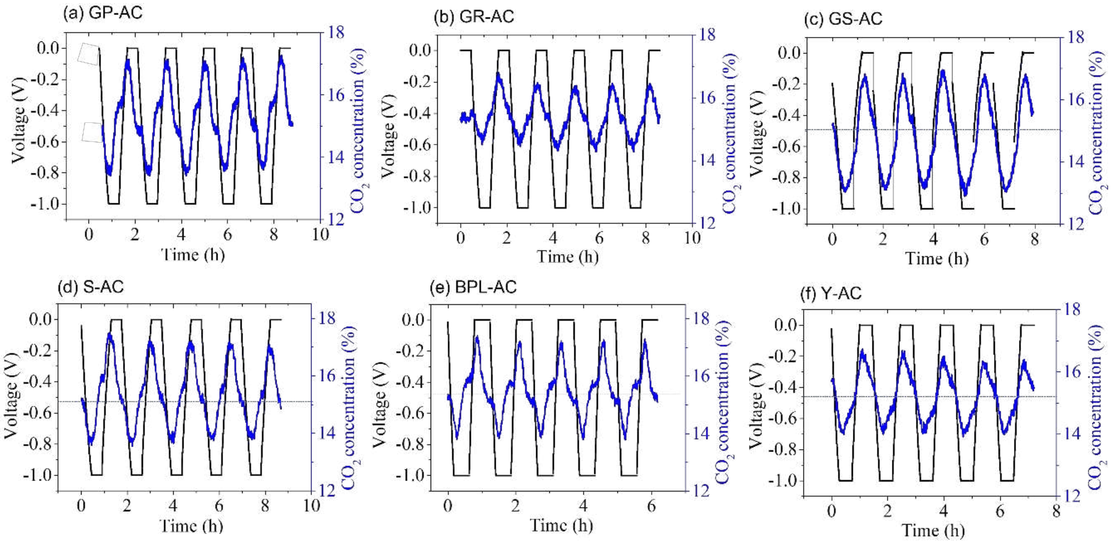

Figure 3-4 Voltage response (shown in black) and CO_2 concentration changes (shown in blue) for six different electrodes, garlic powder, GP-AC (a), garlic roots, GR-AC (b), garlic skin, GS-AC (c), supersorb, S-AC (d), BPL-AC (e), and Y-AC (f) The blue dotted line in the center of the plot denotes the equilibrium concentration of around 15 % CO_2. Electrodes with an area of 4 cm^2 and thickness of 0.7 mm were used for these experiments.

The GCD curves and CO_2 concentration profiles in Figure 3-4 were used to quantitatively evaluate the energetic and adsorptive performance of the electrodes (Figure 3-5 and Table S6). The specific capacitance of the electrodes followed the sequence GR-AC (257 $F.g^{-1}$) > GP-AC (233 $F.g^{-1}$) ≃ S-AC (230 $F.g^{-1}$) > GS-AC (196 $F.g^{-1}$) > Y-AC (135 $F.g^{-1}$) > BPL-AC (85.9 $F.g^{-1}$) (black dots in Figure 5a). The specific capacitance is inversely correlated with the density of the electrodes which follows the sequence GR-AC (0.19 $g.cm^{-1}$) < GS-AC (0.25 $g.cm^{3}$) < GP-AC (0.28 $g.cm^{-3}$) < S-AC (0.31 $g.cm^{-3}$) < Y-AC (0.48 $g.cm^{-3}$) = BPL-AC (0.48 $g.cm^{-3}$). Lower density tends to increase gravimetric specific capacitance due to higher porosity, and more effective utilization of the carbon atoms for EDL formation (a greater fraction of the carbon atoms is on a pore surface). GR-AC has the greatest specific capacitance and the lowest density (0.19 $g.cm^{-3}$). BPL-

AC and Y-AC have the highest densities and the lowest specific capacitances. An outlier is the GS-AC which has the second- lowest density, but only the fourth-highest specific capacitance. This may be explained by the significantly higher resistance in GS-AC. BPL-AC and Y-AC have the same density, but different specific capacitances, which may be attributed to their different raw materials (bitumen coal and carbide, respectively), and the different activation methods.

The gravimetric adsorption capacity of the electrodes increased significantly from 70 mmol.kg^{-1} for BPL-AC electrodes to 273 mmol.Kg^{-1} for GR-AC electrodes and followed the sequence GR-AC > GP-AC > GS-AC > S-AC > Y-AC > BPL-AC (blue dots in Figure 3-5a). The gravimetric adsorption capacity was calculated based on the mass of the top electrode without considering the mass of other cell components. The trend of increase in adsorption capacity is consistent with increasing specific capacitance of the electrodes, except for GS-AC and S-AC, which show the third and fourth highest adsorption capacity but flip positions for the trend in specific capacitance. The higher adsorption capacity of GS-AC (247 mmol.Kg^{-1}) as compared to S-AC (201 mmol.Kg^{-1}) can be attributed to its higher mesoporous surface area compared to S-AC, which ease the transport of ions and electrons for more effective utilization of surface area. GP-AC shows the second highest adsorption capacity (255 mmol.Kg^{-1}) while Y-AC shows the second lowest sorption capacity (84.5 mmol.Kg^{-1}), consistent with the specific capacitance trends. Activation treatment of carbons was necessary to achieve higher capacitance and higher adsorption capacity values. Without the activation treatment, biomass derived carbon showed negligible capacitance and no CO_2 sorption during charging/discharging. The electrodes prepared by mixing carbon black, gluten, and PTFE without the addition of activated carbon also showed very low adsorption capacity (< 30 mmol.kg^{-1}, Figure S8), arguing that high surface area activated carbons are indispensable for SSA. The results indicate that high surface area activated carbons with high specific capacitances investigated for supercapacitor research can be directly used for SSA.[104–106] Table S8 shows a comparison of capacitances of some recently reported biomass-derived porous carbon electrodes.

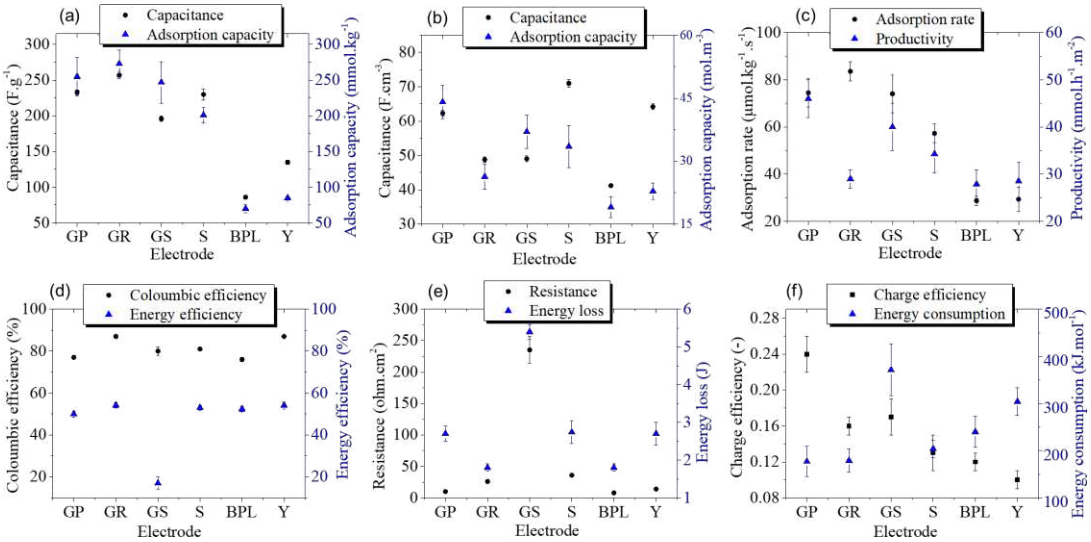

Figure 3-5 Gravimetric capacitance and gravimetric adsorption capacity (a), volumetric capacitance and volumetric adsorption capacity (b), adsorption rate and productivity (c), coulombic efficiency and energy efficiency (d), resistance and energy consumption (e), of biomass-derived (GP, GR, GS) and commercial (S, BPL, Y) activated carbon electrodes. The vertical lines on data points show error bars.

The volumetric performance metrics of the electrodes are also practically relevant because they influence land use, the capital cost for housing the modules, and the ratio between non-adsorbing components (current collector, separator, gas diffusion layer), and the adsorbing electrodes. The volumetric capacitance (C_V) of the electrodes follows the sequence: S-AC > Y-AC > GP-AC > GS-AC > GR-AC > BPL-AC (Figure 5b and Table S6). However, the volumetric adsorption capacities follow the sequence: GP-AC > GS-AC > S-AC > GR-AC > Y-AC > BPL-AC. Capacitance and adsorption capacity are not as strongly correlated on a volumetric basis, unlike gravimetric capacitance/adsorption capacity. GP-AC, GS-AC, and S-AC show the volumetric adsorption capacities of 65.3 $mol.m^{-3}$, 52.9 $mol.m^{-3}$, and 47.3 $mol.m^{-3}$ and exhibit volumetric capacitances of 62.3 $F.m^{-3}$, 49.0 $F.cm^{-3}$, and 71.3 $F.cm^{-3}$, respectively. The biggest discrepancy between capacitive and adsorptive performance exists for Y-AC which ranks second for capacitive, but fifth for adsorptive performance. The results indicate that volumetric adsorption capacity does not solely depend on the volumetric capacitance but also on factors such as the carbon source, surface functionalities, and pore size distribution. Nonetheless, the approximately four-fold improvement in gravimetric adsorption capacity (GR-AC) and two-fold improvement in volumetric adsorption capacity (GP-AC) as compared to BPL carbon electrodes show that biomass derived carbons can be an inexpensive and efficient source for capturing CO_2 using SSA, and there might be room for further improvement. Differences between gravimetric and volumetric adsorption performances can be explained by the different densities of the materials. GR-AC has the lowest density, and therefore this material is able to use the carbon mass most effectively. This does not translate to the highest volumetric capacity because the low density creates “wasted” pore space that cannot be used for adsorption. GP-AC has a higher density and is not as effective on a mass basis because less many carbon atoms are accessible for adsorption.

On the other hand, the higher density leads to less "wasted" pore space, which explains the high volumetric performance.

The kinetics of SSA for the different electrodes was studied by calculating the adsorption rate (AR, $\mu mol.kg^{-1}.s^{-1}$) and productivity (P, $mmol.h^{-1}.m^{-2}$) of CO_2 adsorption on the electrodes (Figure 3-5c and Table S6). The adsorption rate used here is defined as the number of moles of CO_2 adsorbed at the full adsorption capacity over the time required to reach full adsorption capacity, and the mass of the negative electrode. The adsorption rate followed the same sequence as gravimetric adsorption capacity, i.e., GR-AC > GP-AC > GS-AC > S-AC > Y-AC > BPL-AC. An approximately three-fold increase in adsorption rate was seen for GR-AC (83.6 $\mu mol.kg^{-1}.s^{-1}$) compared to BPL-AC (28.7 $\mu mol.kg^{-1}.s^{-1}$). This can be explained by greater porosity of GR-AC, which allows faster mass transfer, and improved kinetics. The productivity of the electrodes followed the same trend as the volumetric adsorption capacity, with GP-AC and GS-AC showing the highest productivities of 46.1 $mmol.h^{-1}.m^{-2}$ and 39.9 $mmol.h^{-1}.m^{-2}$, respectively. Since fast sorption kinetics and high productivity are directly related to the cost of CO_2 capture, a further increase in CO_2 adsorption rate and productivity would be highly desirable for SSA. Studies that quantitatively determine the factors that limit kinetics should be performed. One possibility is that slow CO_2 hydrolysis in the neutral electrolyte limits the kinetics. This could be addressed by the addition of CO_2 hydrolysis catalysts to the electrolyte. Possibly, also the pore surfaces of the activated carbon could be modified so that the carbon acts as a heterogeneous catalyst. In our XPS studies, GR-AC and GP-AC showed a higher degree of -OH functionality while GS showed both -OH and C-N functionality, and these three biomass-derived carbons exhibit the highest adsorption rates. These results argue that pore surfaces with nucleophilic, chemical functionalities may enhance the CO_2 sorption rates during capacitive charging/discharging of the electrodes.

The coulombic efficiency (η_c) of the electrodes lies in the range of 75-90% and follows the sequence GR-AC (87%) ≃ Y-AC (87%) > S-AC (81%) ≃ GS-AC (80%) > GP-AC (76%) ≃ BPL-AC (75 %) (Figure 3-5d). No correlation was found between η_c and any other parameter, suggesting that the ratio of charge recovered during discharging to the charge stored during charging depends specifically on the type of electrode material. Similarly, the energy efficiency (η_e) did not depend on any other performance metric and followed the sequence GR-AC (54.2%) ≃ Y-AC (54.1%) > S-AC (52.8%) > BPL-AC (52.4%) > GP-AC (49.6%) > GS-AC (16.7%) (Figure 5d). The exceptionally low η_e of GS-AC is due to the very high resistance (235 $\Omega.cm^2$) of these electrodes (Figure 3-5e). The higher resistance may be due to modified synthesis conditions and greater sp^3 character of GS-AC compared to other biomass-derived carbons, as shown in XPS surface chemical state analysis. Despite the high resistance, GS-AC electrodes showed high specific capacitance and high adsorption capacity, comparable to GP-AC and GR-AC. Among commercial carbons, S-AC shows the highest resistance due to its highest sp^3 character and smallest sp^2 character. BPL-AC, GP-AC, Y-AC and GR-AC exhibit reasonable resistance values of 7.2 $\Omega.cm^2$, 9.2 $\Omega.cm^2$, 13.6 $\Omega.cm^2$, and 25.5 $\Omega.cm^2$, respectively. The energy loss is lowest for BPL-AC electrodes and highest for GS-AC electrodes and follows the sequence BPL-AC (1.84 J) ≃ GR-AC (1.88 J) < GP-AC (2.73 J) ≃ S-AC (2.74 J) < Y-AC (2.78 J) < GS-AC (5.40 J) (Figure 3-5e and Table S6).

The charge efficiency (CE) signifies the ratio of adsorbed CO_2 over the charges stored in the electrodes. Biomass-derived activated carbons (GP-AC, GR-AC, and GS-AC) exhibit higher CE than commercial activated carbons (S-AC, BPL-AC, and Y-AC) and follow the sequence GP-AC (0.24) > GS-AC (0.17) > GR-AC (0.16) > S-AC (0.13) > BPL-AC (0.12) > Y-AC (0.10) (Figure 3-5f). High charge efficiency of biomass-derived electrodes is still far less than the theoretical maximum value of 1.0 (assuming the ionic liquid-solid mechanism as the only mechanism). Co-ion expulsion, competition of H^+/HCO_3^- with electrolyte ions in the double layer, and unwanted faradaic reactions (e.g., carbon oxidation, oxygen reduction) may hinder the CE to reach its maximum value.[45,103,107–109] In addition, the conversion of HCO_3^- ions to form CO_3^{2-} that have a greater affinity to the anode due to their higher negative charge may reduce the charge efficiency. CE ranging from 0.5 to 0.7 has been achieved by using ion-selective membrane, thinner electrodes (0.25 mm vs 0.70 mm used in this study), and pure DI water instead of salt solutions in a related membrane-capacitive deionization process (MCDI).[45] However, the added cost of membranes along with their mass-transfer limitations, mechanically weak electrodes with less absolute capacitance, and low ionic conductivity of the CO_2 sparged DI water are disadvantageous for capturing CO_2, especially at low concentrations. Separate studies requiring in-situ characterization are needed to gain insights about the adsorbed species at the double-layer, and possible faradaic surface reactions. These insights may then be used to improve the selectivity of the electrodes for H^+/HCO_3^- over the electrolyte ions.

The energy consumption (EC) signifies the amount of energy required to adsorb one mole of CO_2 and was calculated from the ratio of energy loss to absolute amount of CO_2 adsorbed. The overall sequence is as follows: GP-AC (177 kJ.mol^{-1}) < GR-AC (179 kJ.mol^{-1}) < S-AC (204 kJ.mol-1) < BPL-AC (243 kJ.mol^{-1}) < Y-AC (304 kJ.mol^{-1}) < GS-AC (371 kJ.mol^{-1}), (Figure 3-5f). GP-AC, GR-AC, and S-AC have higher surface areas and absorb larger amounts of CO_2 relative to the energy loss, thus resulting in smaller energy consumption values. However, despite the high surface area and high adsorption capacity of GS-AC, the very high energy loss results in large energy consumption. BPL-AC and Y-AC exhibit lower surface areas and adsorb much less amounts of CO_2 relative to the energy loss, resulting in higher energy consumption. Our group reported an energy consumption of ~100 KJ.mol^{-1} with 78% energy efficiency using 7 cm BPL-AC electrodes in 5M NaCl and 1M $MgBr_2$ electrolyte, arguing that improved energy consumption may be achievable by use of 5M NaCl, or 1M $MgBr_2$.[100] More recently, we reported energy consumption values of ~70 KJ.mol^{-1} using hot-pressed garlic-roots derived electrodes,[110] arguing that development of new electrode materials is another promising route to further minimize the energy consumption values.

3.3.3 Experiments with Scaled electrodes (49 cm^2 vs 4 cm^2)

We further investigated if the performance of the module was dependent on the size of the electrodes, by preparing additional electrodes having an increased area of 49 cm^2.

The voltage response and CO_2 concentration profiles for all the electrodes exhibit similar adsorption-desorption behavior (Figure 3-6). The overall change in concentration increased during charging and discharging, owing to the longer distance that CO_2 has to travel through the electrodes. Charging of 49 cm^2 GS-AC electrodes resulted in a CO_2 concentration decrease from 15 % to around 5 % (Figure 6c) while only 1-2 % decrease in CO_2 concentration was observed with 4 cm^2 electrodes. The size of the electrodes was limited only by the size of the Ti current collector end plates. Further scaling of the end plates would allow for even larger electrodes and may produce a pure N_2 effluent stream upon charging the SSA module.

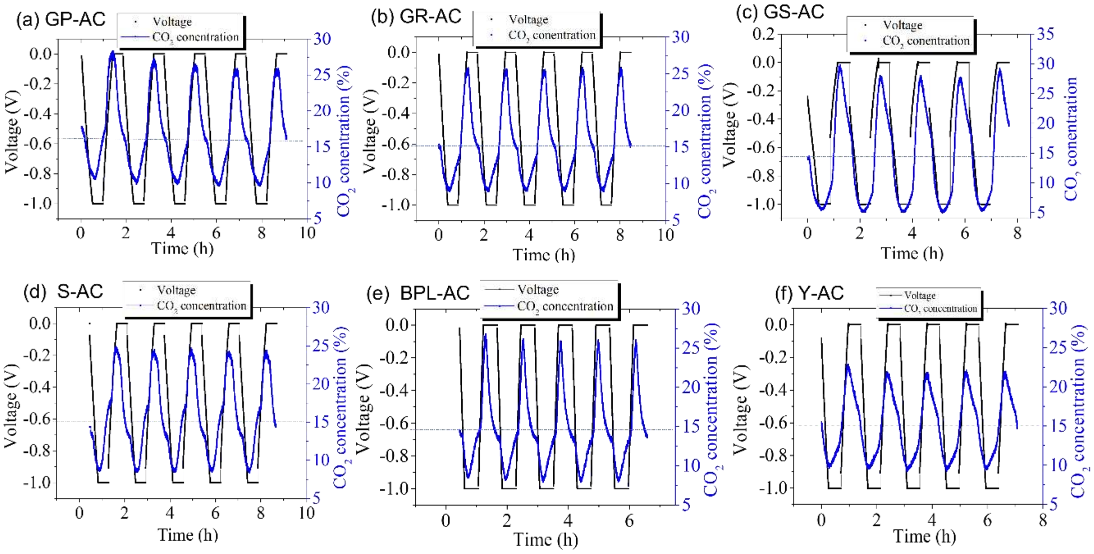

Figure 3-6 Voltage response (shown in black) and CO2 concentration changes (shown in blue) for six different electrodes, garlic powder, GP-AC (a), garlic roots, GR-AC (b), garlic skin, GS-AC (c), supersorb, S-AC (d), BPL-AC (e), and Y-AC (f) The blue dotted line in the center of the plot denotes the equilibrium concentration of around 15 % CO_2. Electrodes with an area of 49 cm^2 and thickness of 0.7 mm were used for these experiments.

The energetic and the adsorptive metrics for 49 cm^2 electrodes are shown in Figure 3-7 and Table S7. The trend of capacitance and gravimetric adsorption capacity is the same as 4 cm^2 electrodes, with GR-AC, GS-AC, and GP-AC exhibiting the maximum gravimetric adsorption capacities of 198 mmol.Kg^{-1}, 194 mmol.Kg^{-1}, and 189 mmol.Kg^{-1}, respectively. S-AC, Y-AC and BPL-AC show significantly lower values of 119, 69.2, and 62.8 mmol.kg^{-1} (Figure 3-7a and Table S7). The volumetric sorption capacity follows the sequence: GS-AC (36.7 mol.m^{-3}) ≈ GP-AC (36.3 mol.m^{-3}) > GR-AC (28.2 mol.m^{-3}) > S-AC (27.2 mol.m^{-3}), > BPL-AC (23.1 mol.m^{-3}) > Y-AC (20.5 mol.m^{-3}) (Figure 3-7b). This is similar to the trend seen for 4cm^2 electrodes. Generally, sorption capacities are lower for the 49 cm^2 electrodes on both a gravimetric and volumetric basis. Nonetheless, there is still a 3.2-fold improvement on a gravimetric basis (198 vs 62.8 mmol.kg^{-1}) and a 1.6-fold increase (36.7 mol.m^{-3} vs. 23.1 mol.m^3) on a volumetric basis compared to BPL-AC. The productivity, and the adsorption rates of 49 cm^2 electrodes are also less compared to 4 cm^2 electrodes. The lower adsorption capacity, adsorption rate, and productivity may be because the gas flow may not be exactly radial for the 49 cm^2 electrodes. There could be preferential gas flow from the center to the exit hole at the periphery of the bigger electrodes caused by a pressure gradient within the smaller void volume around the electrodes. Increasing this void space by increasing the size of the current collector plate may eliminate the pressure gradient inside the void space. The adsorption rate and productivity follow the same trend as gravimetric adsorption capacity and volumetric adsorption capacity, respectively (Figure 3-7c). The coulombic efficiency of 49 cm^2 electrodes is higher than for the 4 cm^2 electrodes (Figure 3-7d). GS-AC electrodes show a coulombic efficiency of 94.9%, indicating that the charge-discharge process is highly reversible. The energy efficiency and energy loss follow a similar sequence to 4 cm^2 electrodes with BPL-AC showing the highest energy efficiency (64.1%) and smallest energy loss (12.1 J) while GS-AC exhibits the lowest energy efficiency (14.8%) and highest energy loss (55 J) (Figure 3-7d and e). Generally, higher resistance values and lower capacitance values are seen for the 49 cm^2 electrodes as compared to the 4 cm^2 electrodes. This may be explained by the fact that the same torque (20 in.lb) was used to assemble the SSA modules with different electrodes sizes, possibly resulting in higher contact resistance for the 49 cm^2 electrodes. The results agree with EIS comparison of 4 cm^2 and 49 cm^2 BPL electrodes (Figure S9), where 49 cm^2 electrodes show slightly higher resistance and slightly lower specific capacitance as compared to 4 cm^2 electrodes. Adjusting the torque and packing pressure may result in a size-independent energetic performance of the SSA modules.

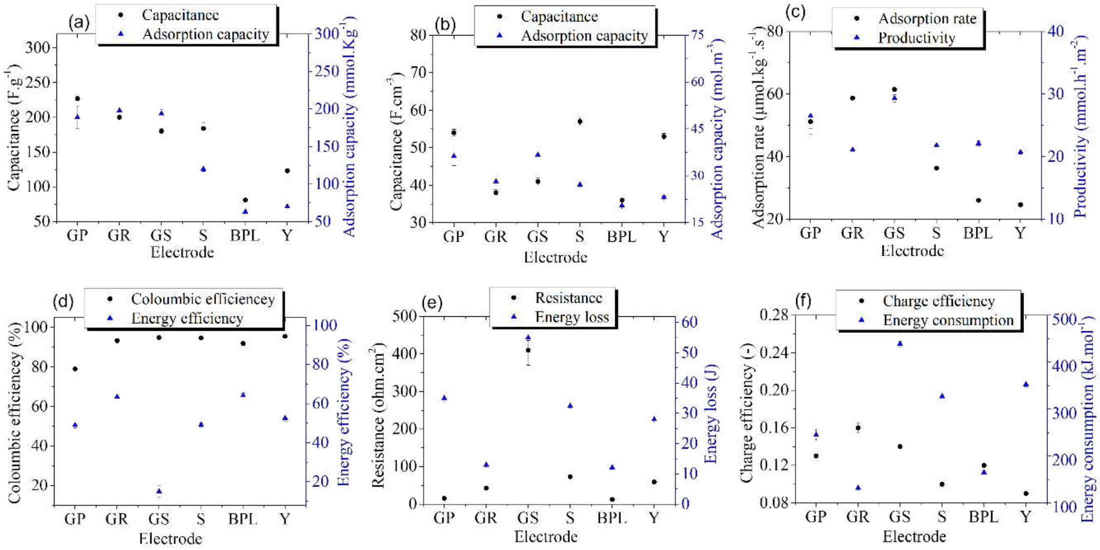

Figure 3-7 Gravimetric capacitance and gravimetric adsorption capacity (a), volumetric capacitance and volumetric adsorption capacity (b), adsorption rate and productivity (c), coulombic efficiency and energy efficiency (d), resistance and energy consumption (e), charge efficiency and energy consumption of biomass-derived (GP, GR, GS) and commercial (S, BPL, Y) scaled (49 cm^2) activated carbon electrodes.

The energy consumption is lowest for GR-AC electrodes and follow the sequence GR-AC (133 kJ.mol^{-1}) < BPL-AC (165 kJ.mol^{-1}) < GP-AC (245 kJ.mol^{-1}) < S-AC (327 kJ.mol^{-1}) < Y-AC (353 kJ.mol^{-1}) < GS-AC (439 kJ.mol^{-1}) (Figure 3-7f). Except GR-AC and BPL-AC, the 49 cm^2 electrodes exhibit higher energy consumption than 4 cm^2 electrodes. This can be attributed to lower energy loss and better energy efficiency of GR-AC and BPL-AC. Since the energy consumption is the ratio of energy loss to the moles of CO_2 absorbed, scaling GR-AC and BPL-AC from 4 cm^2 to 49 cm^2 led to about 7 times increase in energy loss and about 9 times increase in the moles of adsorbed CO_2. In contrast, scaling of GP-AC and S-AC lead to about 12 times increase in energy loss and about 7.5 times increase in the moles of CO_2 absorbed. GS-AC and Y-AC electrodes show about 10 times increase in energy loss and 8.5 times increase in the moles of adsorbed CO_2. The smallest increase in energy loss of GR-AC and BPL-AC explains the smallest energy consumption of these two electrodes. The charge efficiency of the electrodes follows the sequence: GR-AC (0.16) > GS-AC (0.14) > GP-AC (0.12) ≃ BPL-AC (0.12) > S-AC (0.10) > Y-AC (0.09) (Figure 7f). Similar to the energy consumption, the charge efficiency (CE) of 49 cm^2 GR-AC and BPL-AC electrodes stays the same as 4 cm^2 electrodes but significantly decreases for GP-AC, GS-AC, BPL-AC, Y-AC. These results argue that not only the energy loss but also the absolute number of moles of CO_2 adsorbed in case of GR-AC and BPL-AC is highest among other electrodes. Overall, 49 cm^2 electrodes results in improved purity of the effluent gas but requires further optimization to avoid scaling effects that influence adsorptive and energetic performance metrics.

3.3.4 Preliminary technoeconomic analysis

Garlic root-derived activated carbon has the highest gravimetric sorption capacity, and fastest adsorption kinetics. We therefore carried out a preliminary techno-economic analysis for the garlic roots derived carbon to estimate the cost of CO_2 capture using supercapacitive swing adsorption (SSA). The preliminary technoeconomic analysis is based on the established data from the literature and not solely on our experimental results.

The current annual world garlic production is about 28 million tons per year.[111] There is about 6% mass percent of garlic roots per mass unit of garlic.[112] Assuming a garlic root to activated carbon conversion rate of 20 %,[113] a maximum amount of 0.34 million tons of garlic root-derived activated carbon could be made per year. Based on the SSA sorption capacity of 0.20 mol/kg and 1h cycle times, this amount could capture ~26 million tons (Mt) CO_2 per year. Assuming a cycle life of 100,000 cycles, the sorbent would live 11.42 years, hence on an annualized basis 299 Mt CO_2/year could be captured, i.e. SSA with garlic-root derived carbons could be scaled up to this amount (see section S4 for calculations). Assuming a typical activated carbon production cost of \$3.00 per kg,[114] a cost of \$10.00/kg for the PTFE binder,[115] \$6.00/kg for the carbon black,[116] and \$1.35/kg for the gluten,[117] the cost of an electrode is \$3.38/kg at a AC:PTFE:CB:Gluten ratio of 80:5:5:10. At an electrode thickness of 0.7 mm, and electrode density of 0.20 g/cm^3, this translates to an electrode cost of \$0.47/m^2. Application of a Lang factor of 3.63 gives \$1.71/m^2 (calculation S6). The productivity at 0.20 mol/kg and 1h cycle times is 0.028 mol.h^{-1}m^2 or 0.0108 tons.m^{-2}year^{-1}. Assuming an interest rate of 3% and 11.42

years electrode lifetime gives a capital recovery factor of 0.10. This results in an annualized electrode cost of \$0.18/m^2 and carbon capture cost of \$16.82/ton CO_2. This does not yet consider the counter-electrode, the separator, and the electrolyte. The symmetric counter-electrode does not further increase adsorption; hence it doubles the cost to \$34.64/ton. The cost of electrolyte is negligible, but the separator increases the cost to \$75.91/ton CO_2 assuming a separator cost of \$1.2/m^2.[116] A further consideration is the expanded graphite current collectors (\$5/m^2),[115] and the carbon cloth as the gas diffusion layer (\$9/m^2).[118] Figure 3-8(a) shows the cost breakdown of these components. The number and thus cost of current collectors can be minimized by scaling the technique using bipolar electrodes in series similar to fuel cell stacks because then only two current collectors at the end of the stacks are needed. If, for instance, there was a stack of hundred 1m^2 electrodes, one would only need two 1m^2 current collectors, and hence they would not significantly add to the cost (to \$79/ton in this example case). The ionic current within a bipolar electrode must be interrupted to avoid the short-circuiting of the ionic circuit. This could be accomplished by “gluing” the positive and the negative electrode together using graphite cement to give the bipolar electrode, or by using carbon black containing polyethylene foils.[119] The graphite cement would clog the pores at the interface of the two electrodes interrupting the ionic circuit. At an estimated graphite cement cost of ~\$1/m^2 the carbon capture cost would increase to \$115/ton (calculation S8 to S12). The carbon cloth as the gas diffusion layer is the most expensive component (\$9/m^2), would increase cost greatly to \$432/ton. We are currently exploring cell designs without carbon cloth that use electrodes with imprinted gas flow channels. This possibility arises from the large thickness of our electrodes (~0.7 mm).

Sensitivity analysis shows how much room for cost reduction there is by the improvement of individual parameters (Figure 3-8(b)), here investigated for the sorption capacity, the electrode thickness, the electrode density, and the activated carbon cost based on a cell design without carbon cloth as gas diffusion layer at a cost base of \$115/ton as stated above. At a sorption capacity of 50, 100, 400, 600, 800, and 1000 mmol/kg, the cost changes to \$459, \$229, \$57, \$38, \$29, and \$23/ton, respectively. At an electrode thickness of 0.2, 0.4, 1.0, 1.3, 1.7, and 2.0 mm, the cost changes to \$317, \$176, \$90, \$77, \$67, and \$62. This is because the ratio the of adsorbing components (electrodes) relative to the non-adsorbing components (separator, carbon cement, current collector) increases with decreasing thickness. A change of electrode density to 0.05, 0.1, 0.3, 0.4, 0.6, and 0.8 $g.cm^{-3}$ (at constant gravimetric sorption capacity), changes the cost to \$359, \$196, \$88, \$74, \$60, and \$53, respectively for the same reasons. Reduced activated carbon cost (\$1.5/kg, \$0.75/kg) changes the capture cost to \$102, and \$97/ton. Increasing the activated carbon cost to \$6/kg, and \$12/kg, increases the capture cost to \$138, and \$185/ton, respectively. It can be seen that the greatest sensitivity exists for the sorption capacity, and that a moderate further improvement to values of 600 mmol/kg can reduce the cost to < \$50/ton (Figure 8 (b)). The cost of sorbent is least sensitive to CO_2 capture cost because the cost of the non-adsorbing components is higher. Increase of electrode density could be achieved by greater compression. A simple and effective way to reduce cost is to increase the thickness of the electrodes, as long as this can be done without significantly decreasing the adsorption rates and increasing energy consumption due to increased resistance in the supercapacitor. The energy cost at an energy consumption of 179 kJ/mol is \$56/ton at an electricity production cost of 5c/kWh (section S13). The contribution of energy cost would be reduced to \$31 at 100 kJ/mol, and \$16/ton at 50 kJ/mol, respectively.

The cost may be further reduced by crushing electrode stacks at the end of their lifetime, and using them as soil conditioner, similar to biochar. Biochar is currently sold at a price of \$2,500/ton indicating significant reductions in cost through the use of crushed, "spent" activated carbon electrode stacks as soil conditioner.[120] Regeneration of the activated carbon is another potential way to reduce cost.

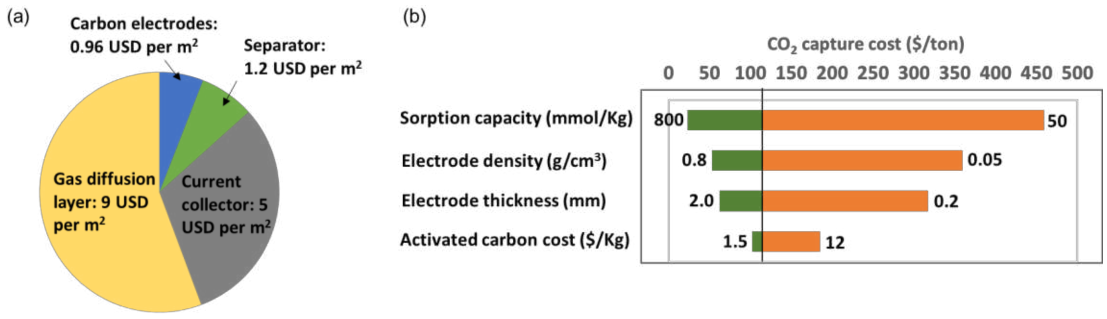

Figure 3-8 Cost breakdown of major components of the SSA module (a), Sensitivity analysis showing the influence of change in sorption capacity, electrode density, electrode thickness and activated carbon cost on the CO2 capture cost in \$/ton (b). The baseline at 115 \$/ton in (b) represents the cost achieved at an adsorption capacity of 200 mmol.Kg^{-1}, electrode density of 0.2 g.cm^{-3}, electrode thickness of 0.7 mm, and activated carbon cost of 3\$/ton.

The DOE 2025 cost target for post-combustion capture is \$40/ton CO_2.[121] Although the above techno-economic analysis is not comprehensive, it indicates that the SSA has the potential to reach the DOE cost targets with moderate improvements. For example, the target would be met at a sorption capacity of 0.6 mol/kg, an electrode thickness of 1 mm, an electrode density of 0.4 g/cm^3, and an energy consumption of 50 kJ/mol without considering the end-of-lifetime value of the electrodes. The SSA technology does not only appeal for separation of CO_2 from point sources (4-20% CO_2) but also from air (0.04%) due to the combination of chemical robustness, moisture-compatibility, selectivity, reversibility, and low cost of materials. An investigation on the applicability of SSA to DAC is currently on the way in our laboratory.

3.4 Conclusions

We evaluated three biomass-derived (garlic roots/skin/powder) and three commercially available carbons from different sources (bitumen coal, carbide, and coke) as electrode materials for supercapacitive swing adsorption (SSA). Galvanostatic charging and discharging coupled with SSA adsorption measurements showed that higher capacitance not only led to up to four times higher gravimetric adsorption capacities but also accelerated the adsorption rates and improved productivity. There is a positive correlation between specific capacitance and sorption capacity, arguing that the development of electrode materials with increased specific capacitance is a pathway to improve the sorption capacity. A quantitative overview over the relationships between capacitance and adsorption capacity shows that GR-AC (gravimetrically) and GP-AC (volumetrically) show the best CO_2 adsorption capacities among the tested electrodes. GR and GS are abundantly available biomass waste and can be used economically for activated carbon synthesis. The positive correlation between capacitance and adsorption capacity suggests that the ionic-liquid solid mechanism plays an important role in CO_2 adsorption and desorption. Scaling of electrodes resulted in improved purity of the effluent gas but requires further optimization to avoid scaling effects that influence adsorptive and energetic performance metrics. The techno-economic analysis shows that the improvements presented herein substantially increase the practical potential for SSA as carbon capture technique from a cost perspective.

3.5 Supporting Information

Table S1 Comparison of different electrochemical carbon capture methods.

Method	**Description**	**CO_2 source**	**Current density ($mA.cm^{-2}$)**	**Energy consumption ($kJ.mol^{-1}_{CO2}$)**	**Operation mode**
SSA[60,110]	Capacitive charge/discharge captures/concentrates CO_2	15%CO_2/85% N_2	~1	50-200	Cyclic (ref 17, 18, and **this work**)
MCDI[45]	Membrane capacitive deionization	15%CO_2/85% N_2	~0.1	50	Cyclic
BPMED[42]	pH-swing by electrochemical water splitting	0.5 M $KHCO_3$	20-140	200-400 (desorption)	Cyclic
Redox active Quinone[30]	Quinones in ionic liquid electrolyte	15%CO_2/85% N_2	~1	50-200	Cyclic
PCET[25]	pH-swing by proton coupled electron transfer	10-50% CO_2 balanced with N_2	20-150	60-150	Cyclic
Redox Tunable sp^2-N[36]	Redox tunable nitrogen centers in ionic liquid electrolyte	15% CO_2/5 % O_2/ 80% N_2	2	156	Cyclic
EMAR[37]	Electrochemically mediated main regeneration	15%CO_2/85% N_2	2-12	40-120 (desorption)	Cyclic
PSE[122]	Porous solid electrolyte reactor	14% CO_2/86% N_2	0.5-500	150-600	Continuous

EDCS[123]	Electrochemically driven CO_2 separator	400 ppm	NA	> 240	Continuous

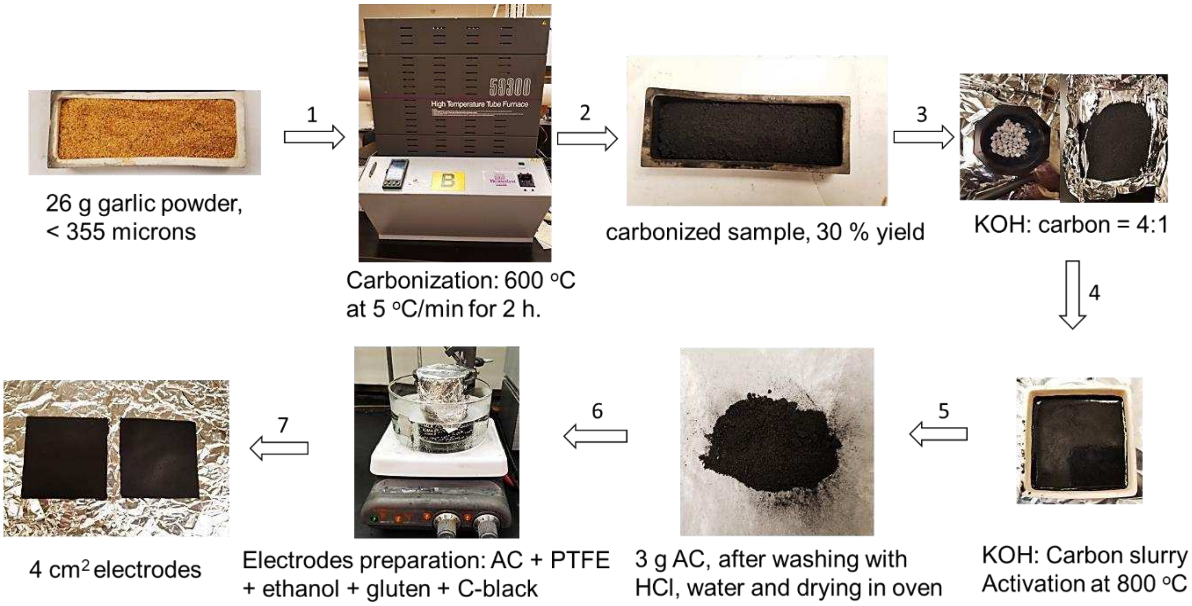

Figure S1. Scheme for the synthesis of activated carbon and preparation of electrodes. About 26 g of garlic was used as starting material. The yield after carbonization was around 30 %. The electrodes were prepared using a magnetic stirrer at 60°C for two hours and the obtained dough was flattened using pasta machine.

Table S2. Pore characteristics of activated carbons and electrode densities of 4 cm^2 electrodes.

Samples	**S_{BET} ($m^2.g^{-1}$)**	**S_{micro} ($m^2.g^{-1}$)**	**V_{pore} ($cm^3.g^{-1}$)**	**V_{micro} ($cm^3.g^{-1}$)**	**PSD (nm)**	**Electrode density ($g.cm^{-3}$)**
GP-AC	2341	1374	1.11	0.57	1.9	0.28
GR-AC	2582	238	1.41	0.10	2.2	0.19
GS-AC	2454	401	1.31	0.20	2.1	0.25
S-AC	2715	1412	1.31	0.59	1.9	0.31
BPL	1023	659	0.54	0.27	2.1	0.48
Y-AC	1109	685	0.60	0.29	2.1	0.48

(a) C1s spectra of activated carbons

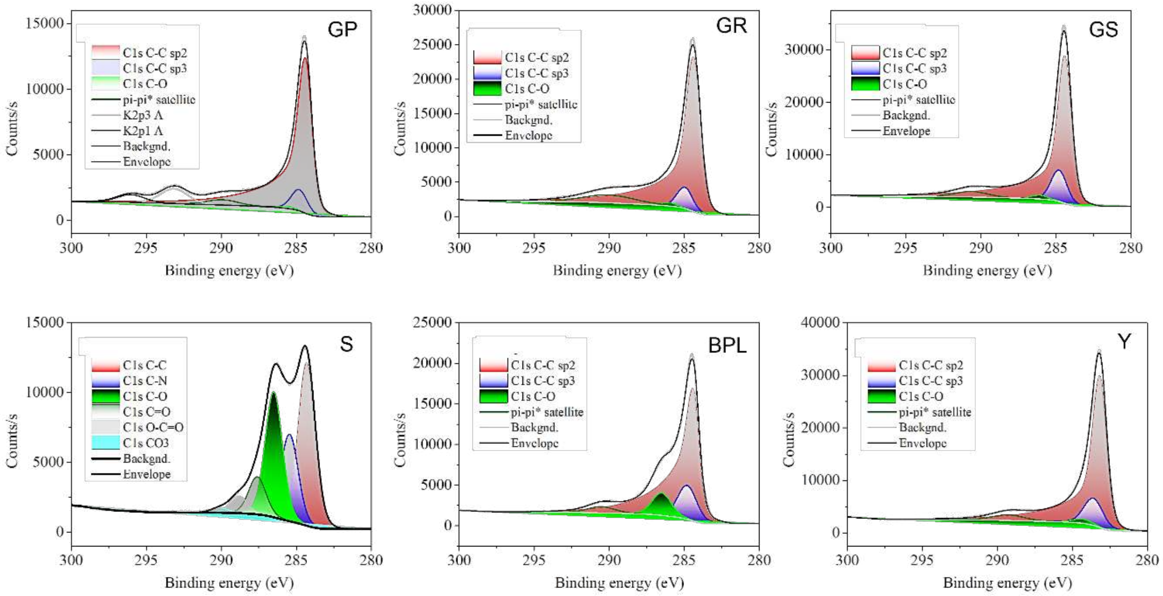

(b) O1s spectra of activated carbons

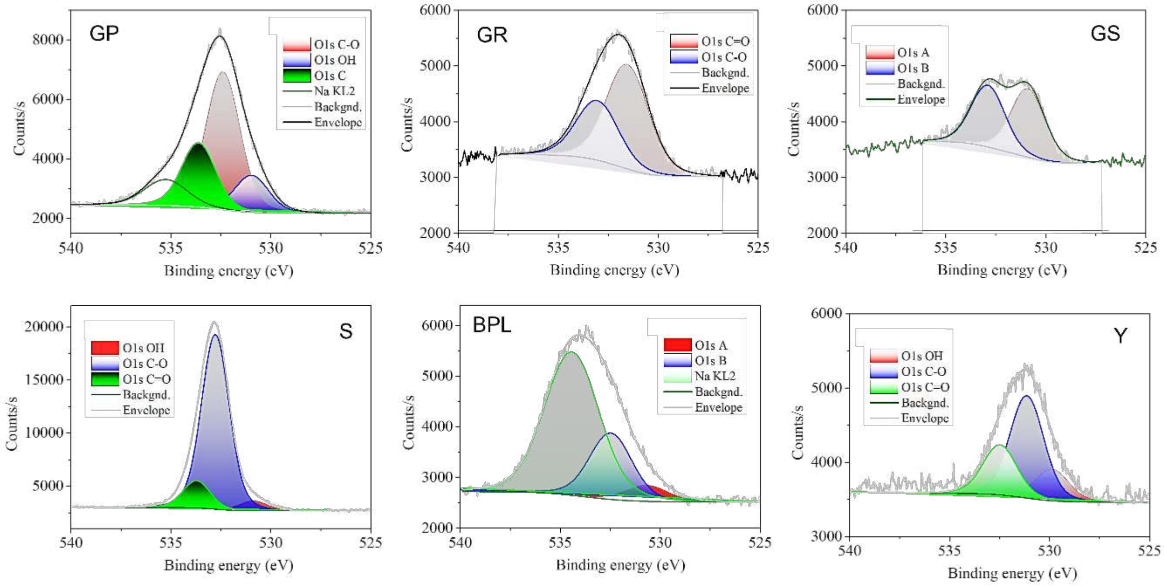

Figure S2 High resolution C1s (a) and O1s (b) spectra of garlic powder (GP), garlic roots (GR), garlic skin (GS), coke derived supersorb (S), coal derived (BPL), and carbide-derived (Y) carbons.

Table S3 Chemical state and compositional analysis of activated carbons.

Element	**Chemical state**	**BPL**	**GP**	**GR**	**GS**	**SAC**	**Y**
C	C-C_3 sp^2	64.52%	60.70%	83.53%	80.91%	28.20%	79.42%
	C-C_4 sp^3	12.80%	5.79%	7.94%	13.13%	15.07%	13.03%
	C-O_x-C_y	8.46%	0.56%	1.28%	1.58%	32.10%	2.02%
N	C-N	0.42%	-	-	0.59%	0.41%	0.54%
O	OH	0.66%	2.88%	3.95%	1.75%	1.09%	0.58%
	C-O_x-C_y	10.33%	15.81%	2.26%	1.58%	22.84%	2.80%
Na	-	-	2.44%	-	-	-	-
Al	Al_2O_3	1.11%	2.77%	0.39%	-	-	-
Si	SiO_2	1.40%	1.31%	0.52%	-	-	-
P	-	-	0.92%	-	-	-	-
S	C-S, SO_x	0.31%	-	-	0.36%	0.31%	0.35%
Cl	C-Cl	-	1.01%	0.15%	0.10%	-	1.26%
K	-	-	2.61%	-	-	-	-
Mg	-	-	3.18%	-	-	-	-

S1. Capacitance contributions from CV:

Trasatti method[102,124] was used to find the contribution of minimum double layer capacitance (from outer surface) and diffusion-controlled capacitance (from inner-surface). The cyclic voltammograms were collected in the range of scan rates from 1 to 5 $mV.s^{-1}$ and capacitance values were calculated at each scan rate using $C = Q/(\Delta V \times m)$, where Q is the total charge stored during charging, ΔV is the potential window, and m is the average mass of active material. A plot of capacitance versus the reciprocal of the square root of scanrate gives a linear relation $C = Rv^{-0.5} + C_{dl}$, where v represents the scan rate, R is the slope, and C_{DL} represents the minimum double layer capacitance. The C_{DL} values were calculated from the y-intercept of the above equation (Figure S3 (a) and Table S3). Similarly, plotting the reciprocal of capacitance versus square root of scanrate gives a linear relation $C^{-1} = Rv^{0.5} + C_T^{-1}$, where C_T is total capacitance, calculated from the y-intercept of Figure S3 (b). The difference between minimum double-layer capacitance (C_{DL}) and total capacitance (C_T) yielded diffusion-controlled capacitance. The results are shown in Figure S3 (c) and Table S3. The results for GS-AC are not shown because negative values of C_{DL} for GS-AC (column 2 in Table 1) refers to completely diffusion dominated charge storage and make the quantification of C_{DL} and $C_{Diffusion}$ from Trasatti method inapplicable in the range of 1 to 5 $mV.s^{-1}$.

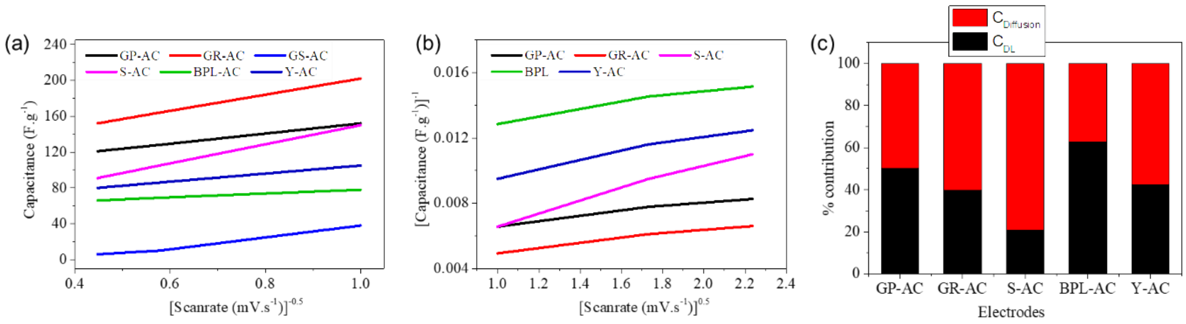

Figure S3 Dependence of reciprocal of square root of scanrate on capacitance to obtain the relation $C = Rv^{-0.5} + C_{dl}$ (a), dependence of square root of scanrate on reciprocal of capacitance to obtain the relation $C^{-1} = Rv^{0.5} + C_T^{-1}$ (b), percentage contributions of double-layer capacitance and diffusion-controlled capacitance for different electrodes.

Table S4 Linear relations obtained from the graphs of scan rates and capacitance for different electrodes (column 2 and column 3) and corresponding C_{DL}, $C_{Diffusion}$, and C_T values.

Electrode type	**$C = Rv^{-1/2} + C_{dl}$**	**$C^{-1} = Rv^{0.5} + C_T^{-1}$**	**C_{DL}**	**$C_{Diffusion}$**	**C_T**	**% C_{DL}**	**% $C_{Diffusion}$**
GP-AC	$C = 56.4v^{-1/2} + 95.9$	$C^{-1} = 0.0014v^{0.5} + 0.0052$	96.5	95.8	192	50.2	49.8
GR-AC	$C = 92.8v^{-1/2} + 110$	$C^{-1} = 0.0036v^{0.5} + 0.005$	110	168	277	39.6	60.4
GS-AC	$C = 59{,}7v^{-1/2} – 22$	-	-	-	-	-	-
S-AC	$C = 111v^{-1/2} + 41.3$	$C^{-1} = 0.0036v^{0.5} + 0.005$	41.3	159	200	20.7	79.4
BPL-AC	$C = 21.3v^{-1/2} + 56.5$	$C^{-1} = 0.0019v^{0.5} + 0.0111$	56.5	33.6	90.1	62.7	37.3
Y-AC	$C = 45.6v^{-1/2} + 59.8$	$C^{-1} = 0.0024v^{0.5} + 0.0071$	59.8	81.1	141	42.5	57.5

Note:

Misinterpreted in literature,[125–127] Trasatti method cannot be used to differentiate double-layer capacitance and pseudocapacitance. The misinterpretation was caused from the confusion that pseudocapacitance is diffusion-controlled while double-layer capacitance is surface-controlled. Both double-layer capacitance and pseudocapacitance can either be surface-controlled or diffusion-controlled. Pseudocapacitance involves chemical changes during charging/discharging and can be distinguished from double-layer capacitance by combining electrochemical methods with in-situ spectroscopic technique capable of monitoring the variation of element valence or chemical bonding.

S2. Electrochemical Impedance spectroscopy (EIS) analysis

EIS analysis was carried out to gain insights about the charge transport kinetics and contribution from different resistances (Figure S5). The solution resistance (R_S), charge transfer resistance (R_{CT}), and Warburg resistance (R_W) were calculated from the Nyquist plots (Figure S5a). The initiation of semicircle in the high-frequency region corresponds to the solution resistance of the electrodes. The solution resistance increases from 0.58 Ω for GP-AC to 1.21 Ω for GS-AC and follows the sequence GP-AC < BPL-AC < GR-AC ≃ S- AC < GS-AC, the values are given in Table S4. The width of semi-circle region in the Nyquist plots correspond to charge-transfer resistance of the electrodes. BPL-AC shows the lowest R_{CT} of 0.29 Ω while GS-AC shows the highest R_{CT} of 37.4 Ω, indicating the presence of charge transfer processes at the electrode surface. The charge transfer reactions can occur due to the presence of redox-active surface functionalities on activated carbons. The overall sequence of R_{CT} is as follows: BPL-AC < GP-AC < Y-AC < S-AC < GR-AC < GS-AC. The charge transfer resistance is followed by Warburg or diffusion resistance (R_w) in the intermediate to low frequency regions of the Nyquist plots. The smaller R_W indicates efficient diffusion of electrolyte ions deep inside the electrode pores. This is seen for GP-AC (0.61 Ω), Y-AC (0.97 Ω), S-AC (1.15 Ω), and BPL-AC (1.41 Ω) in the Nyquist plots. GR-AC and GS-AC exhibit higher resistance of 6.78 Ω and 36.4 Ω, respectively, indicating sluggish kinetics of pore utilization in the intermediate to low frequency regions. The appearance of quasi-vertical lines at lowest frequencies correspond to capacitive type behavior of the electrodes. The capacitance values at lowest frequencies (0.001 Hz) were calculated from the imaginary component of the Nyquist plot using equation 1 and are reported in Table S3. The relation between frequency and specific capacitance in Figure S5(b) provides further kinetic insights into the charge storage behavior of the electrodes. At high frequencies (10^5 Hz to 10^1 Hz), the electrolyte ions can only utilize the outer surface of the electrode and don't have enough time to access the pores, leading to very small and nearly constant capacitance in the high frequency region. As the frequency decreases from 1 Hz to 0.01 Hz, the pore utilization increases which leads to increase in capacitance values until the pores saturate with ions and the capacitance reaches a nearly constant value at the lowest frequency. Similar behavior is seen for all the electrodes except GS-AC, which shows a decrease in the capacitance after an initial increase in the low frequency region (Figure S5b). This maybe because GS-AC electrodes show higher resistance and higher deviation from the quasi-vertical line as compared to other electrodes (Figure S5a). The specific capacitance from

EIS at lowest frequency follows the sequence BPL-AC < Y-AC < GP-AC < GS-AC < S-AC < GR-AC. Deconvolution of the total capacitance into real capacitance (C_{real}) and imaginary capacitance (C_{imag}) provided additional insights into the charge storage behavior of supercapacitors (Figure S5c and d). C_{real} signifies the amount of charge reversibly stored at the electrode while C_{imag} signifies the energy dissipation from diffusion limitations and/or kinetically irreversible processes.[67,73,74] High C_{real} and low C_{imag} signifies reversible charge storage behavior and smaller diffusion resistance of the electrodes. Each electrode shows maximum C_{real} at the lowest frequencies except GS-AC. In contrast, C_{imag} reaches a maximum value at frequencies of around 0.01 Hz and then decreases for GP-AC, S-AC, BPL-AC, and Y-AC. The maximum value of C_{imag} at a particular frequency refers to the relaxation time (the time needed to discharge all the energy from the supercapacitor device with > 50 % efficiency).[128] The relaxation time follows the sequence BPL-AC ≃ GP-AC < Y-AC < S-AC < GR-AC < GS-AC. C_{imag} for GS-AC and GR-AC continue to increase at lowest frequencies and indicate the higher relaxation time needed to discharge the energy from the supercapacitor and slow kinetic behavior of these electrodes as compared to BPL-AC, GP-AC, Y-AC, and S-AC.

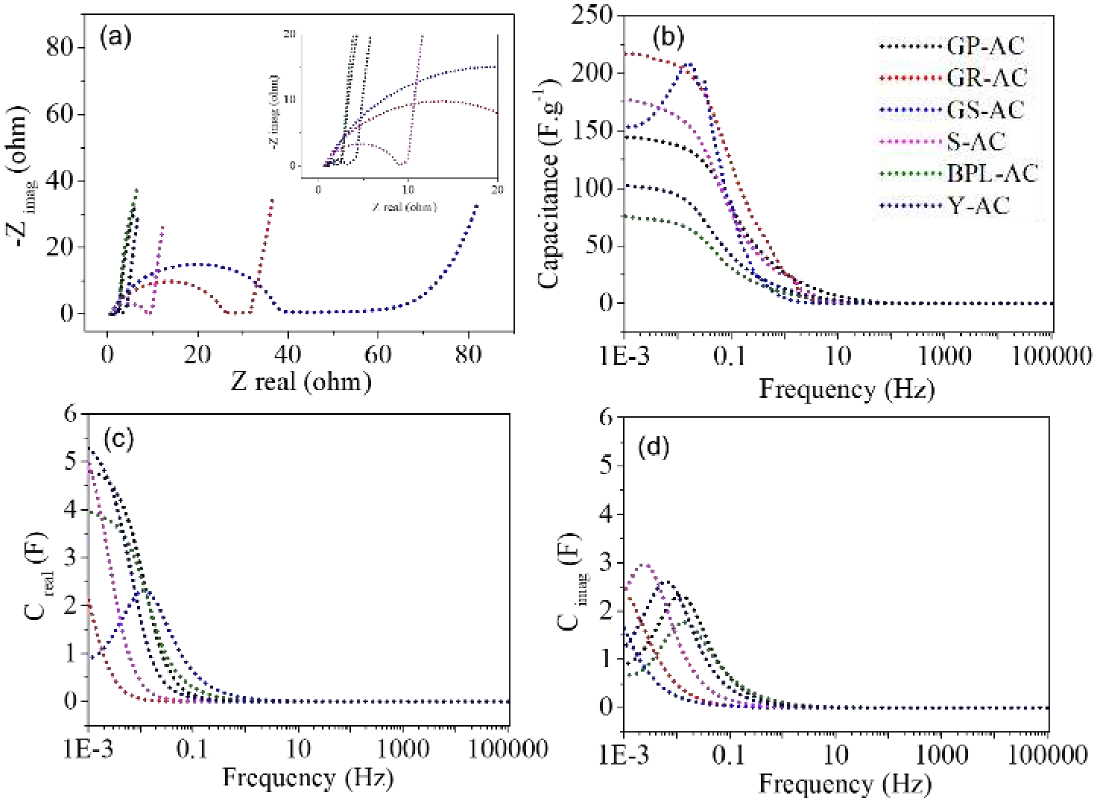

Figure S4 Nyquist plots obtained from electrochemical impedance spectroscopy (EIS) data for various electrodes analyzed in a two-electrode configuration (a). Dependence of capacitance on frequency showing the kinetics of charge storage (b). Frequency dependence of real capacitance (c) and imaginary capacitance (d). The color codes of dotted lines shown in (b) are consistent in all plots.

Table S5 Solution resistance (R_s), charge-transfer resistance (R_{CT}), Warburg resistance (R_W), total capacitance (C_T), real capacitance (C_{real}), and imaginary capacitance (C_{imag}) for different electrodes calculated from EIS data.

Electrode	**Rs (Ω)**	**R_{CT} (Ω)**	**R_w (Ω)**	**C_T (F)**	**C_{real} (F)**	**C_{imag} (F)**
GP-AC	0.58	1.29	0.61	4.96	4.79	0.884
GR-AC	0.88	25.3	6.78	4.61	2.78	2.95
GS-AC	1.21	37.4	36.4	4.69	0.69	1.79
S-AC	0.89	5.86	1.15	5.20	4.58	1.68
BPL-AC	0.70	0.29	1.41	4.09	3.97	0.69
Y-AC	0.96	2.14	0.97	5.51	5.27	1.22

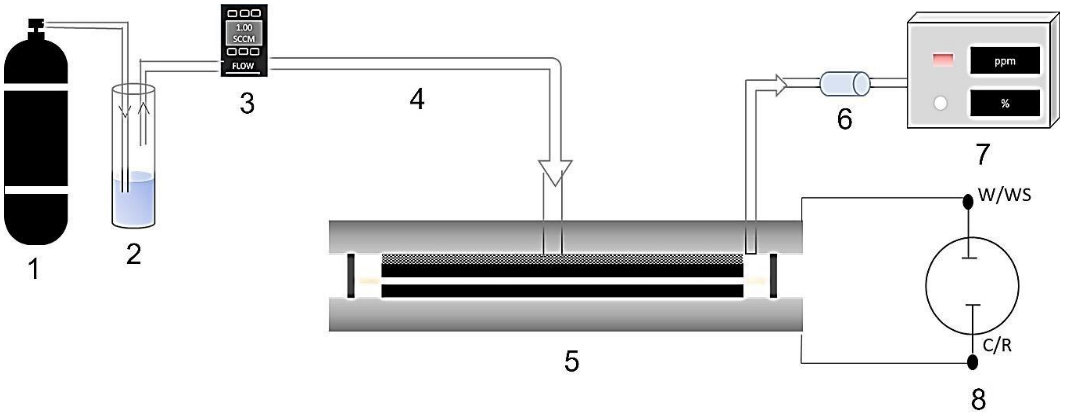

Figure S5 Schematic illustration of supercapacitive swing adsorption (SSA) apparatus in flow-through mode. 1: N2/CO2 gas cylinder, 2: Bubbler containing 1 M NaHCO3, 3: Mass flow controller, 4: Cu tubing, 5: supercapacitor module, 6: Drying tube, 7: CO_2 analyzer, 8: Potentiostat.

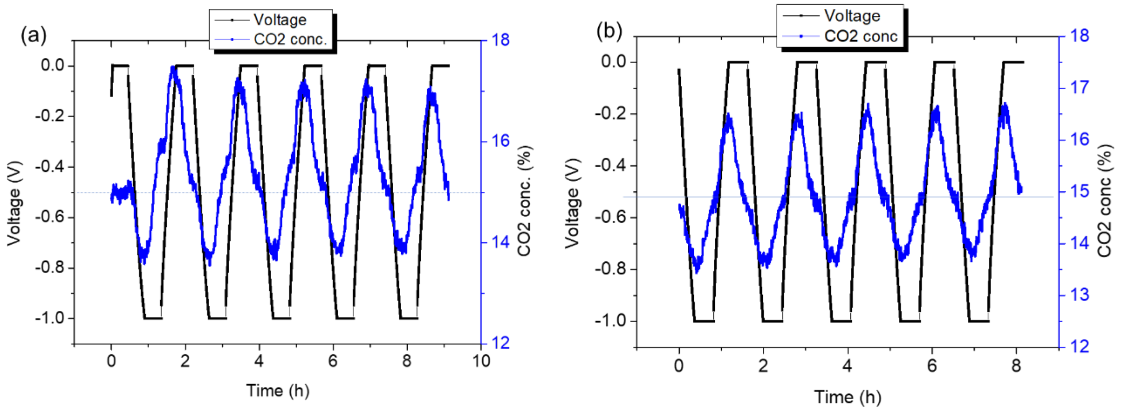

Figure S6 Voltage versus CO_2 concentration response of the newly assembled electrode pair (a), Voltage versus CO_2 concentration response of the same electrode pair after 20 cycles (b).

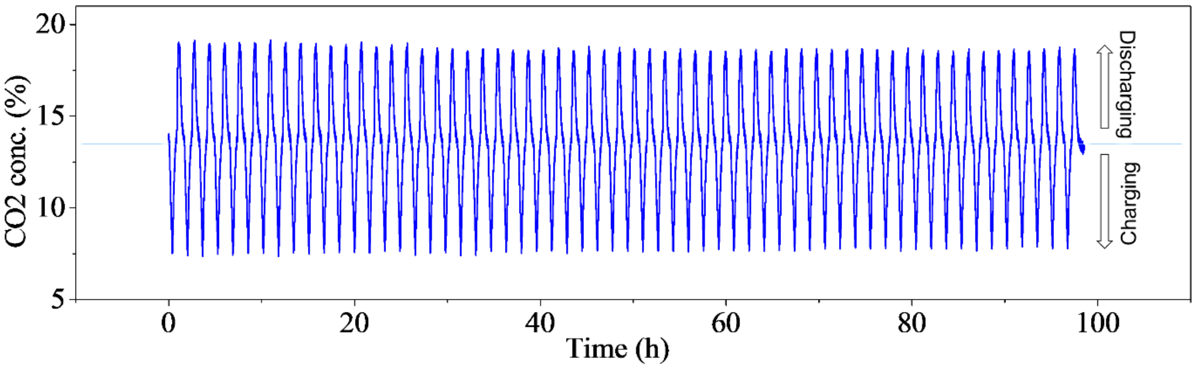

Figure S7 CO_2 concentration changes during 60 charging-discharging cycles show reproducible behavior. 49 cm^2 BPL-AC electrodes soaked in NaCl electrolyte were used for this study.

Table S6 Energetic and adsorptive performance metrics of the SSA with 4 cm^2 electrodes.

Parameter		**Garlic powder-AC**	**Garlic roots-AC**	**Garlic skin-AC**	**Supersorbed-AC**	**BPL-AC**	**Y-AC**
Energetic metrics @ 50 mA/g							
R_{ES} (Ω.cm^2)	at 0 V	9.2 ± 0.5	25.5 ± 2.1	235 ± 21	35.8 ± 1.8	7.16 ± 0.2	13.6 ± 0.3
	at -1 V	12.0 ± 0.1	33.7 ± 1.6	383 ± 23	47.1 ± 1.3	7.87 ± 0.1	14.7 ± 0.0
C_s (F.g^{-1})		233 ± 3.1	257 ± 5	196 ± 3.8	230 ± 8.0	85.9 ± 1.1	135 ± 3.0
C_A (F.cm^{-2})		4.17 ± 0.06	3.41 ± 0.05	3.43 ± 0.02	4.99 ± 0.07	2.88 ± 0.01	4.56 ± 0.06
C_V (F.cm^{-3})		62.3 ± 0.9	48.8 ± 0.8	49.0 ± 0.9	71.3 ± 1.1	41.2 ± 0.2	64.2 ± 0.8
Q_c (C)		6.75 ± 0.1	5.14 ± 0.05	5.62 ± 0.1	7.76 ± 0.2	4.65 ± 0.08	7.30 ± 0.1
t_g (s)		1566 ± 21	1466 ± 17	1227 ± 29	1718 ± 18	647 ± 6.1	1080 ± 9 .5
η_c (%)		76.2 ± 0.9	87.0 ± 0.5	80 ± 2.1	80.8 ± 0.5	75.1 ± 1.0	86.7 ± 1.1
η_e (%)		49.6 ± 1.4	54.2 ± 1.2	16.7 ± 0.24	52.8 ± 1.1	52.4 ± 1.3	54.1 ± 1.6
ΔE (J)		2.73 ± 0.2	1.88 ± 0.1	5.40 ± 0.16	2.74 ± 0.3	1.84 ± 0.1	2.78 ± 0.3
Adsorptive metrics @ 50 mA/g							
n_a, CO_2. (µmol)		17.6 ± 1.7	10.5 ± 1.1	14.8 ± 1.7	13.4 ± 0.8	7.59 ± 0.3	9.13 ± 1.2
AC (mmol.kg^{-1})		255 ± 27	273 ± 19	247 ± 29	201 ± 11	70.0 ± 5.3	84.5 ± 11
AC (mmol.m^{-2})		44.1 ± 4.7	26.3 ± 3.3	37.0 ± 4.4	33.5 ± 4.9	19.0 ± 2.2	22.8 ± 4.6
AC (mol.m^{-3})		65.3 ± 6.9	39.2 ± 4.1	52.9 ± 6.2	47.8 ± 7.0	27.1 ± 3.3	32.1 ± 6.3
AR (µmol.kg^{-1}.s^{-1})		74.5 ± 6.7	83.6 ± 4.8	74.1 ± 9.2	57.3 ± 4.5	28.7 ± 2.2	29.4 ± 5.9
P (mmol.h^{-1}.m^{-2})		46.1 ± 4.2	28.9 ± 2.2	39.9 ± 5.0	34.3 ± 4.5	27.9 ± 2.8	28.5 ± 4.0
CE (_)		0.24 ± 0.02	0.16 ± 0.01	0.17 ± 0.02	0.13 ± 0.02	0.12 ± 0.01	0.10 ± 0.01
EC (kJ.mol^{-1})		177 ± 32	179 ± 25	371 ± 55	204 ± 18	243 ± 33	304 ± 29
TEE (µmol.kJ^{-1}.s^{-1})		1.71 ± 0.3	1.71 ± 0.2	0.82 ± 0.12	1.39 ± 0.2	1.68 ± 0.1	1.14 ± 0.1

Table S7 Energetic and adsorptive performance metrics of the SSA with 49 cm^2 electrodes.

Parameter		**Garlic powder-AC**	**Garlic roots-AC**	**Garlic skin-AC**	**Supersorbed-AC**	**BPL-AC**	**Y-AC**
Energetic metrics @ 50 mA/g							
R_{ES} (Ω.cm^2)	at 0 V	15.5 ± 0.4	42.8 ± 0.9	410 ± 42	73.1 ± 4.5	12.3 ± 0.1	58.8 ± 0.6
	at -1 V	21.6 ± 0.7	65.2 ± 1.1	645 ± 55	89.2 ± 7.9	12.8 ± 0.2	64.5 ± 0.8
C_s (F.g^{-1})		227 ± 2.4	200 ± 0.5	178 ± 1.8	184 ± 2.2	80.8 ± 0.1	123 ± 0.1
C_A (F.cm^{-2})		3.75 ± 0.0	2.65 ± 0.0	2.86 ± 0.0	3.96 ± 0.1	2.59 ± 0.0	3.85 ± 0.0
C_V (F.cm^{-3})		53.6 ± 0.6	37.9 ± 0.1	40.8 ± 0.4	56.6 ± 0.7	35.6 ± 0.0	52.8 ± 0.1
Q_c (C)		84.8 ± 10	50.6 ± 0.2	55.7 ± 0.6	76.7 1.2	46.7 ± 0.1	71.0 ± 0.3
t_g (s)		1899 ± 21	1575 ± 4.0	1083 ± 14	1498 ± 18	647 ± 0.5	1011 ± 1.1
η_c (%)		79.0 ± 0.6	93.3 ± 0.1	94.9 ± 1.2	94.7 ± 1.0	91.9 ± 0.1	95.5 ± 0.1
η_e (%)		48.9 ± 0.8	63.4 ± 0.2	14.8 ± 0.2	49.1 ± 0.6	64.1 ± 0.1	52.6 ± 0.1
ΔE (J)		34.9 ± 1.2	12.8 ± 0.1	55 ± 0.9	32.5 ± 0.7	12.1 ± 0.1	28.0 ± 0.1
Adsorptive metrics @ 50 mA/g							
n_a, CO_2. (μmol)		133 ± 12	96.8 ± 0.7	126 ± 3.1	97.5 ± 2.1	71.2 ± 4.7	79.2 ± 1.2
AC (mmol.kg^{-1})		189 ± 17	198 ± 1.4	194 ± 4.8	119 ± 2.5	62.8 ± 4.2	69.2 ± 1.1
AC (mmol.m^{-2})		27.1 ± 2.6	19.7 ± 0.1	25.6 ± 0.6	19.9 ± 0.4	14.9 ± 0.3	16.2 ± 0.2
AC (mol.m^{-3})		36.3 ± 3.4	28.2 ± 0.2	36.7 ± 0.9	27.2 ± 0.6	20.5 ± 0.4	23.1 ± 0.3
AR (μmol.kg^{-1}.s^{-1})		51.2 ± 5.0	58.7 ± 0.3	61.5 ± 1.3	36.3 ± 0.6	26.4 ± 0.5	24.6 ± 0.4
P (mmol.h^{-1}.m^{-2})		26.5 ± 2.6	21.1 ± 0.1	29.3 ± 0.6	21.8 ± 0.4	22.1 ± 0.4	20.7 ± 0.3
CE (_)		0.12 ± 0.0	0.16 ± 0.0	0.14 ± 0.0	0.10 ± 0.0	0.12 ± 0.0	0.09 ± 0.0
EC (kJ.mol^{-1})		245 ± 12	132 ± 0.9	439 ± 5.7	327 ± 3.1	165 ± 4.1	353 ± 5.0
TEE (μmol.kJ^{-1}.s^{-1})		1.03 ± 0.1	2.24 ± 0.0	0.72 ± 0.0	0.93 ± 0.0	2.47 ± 0.1	1.01 ± 0.0

Table S8 Summary of capacitances from high mass-loading biomass-based porous carbons electrodes

Activated carbon source	**Surface area (m^2g^{-1})**	**Mass loading ($mg.cm^{-2}$)**	**Specific capacitance ($F.g^{-1}$)**	**Areal capacitance ($F.cm^{-2}$)**	**Reference**
Garlic roots	2582	12	257	3.4	This work
Garlic skin	2454	18	196	3.4	This work
Garlic powder	2341	17	233	4.2	This work
Soybean root	2690	20	205	4.1	[129]
Wheat bran	2562	20	154	3.1	[130]
Orange peel	860	23	186	4.3	[131]
Lignin	803	14	208	3.0	[132]
Pine tannin	2457	38	262	10	[133]
Coffee ground	2884	12	324	3.9	[134,135]

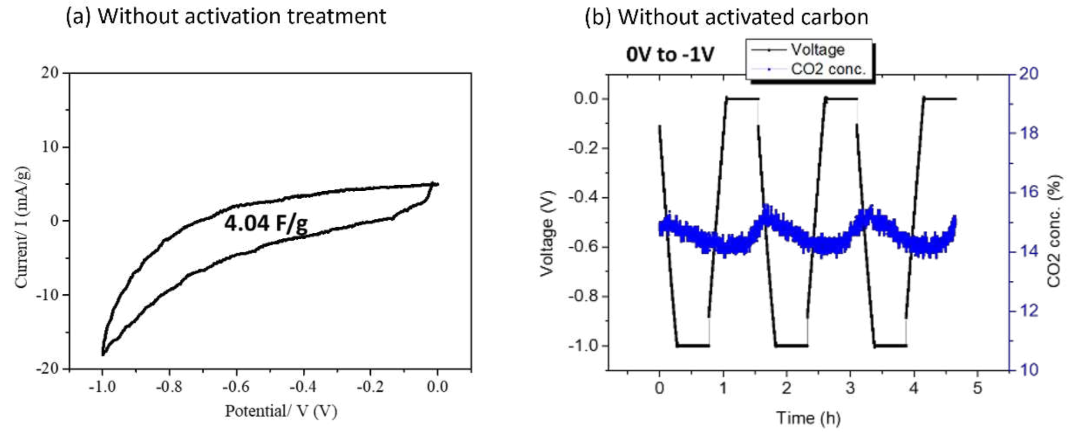

Figure S8. CV of GP-AC at 5 mV/s without the activation treatment showing very small capacitance and large deviation from EDL behavior (a), voltage vs CO_2 concentration changes of electrodes (containing 85% carbon black, 10% gluten, and 5% PTFE) without using activated carbon showing very low sorption capacity

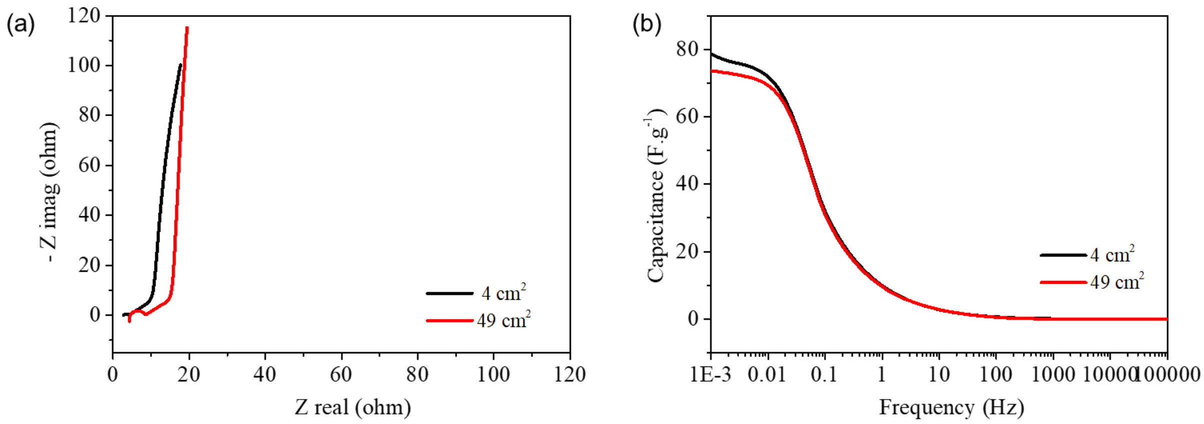

Figure S9. Nyquist plots of 4 cm^2 (black curve) and 49 cm^2 (red curve) BPL electrodes (a) and dependence of capacitance on frequency (b).

S3. Theoretical adsorption capacity calculations:

At V = 1V and C = 1000F/g, about 500 C of charges could be stored per gram of each electrode in a symmetrical supercapacitor. Assuming the ionic liquid solid mechanism and 100% charge efficiency ($n_{HCO3^-}/n_c = 1$), $n_{HCO3^-} = n_C = n$.

Since, Q = nF ⇒ n = Q/F = (500 C/g)/96485 C/mol = 0.00518 mol/g = (0.00518 *1000) mol/Kg

⇒ n = 5.2 mol/Kg

Similarly, at V = 1.5 V, about 750 C of charges could be stored per gram of each electrode in a symmetrical supercapacitor.

⇒ n = Q/F = (750 C/g)/(96485 C/mol) = 0.00777 mol/g = (0.00777 *1000) mol/Kg

⇒ n = 7.8 mol/kg

Technoeconomic analysis

S4. Calculations for CO_2 capture using garlic roots-derived activated carbon:

Global garlic production = 28 million tons per year

Garlic roots available per 28 million tons garlic = 6 % of 28 million = 1.68 million tons per year

Activated carbon production from garlic roots at 20 % yield = 0.2 × 1.68 million tons = 0.34 million tons per year

Since, 1 Kg of activated carbon can adsorb 0.2 mol of CO_2 in 1 hour, 0.34 million tons AC can adsorb 0.2 × 0.34 × 1000 × 1000000 = 6.8×10^7 mol CO_2 in 1 hour. Converting mol per hour to million tons per year yields,

$\Rightarrow$ (6.8×10^7 mol/h)(44g/1mol)(1ton/10^6 g)(1 million ton/10^6 ton)(8760hr/1year) = 26.2 million tons CO_2/year

Assuming a cycle life of 100,000 cycles, and 1 h cycle time, the sorbent would live for 11.42 years.

Hence, on an annualized basis: 26.2 × 11.42 = 299 Mt CO_2/year could be captured

S5. Cost of electrode per kg:

Component	wt%	Cost $/kg
Activated carbon	0.80	3.00
binder	0.05	10.00
Carbon black	0.05	6.80
Gluten (Alibaba)	0.10	1.35

Cost of electrode: per kg = $(0.8*3+0.05*10+0.05*6.8*0.10*1.35)kg = $3.38/kg

S6. Cost of electrode per m^2:

Density of electrode: 0.2 g.cm^3 = 200 kg/m^3

Thickness of electrode: 0.7 mm = 0.7*10^{-3} m

Cost of electrode per m^3 = \$3.38/kg * (200 kg/m^3) = \$676/m^3

Cost of electrode per m^2 = \$676/m^3*0.7*10^{-3} m = \$0.47/m^2

Land factor: 3.63

Cost of electrode per m^2 including Lang factor: \$0.47/m^2*3.63 = \$1.71/m^2

S7. Cost of electrode, counter-electrode, separator (ECS) assembly per m^2:

Cost of separator = \$1.2/m^2

Cost of ECS = (\$0.47+\$0.47+\$1.2)/m^2 = \$2.14/m^2

Cost of ECS with Lang factor = \$2.14/m^2*3.63 = \$7.768/m^2

S8. Assembly cost assuming stack with 100 electrodes (A200) including counter-electrode, separators, current collectors, electrolyte, and graphite cement per m^2 electrode.

Cost of current collector (expanded graphite): \$5/m^2

Area of current collector used in a 100-electrode stack per m^2 electrode =

\$5/100=\$0.05/m^2

Cost of graphite cement: \$1/m^2 (assuming graphite cement layer thickness of 25 microns)

Cost of A200 = (\$2.14+\$0.05*2+\$1)/m^2 = \$3.245/m^2

Cost of $NaHCO_3$: \$0.15/kg

Cost of water: \$6/m^3 = 0.6c/L

Molar mass $NaHCO_3$ = 84 g/mol

Density $NaHCO_3$ = 2.2 g/cm^3

Molar Volume $NaHCO_3$ = (84 g/mol)/(2.2 g/cm^3)=38.2 cm^3/mol

Cost of 1L 1M $NaHCO_3$ solution = (1L-0.0382L)*\$0.006+\$0.15/kg*0.084kg = \$0.0184/L

Separator+counter-electrode volume for 1m^2: 1m^2*(0.115*10^{-3}m+0.7*10^{-3}m) = 0.815*10^{-3} m^3

Assuming 50% pore volume required electrolyte volume for 1m^2 electrode area is 0.815*10^{-3} m^3/2=0.408*10^{-3}m^3 = 0.408 L

Cost of electrolyte for 1 m^2 electrode area = 0.408 L*\$0.0184/L = \$0.0075/m^2

Cost of A200 with electrolyte = \$(3.245+0.0075)/m^2 = \$3.2575/m^2

Cost of A200 with electrolyte and Lang factor = 3.63*3.2575 = \$11.81/m^2

S9. Assembly cost per m^2 electrode with additional gas diffusion layer (GDL):

A200+GDL = (\$3.245+\$9)/m^2 = \$12.245/m^2

Cost including Lang factor = \$12.245*3.63=\$44.45/m^2

S10. Annualized assembly cost (capital cost) per m^2

Electrode cycle life: 100,000 cycles

Cycle time: 1h

Electrode lifetime [years] = (100,000*1h)/(24*365 h/year) = 11.43 years

Interest rate: 3% (0.03)

Capital recovery factor = (0.03*(1+0.03)^11.43)/((1+0.03)^(11.43-1)) = 0.1047

Annualized capital cost without GDL = \$11.81/m^2*0.1047 = \$1.24/m^2

Annualized cost with GDL = \$44.45*0.1047=\$4.66/m^2

S11. Amount of CO_2 separated per m^2 and year (assuming 1h cycle times):

Gravimetric sorption capacity: 0.2 mol/kg

Gravimetric Productivity at 1h cycle time: 0.2 mol.kg^{-1}.h^{-1}

Volumetric productivity: 0.2 mol.kg^{-1}h^{-1}*(200kg/m^3) = 40 mol.m^{-3}.h^{-1}

Productivity per m^2 electrode and hour = 40 mol.m^{-3}h^{-1}*0.7*10^{-3}m = 0.280 mol.m^{-2}.h^{-1}

Productivity per m^2 electrode and year = 0.280 mol.m^{-2}h^{-1}*24h/day*365days/year=245 mol.m^{-2}.year^{-1}

Productivity in tons of CO_2 per m^2 and year = 245 $mol.m^{-2}.year^{-1}$*($44g.mol^{-1}$/(10^6 $tons.g^{-1}$)) = 0.01079 $tons.m^{-2}.year^{-1}$

S12. Annualized capital cost in \$/ton CO_2

Cost without GDL = \$1.24 $m^{-1}.year^{-1}$ / 0.01079 $tons.m^{-2}.year^{-1}$= \$114.59/ton

Cost with GDL = \$432.9/ton

S13. Calculation of energy cost

Cost of electrical energy: 5c/kWh

Cost of electricity in \$/GJ = (\$0.05/kWh)/(0.0036 GJ/kWh) = \$13.89/GJ

Energy consumption: \$179 kJ/mol CO_2 = (\$179 kJ/mol/($44g.mol^{-1}$*10^6 g/ ton))/10^6 kJ/GJ = 4.07 GJ/ton

Cost of energy per ton CO_2 = \$13.89/GJ*4.07 GJ/ton = \$56.5/ton

CHAPTER 4: HIGH VOLTAGE SUPERCAPACITIVE SWING ADSORPTION OF CO_2

This chapter has been published as: High-Voltage Supercapacitive Swing Adsorption of Carbon Dioxide, ***Small***, 2207834 (2023) https://doi.org/10.1002/smll.202207834

4.1 Introduction

Electrochemical CO_2 capture methods are currently gaining increased attention due to their potentially lower energy consumption and their ability to be coupled with renewable power sources.[32,40] These methods rely solely on the application of potential or current to capture CO_2 either through pH modulation,[35] redox-active agents,[23,38] or capacitive adsorption.[45,58] Currently, the majority of these electrochemical methods require expensive ion-selective membranes, electrode materials, and solvents.[31,136] In contrast, supercapacitive swing adsorption (SSA) only requires the use of robust, inexpensive, and environmentally benign activated carbon electrodes, a separator, and an aqueous electrolyte to capture and release CO_2. Compared to redox techniques, it offers the advantage of longer sorbent (electrode) lifetime, high round-trip energy efficiency, and fast charge/discharge cycles. However, the performance of SSA was largely limited by the low CO_2 sorption capacity (~60 mmol/kg) and slow sorption rate (24 $\mu mol.kg^{-1}.s^{-1}$). Our group discovered that biomass-derived activated carbons from garlic skin, garlic roots, and garlic clove powder lead to about 3-4 times increase of the gravimetric adsorption capacity and adsorption rate, and there is a strong positive correlation between capacitance and CO_2 capture performance.[137] Recently, Forse et al. reported that the gravimetric sorption capacity of SSA can be increased from 50 to 112 mmol.kg^{-1} by charging the electrodes between -1 V to +1 V instead of -1 V to 0 V, but this approach resulted in a very high energy consumption (751 kJ/mol CO_2).[95] To meet the 2025 DOE cost target for post-combustion CO_2 capture (~ 40$/ton),[121] a significant decrease in SSA energy consumption and further increase in SSA adsorption capacity is desirable. To reduce cost, the use of thicker and denser electrodes with a higher mass loading is advantageous because it increases the ratio of the adsorptive (activated carbon) versus the non-adsorptive (separator, gas diffusion layer, current collector) components. One challenge is to maintain high capacitances, high CO_2 sorption capacity, fast charge transport kinetics, fast sorption rates and low energy consumption at higher mass loadings due to less efficient gas permeation and ion diffusion as well as a greater resistor length.[138]

Herein, we show the overcoming of this challenge through the demonstration of novel, high-mass loading garlic-roots derived activated carbon-based (GR-AC) electrodes with improved adsorptive and energetic performance. We show that the SSA adsorption capacity can be further increased by increasing the voltage window without substantially compromising the energy consumption. Although the thermodynamic potential window of aqueous supercapacitors is limited to 1.23 V, a higher voltage window is possible because of the high hydrogen evolution and oxygen evolution reaction overpotential of carbon-based electrodes in neutral electrolytes.

4.2 Results and Discussion

Garlic roots derived activated carbon was prepared using an improved method which is illustrated in Scheme 1. K_2CO_3 was used as the activating agent instead of KOH. Compared to KOH, K_2CO_3 is cheaper, little toxic, less corrosive, and offers a higher yield.[113,139] The activated carbon obtained after K_2CO_3 activation was subsequently heat-treated in air to introduce oxygen surface functionalities (e.g., carbonyl, quinone)[140] on the carbon surface and to improve the capacitance of the activated carbon due to enhanced hydrophilicity of the pores. The electrodes were prepared by mixing the activated carbon, binder, and solvent, and subsequent hot-pressing the resulting dough between two steel plates at 50°C and 10,000 pounds to obtain 1 mm thick electrodes with a high mass-loading of 38 mg/cm^2 (Electrode area = 36 cm^2). The electrodes prepared without oxidation treatment showed less resistance but poor interparticle adhesion and could not be used for SSA. The detailed synthesis and electrodes preparation procedure is discussed in the supporting information (section S1).

Scheme 1. Main steps for the synthesis of garlic roots-derived activated carbon and electrodes assembling.

The N_2 sorption isotherm of garlic roots-derived activated carbon (GR-AC) shows a combination of a type I and type IV isotherms (Figure 4-1a). The steep uptake at low relative pressure ($P/P_o \leq 0.01$) indicates that the majority of adsorption takes place in the micropores (type I). At $P/P_o > 0.4$, the curve shows a hysteresis loop, indicating the presence of mesopores along with micropores (type IV). The hysteresis loop at higher relative pressures is commonly observed due to capillary condensation in the mesopores.[141] The BET surface area (S_{BET}) and microporous surface area (S_{micro}) of GR-AC is determined to be 1464 m^2g^{-1} and 1208 m^2g^{-1}, respectively. The pore size distribution curve shows a maximum differential pore volume at around 0.6 nm (Figure 4-1b), and pore volumes of 0.75 cm^3g^{-1} (V_{total}) and 0.47 cm^3g^{-1} (V_{micro}), respectively. Pore size versus cumulative and incremental pore volume in Figure S1 further confirms the micro-mesoporous structure of GR-AC.

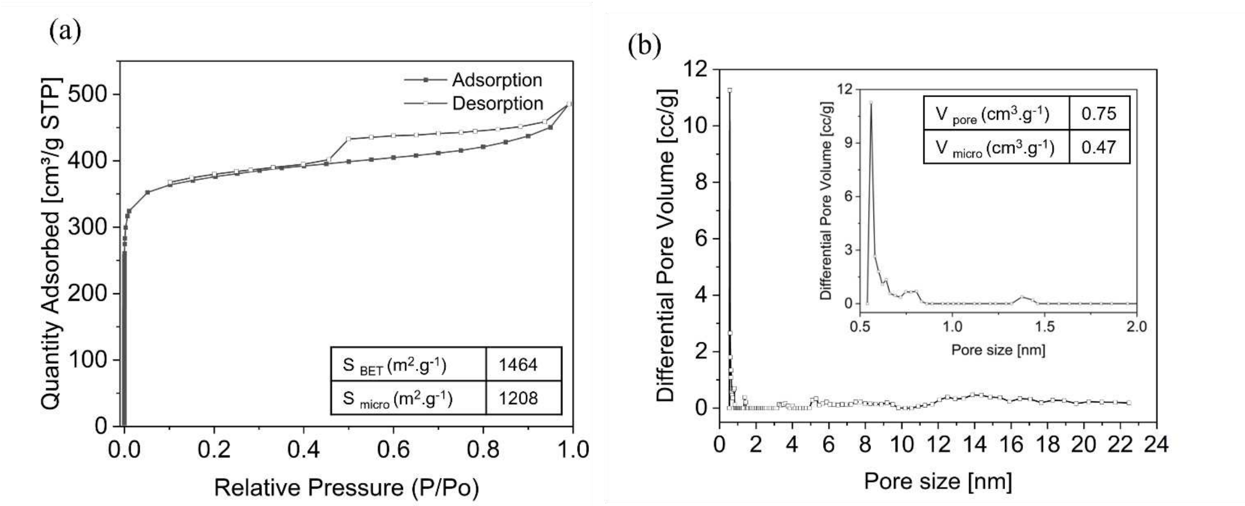

Figure 4-1 N_2 adsorption-desorption isotherm of GR-AC (a) and its corresponding pore size distribution (b). The insets in figures show surface areas and pore volumes.

The SSA performance of the garlic roots-derived activated carbon (GR-AC) electrodes was investigated by coupling the galvanostatic charging and discharging (GCD) cycles with CO_2 concentration measurements. The experimental setup used for SSA experiments is discussed in the supporting information (section S4 and Figure S2). The GCD curves and CO_2 concentration measurements in Figure 4-2 show that for all voltage windows, charging the supercapacitor leads to adsorption of CO_2 while discharging the supercapacitor leads to desorption of CO_2. A concentration decrease from 15 % to 5 % is observed during charging from 0 V to -1 V (Figure 4-2a). After reaching the minimum concentration, the CO_2 concentration returns close to the equilibrium value during the potential holding step at -1 V. A holding time of 120 min was needed to achieve the full saturation and maximum adsorption capacity of the electrodes (Figure S3). Similarly, an increase in concentration from 15 % to 31 % is observed during discharging the supercapacitor from -1 V to 0 V followed by a voltage holding step at 0 V to allow complete desorption of CO_2. At increased voltage windows, the minimum CO_2 concentration reaches 4.8 %, 3.8%, and 3.3 % at -1.2 V, -1.4 V, and -1.6 V while the maximum concentration increased to 36 %, 40 %, and 41 %, respectively upon discharging to 0 V from respective voltages (Figure 4-2b-d).

The desorption curves show a sharp transition after reaching the maximum concentration at all voltage windows and attain the equilibrium concentration of ca. 15% during the 60 minutes of holding time. However, the adsorption curves are broader and return only slowly to the original CO_2 concentration, suggesting that adsorption is slower than desorption. This effect is more pronounced at higher voltage windows of -1.2 V, -1.4 V, and -1.6 V, and the maximum adsorption capacity is not reached after the 90 minutes holding time. These results can be understood through the ionic liquid-solid mechanism of SSA which assumes that CO_2 hydrolyses in the electrolyte to form H^+, HCO_3^-, and CO_3^{2-} ions that can adsorb to the double layers of the positive electrode (as HCO_3^-, CO_3^{2-}) and the negative electrode (as H^+) upon charging. The H^+ ions have smaller size, higher charge-density, and higher mobility compared to Na^+ ions and their preferential adsorption to the double layer increases the pH of the bulk solution. The increase in pH upon charging shifts the $CO_{2(aq)}/HCO_3^-$ equilibrium towards HCO_3^-, leading to depletion of CO_2 from the solution, which leads to additional CO_2 dissolution from the gas phase to the solution, until the chemical equilibrium is re-established. Application of higher voltage windows results in higher charge storage in the electrodes explaining the increased amount of CO_2 captured. Upon discharging, the desorption of respective ions from the solution shifts the chemical equilibria, leading to increased concentration of CO_2 in the effluent stream. The proposed ionic liquid-solid mechanism is a working hypothesis backed by previous studies.[58,62,95] The rate constant for CO_2 hydrolysis is known to be smaller than for the reverse reaction, explaining the faster desorption.[4,142] The effect is possibly more pronounced at higher voltage windows because first more easily accessible larger pores are utilized, and less accessible, smaller pores are only used closer to the final voltage. In addition to the ionic liquid-solid mechanism, the gas-solid mechanism (adsorption of CO_2 in the micropores that are not infiltrated by the electrolyte) and the molecular liquid-solid mechanism (adsorption of CO_2 in the electric double layer due to solubility difference between the double layer and the bulk solution) have also been proposed for SSA.[62,63] The quantitative determination of the exact mechanism require in-situ spectroscopic technique and modified experimental setup to track the formation of $CO_2/HCO_3^-/CO_3^{2-}$ during discharging/charging and is a subject of future study.

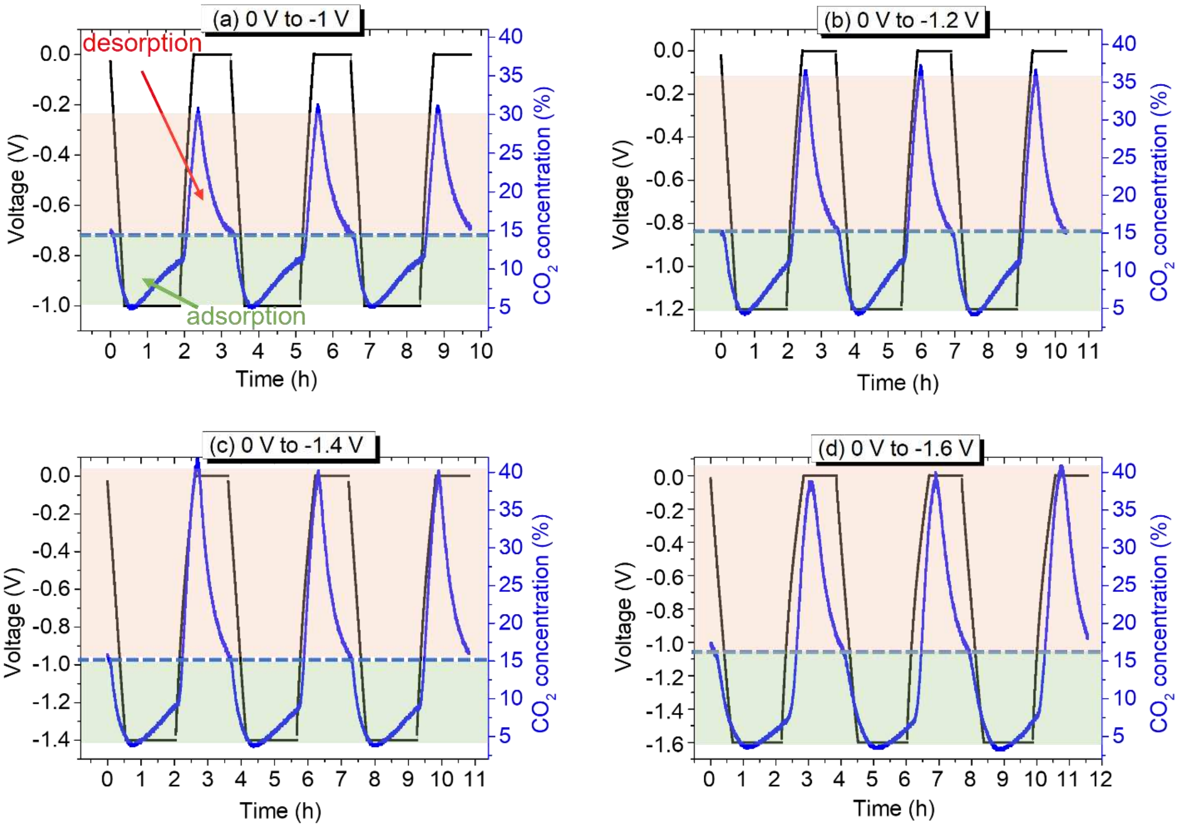

Figure 4-2 Voltage response (black) and CO_2 concentration profiles (blue) versus time at different potential windows (a-d). The green and red shaded areas above and below the equilibrium concentration of 15 % CO_2 indicate adsorption (CO_2 capture) and desorption (CO_2 release) during charging and discharging cycles. Gas flow rate of 1 sccm was used for these experiments. The gas mixture contains 15% CO_2 and 85% N_2.

Figure 4-3 shows a quantitative comparison of the SSA energetic and adsorptive performance at different potential windows. These metrics are calculated from the voltage and CO_2 concentration profiles in Figure 4-2. Formulas and tabulated results are provided in section S5 and Table S1 in the supporting information, respectively. The gravimetric capacitance increases from 173 $F.g^{-1}$ at -1 V to 181 $F.g^{-1}$, 183 $F.g^{-1}$, and 196 $F.g^{-1}$ at -1.2 V, -1.4 V, and -1.6 V, respectively (Figure 3a). The increase in capacitance is due to increased pore utilization and/or enhanced pseudocapacitive contribution from hydrogen sorption at higher potentials.[143] The SSA gravimetric adsorption capacity (AC) achieves a record high value of 312 $mmol.kg^{-1}$ at -1 V compared to all the previous reports. It further increases to 384 $mmol.kg^{-1}$, 461 $mmol.kg^{-1}$, and 485 $mmol.kg^{-1}$ at -1.2 V, -1.4 V, and -1.6 V, respectively (Figure 4-3a). The adsorption capacity values almost linearly increase with increasing potential window until -1.4 V after which the slope decreases, which is consistent with more incomplete adsorption at higher potential window (Figure 2d). The volumetric capacitance and volumetric adsorption capacity also follow the same pattern (Figure 4-3b) as the gravimetric capacitance and gravimetric adsorption capacity (85.7 $mol.m^{-3}$ at -1 V, 105 $mol.m^{-3}$ at -1.2 V, 126 $mol.m^{-3}$ at -1.4 V, and 133 $mol.m^{-3}$ at -1.6 V, respectively).

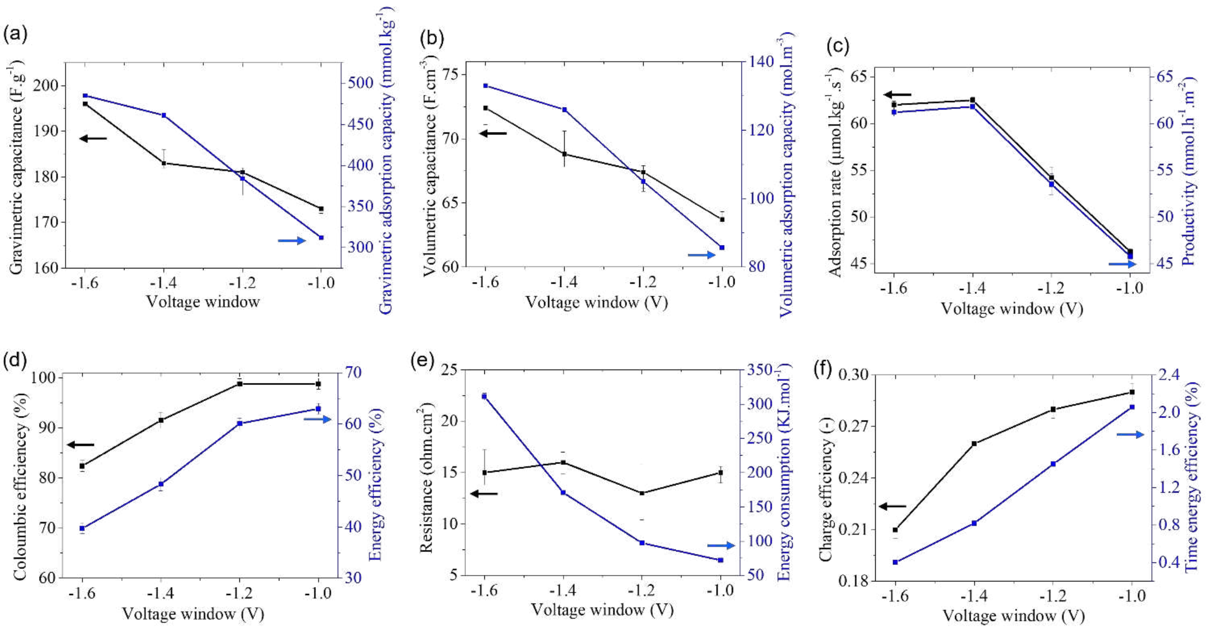

Figure 4-3 Relationships between SSA energetic and adsorptive metrics at different voltage windows for GR-AC electrodes. (a) Gravimetric capacitance and gravimetric adsorption capacity, (b) volumetric capacitance and volumetric adsorption capacity, (c) adsorption rate and productivity, (d) coulombic efficiency and energy efficiency, (e) resistance and energy consumption, (f) charge efficiency and time energy efficiency.

The relationship between the total charge stored in the supercapacitors at different voltage windows and the gravimetric/volumetric sorption capacities also follows a linear pattern until -1.4 V (Figure S4). Above -1.5 V there is a possibility of carbon electro-oxidation along with increased leakage currents and decreased coulombic efficiency,[144] which may reduce the adsorption capacity as well as adsorption rates. Their effect on SSA energetic performance at higher potential windows is discussed in the later section.

The SSA adsorption rate and productivity linearly increases from -1.0 V to -1.4 V after which they stay the same (Figure 4-3c). The 24 % increase in both the adsorption rate and productivity at -1.4 V indicates that a wider potential window leads to faster CO_2 hydrolysis, possibly due to faster depletion of H^+ ions in the bulk solution. Similar to volumetric adsorption capacity, the productivity also approximately doubles compared to previous best results, possibly due to the combined effect of using higher voltage window and improved mass transfer of GR-AC electrodes. The coulombic efficiency (η_c) stays around 99 % at -1 V and -1.2 V, reduces to 91 % at -1.4 V, and further reduces to 82 % at -1.6 V (Figure 3d). Reduced η_c at -1.6 V may be attributed to enhanced irreversible, pseudocapacitive contributions from surface functionalities and hydrogen sorption.[145,146] By continuously running the SSA cycles at -1.4 V for multiple cycles, a coulombic efficiency of ~97 % was achieved without any performance loss in SSA adsorption capacity (Figure S5), arguing that after a few cycles the most irreversibly redox-active functionalities from the activated carbon surface are removed, and the electrodes can be fully reversibly charged. After 130 h of continuous cycling at -.1.4 V, the electrodes were again charged for additional 90 h at -1.4 V, and the voltage curves, current profiles, and CO_2 concentration changes show reproducible results (Figure S6). Previous studies have shown that increasing the voltage window of aqueous supercapacitors above 1.5-1.6 V results in carbon oxidation at the anode and hydrogen evolution at the cathode, irreversible charge losses, and high leakage currents that significantly degrades the supercapacitors long-term performance.[144–146] Therefore, the optimal voltage window for SSA with GR-AC electrodes in the $NaHCO_3$ electrolyte used in the current study would be -1.4 V. The energy efficiency (η_e) stays above 60 % up to -1.2 V, reduces to 50 % at -1.4 V, and further reduces to 40 % at -1.6 V (Figure 4-3d). Since additional energy is required to store additional charges in the pores at higher voltage, an increased energy loss is observed at higher voltages (Table S1). Previous SSA studies have shown that η_e

as high as 80 % can be achieved by using very concentrated electrolytes (e.g. 5 M NaCl),[100] or alternative salt solutions (e.g., 1 M $MgBr_2$)[63], arguing that there is a room for further improvement in η_e values.

The relationship between voltage window, resistance, and energy consumption is shown in Figure 4-3e. The resistance values vary between 10 $\Omega.cm^2$ to 16 $\Omega.cm^2$ within the standard deviation from -1 V to -1.6 V, suggesting that thicker GR-AC electrodes (1 mm) with high mass-loadings (38 mg/cm^2) can still show good charge transport behavior. These resistance values are lesser than all the previously reported biomass-derived electrodes used for SSA.[137] This signifies that the modified synthesis and electrode preparation procedure for garlic-roots derived activated carbon electrodes is critical to achieve better electronic conductivity. A record low energy consumption of ~70 $kJ.mol^{-1}$ is observed at -1 V voltage window (Figure 4-3e). The energy consumption increases to 97 $kJ.mol^{-1}$ at -1.2 V, 166 $kJ.mol^{-1}$ at -1.4 V, and 311 $kJ.mol^{-1}$ at -1.6 V, respectively. Since energy consumption is the ratio of energy loss to the moles of CO_2 adsorbed, the increased energy loss at high voltage windows results in increased energy consumption values. Minimizing the voltage holding times and increasing the SSA adsorption rates can improve the energy consumption values. To verify this statement, we performed additional experiments at a higher gas flow rate of 5 sccm compared to 1 sccm used in the previous experiments. The results showed that the SSA energy consumption can be reduced to 130 $kJmol^{-1}$ at -1.4 V and 191 $kJmol^{-1}$ at -1.6 V, respectively (Table S2). The experiments further showed that the full CO_2 adsorption capacity of GR-AC electrodes is 524 $mmol.kg^{-1}$ at -1.4 V and 578 $mmol.kg^{-1}$ at -1.6 V. The adsorption kinetics also increases at higher flow rates, but the gas purity decreases (Figure S7). Additional SSA experiments at voltage window of -2.0 V (Figure S7c) showed large deviation from the capacitive-type behavior, poor coulombic/energy efficiency, and very large energy consumption, arguing that the working voltage window of SSA must be within the recommended operating voltage window of carbon-based aqueous supercapacitors (< 1.6 V).[144,147] A comparison of SSA adsorption and desorption capacities after ageing the electrodes for six days showed significantly higher CO_2 desorption capacity (807 $mmol.kg^{-1}$) at -2 V compared to the adsorption capacity (641 $mmol.kg^{-1}$), while the adsorption and desorption capacity at -1.6 V stayed almost the same (~570 $mmol.kg^{-1}$) (Figure S7). This indicates that at very high voltage the carbon in the electrodes is partially oxidized to form CO_2, further confirming the detrimental effects of electrodes charging above the 1.6 V limit. The charge efficiency (CE) of GR-AC electrodes is around 0.3 up to -1.2 V which is higher than all the previously reported values.[137] The CE slightly reduces to 0.26 at -1.4 V, and further reduces to 0.21 at -1.6 V (Figure 4-3f). The improved charge efficiencies may be due to improved pore accessibility to H^+/HCO_3^- $/CO_3^{2-}$, leading to a more effective removal of these ions from the chemical equilibrium. Nevertheless, further improvement in CE without narrowing down the voltage window or using expensive ion-selective membranes is desirable, which may be achieved through further pore size engineering of activated carbons. Time energy efficiency (TEE) signifies the amount of CO_2 adsorbed per unit time per unit energy and is maximum at -1 V (Figure 3f). TEE decreases almost linearly from 2.0 $\mu mol.kJ^{-1}.s^{-1}$ at -1 V to 0.4

μmol.kJ^{-1}.s^{-1} at -1.6 V. Further minimization of cycle times and energy consumption at high voltage windows are desirable to increase the TEE values.

The energetic and adsorptive performance metrics obtained from GR-AC electrodes were compared with BPL 4 x 6 electrodes as reference with the aim to identify the influence of electrode hot-pressing on SSA performance. BPL carbon exhibits a lower BET surface area (1023 m^{2}g^{-1}), smaller micropore volume (0.27 cm^{3}g^{-1}), and narrower pore size distribution compared to GR-AC (Figure S8). The resistance of 1 mm thick BPL electrodes used in this study is higher (~32 Ω.cm^2) than the 0.7 mm thick electrodes used in previous studies (~12 Ω.cm^2), due to increased resistor length (Table S3 and Figure S9). However, the sorption capacity of thicker BPL electrodes prepared by hot-pressing improved to 90 mmol.kg^{-1} compared to previously reported values of ~60 mmol.kg^{-1} for thinner electrodes prepared by rolling technique,[63] signifying that the hot-pressing method for preparing high-mass-loading electrodes improves the adsorptive performance. A comparison of microporous BPL-AC with micro-mesoporous GR-AC shows that the sorption capacity of BPL-AC is still 3.5 times less than GR-AC at -1 V (89.8 mmol.kg^{-1} vs 312 mmol.kg^{-1}), three times less than GR-AC at -1.2 V (127 mmol.kg^{-1} vs 384 mmol.kg^{-1}), 2.7 times less than GR-AC at -1.4 V (173 mmol.kg^{-1} vs 461 mmol.kg^{-1}), and 2.4 times less than GR-AC at -1.6 V (200 mmol.kg^{-1} vs 485 mmol.kg^{-1} (Table S3). The decreasing difference in adsorption capacities at higher voltages indicate that BPL-AC initially had less many accessible pores compared to GR-AC at -1 V, but the pore utilization ratio of BPL-AC improves as the voltage window increases because more energy is available to force adsorption in smaller micropores. The increase in capacitance values of BPL-AC versus GR-AC from -1.0 V to -1.4 V also supports this statement (13.8 % increase for BPL versus 5.8 % increase for GR). Similarly, the adsorption rate of BPL-AC is around 2 times less than GR-AC at -1 V, and 1.6 times less at -1.6 V (Figure 4-3c and Table S3). The energy consumption of BPL is very high compared to GR-AC, i.e., 210 kJ.mol^{-1} at -1V, 244 kJ.mol^{-1} at -1.2 V, 318 kJ.mol^{-1} at -1.4 V, and 555 kJ.mol^{-1} at -1.6 V, respectively. Similar to GR-AC, the long-term cyclic performance of BPL for 130 h at -1.4 V voltage window showed reproducible adsorption-desorption curves without any performance loss (Figure S10). The above results prove that the new GR-AC electrodes with micro-mesoporous structure show greatly enhanced SSA performance compared to coal-derived microporous BPL-AC, both on energetic as well as adsorptive basis, and that high-mass loading electrodes prepared by hot pressing method are highly desirable for SSA.

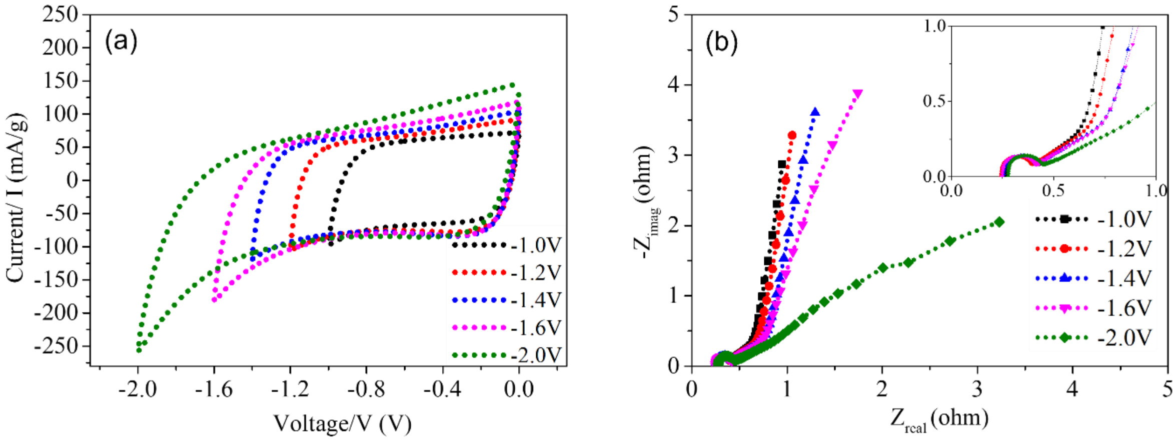

Figure 4-4 Cyclic voltammograms (1 mV.s-1) of GR-AC supercapacitor at different voltage windows (a), Nyquist plots of GR-AC supercapacitor at different DC voltages under frequency range of 105 Hz to 5 mHz (b). Both graphs show deviation from the ideal capacitive

The capacitive behavior of GR-AC electrodes exposed to CO_2 at different voltage windows was further evaluated using cyclic voltammetry (CV) and electrochemical impedance spectroscopy (EIS). The CV curves are rectangular-shaped up to -1.4 V and exhibit typical double-layer charge storage behavior (Figure 4-4a). At -1.6 V, the CV curve deviates from the ideal double layer behavior due to an increase in current after the charging curve exceeds -1.4 V. This suggests that some side reactions start to occur above -1.4 V, and is consistent with our GCD results, which showed slight deviation from the capacitive behavior and larger energy and charge loss at -1.6 V compared to -1.0 V, -1.2 V, and -1.4 V, respectively. The CV at -2.0 V further intensifies the faradaic currents possibly due to undesirable water decomposition and gas evolution reactions.[145] The Nyquist plots from EIS spectra also show capacitive type behavior up to -1.4 V, as seen from their quasi-vertical lines at low frequency (Figure 4-4b). The Nyquist plot at -1.6 V shows slight deviation from a quasi-vertical line and the plot at -2 V show a completely redox-type behavior, arguing that the optimal voltage window of GR-AC supercapacitor is -1.4 V for SSA operation.

In summary, we report a simple synthesis and preparation procedure to develop high mass-loading garlic-roots derived activated carbon electrodes with micro- and meso-pores for high voltage supercapacitive swing adsorption of carbon dioxide. The minimum energy consumption of 70 $kJ.mol^{-1}$ is achieved at an adsorption capacity of 312 $mmol.kg^{-1}$. The adsorptive performance of SSA can be increased to 524 $mmol.kg^{-1}$ at an energy consumption of 130 $kJ.mol^{-1}$ by increasing the potential window to -1.4 V. The electrodes show capacitive behavior up to -1.4 V with stable SSA performance over multiple cycles. These results show that new electrodes development is a potential route to further increase the adsorption capacity, lower the energy consumption, and improve the sorption kinetics of SSA.

4.3 Supporting information

S1. Experimental Section

S1.1 Materials

Garlic roots (KV farms, Stroudsburg, PA, USA) and coal-derived BPL 4 x 6 carbon (Calgon) were used as activated carbon sources. 60 % PTFE dispersion (Sigma Aldrich), conductive carbon black (VXCMAX22, Cabot Corporation), gluten (Hodgson Mill), ethanol (190 proof, Decon Labs), and DI water (18 MΩ) were used as binder, conductive agent, hydrophilic co-binder, and solvent, respectively. 1 M $NaHCO_3$ was used as an electrolyte and filter paper (Whatman Grade 2, GE Healthcare Life Sciences) was used as a separator.

S1.2 Synthesis of garlic roots-derived activated carbon

As-received garlic roots were washed several times with DI water and soaked in isopropyl alcohol overnight. The resulting sample was washed again with DI water, dried in the oven at 100^{o} C for 24 h, and pulverized to achieve a particle size of ≤ 350 µm. 30 g of powdered garlic roots sample was uniformly mixed with 120 g of K_2CO_3 and transferred to a custom-made Ni boat. The sample was then transferred to a tube furnace and heated to 600^{o}C at 6^{o}C/min ramp rate. The temperature was maintained at 600^{o}C for 1 h, then increased to 800^{o}C at 6^{o}C/min ramp rate, maintained at 800^{o}C for 1 h, and allowed to cool to room temperature naturally. Ar gas was used at a flowrate of 50 sccm to maintain the inert atmosphere inside the tube. The resulting activated carbon sample was washed several times with 1 M HCl and DI water until the pH reached 7.0. The sample was dried in the oven at 100^{o}C for 24 h. For air treatment, the activated carbon sample was placed inside the alumina boat, transferred to a tube furnace, heated to 420^{o}C at 6^{o}C/min ramp rate for 100 min. The final yield of the sample was around 15%. The resulting air oxidized garlic-roots-derived activated carbon was used to prepare the electrodes.

S1.3 Electrodes preparation and supercapacitor assembly

0.30 g of PTFE was added to 25 mL of ethanol. The solution was mixed and sonicated for 10 min to obtain a homogeneous mixture. 3.0 g of activated carbon, 0.37 g gluten, and 0.30 g conductive carbon black were added to the PTFE solution. The mixture was covered with Al foil and magnetically stirred at 60-65^o C for 2 h. The temperature was then increased to 80 ^{o}C for 30 min to evaporate the remaining solvent. The resulting slurry was transferred onto a glass plate, pressed, and mixed with metal spatulas for 10 min. The resulting dough was hot-pressed between two steel plates at 10,000 pounds and 50^{o}C to obtain about 1 mm thick electrodes. Two square electrodes with 36 cm^2 area were cut and placed in a vacuum oven at 100 ^{o}C and 25 mmHg for 12 h. The bottom electrode was soaked in 1 M $NaHCO_3$ solution for 2 hours. A 49 cm^2 filter paper was wetted with the electrolyte and used as a separator. A 36 cm^2 carbon cloth (AvCarb 1071 HCB) was used to cover the top electrode and served as a gas diffusion layer. The electrodes, separator, and gas diffusion layer were surrounded by an EPDM rubber gasket (9.5 cm × 9.5 cm outer area, 8 cm × 8 cm inside area, 0.29 cm thickness, Fuel cell store) and sandwiched between titanium grade 7 plates (13 cm × 13 cm, 0.95 cm thick), which served as current collectors. The resulting assembly was pressed together by evenly tightening 16 set screws connecting the Ti plates using a torque wrench to 20 in.lb of force. Figure S2 (part 5) shows the supercapacitor assembly.

S2. Surface area and pore size analysis

The N_2 adsorption and desorption isotherms were measured at 77 K using Micromeritics ASAP 2020 equipment. The sample was degassed under 200 °C for 24 h before the analysis. Low N_2 dosing mode was carried out before the relative pressure P/P_0 = 0.000105 in the adsorption branch. Total surface areas were calculated from the adsorption data at P/P_0 0.001~0.051 using the Brunauer-Emmett-Teller (BET) model. Total pore volumes were calculated from the adsorption data at P/P_0=0.99. The area and volume information of the micropore and mesopore were calculated from the adsorption data using the t-plot method (Carbon Black STSA model). The pore size distribution curves were obtained from the adsorption data using the non-local density functional theory (NLDFT) method, specifically with the N2-Carbon Finite Pores, AS=6. Here, AS=6 means a 2D model of finite slit pores having a diameter-to-width aspect ratio of 6. Slit type geometry of pores was used for simulation.

S3. Electrochemical testing

The electrochemical testing was performed using a Gamry Potentiostat 3000 in a two-electrode configuration. Cyclic voltammetry (CV) tests were conducted at 1 mV/s scan rate in the potential range of 0 to -2 V. Electrochemical impedance spectroscopy (EIS) was performed at different DC voltages (-1.0 V, -1.2 V, -1.4 V, -1.6 V, -2.0 V) in the frequency range of 10^5 Hz to 10^{-3} Hz. Galvanostatic charging and discharging (GCD) was performed at a constant current density of 50 mA.g^{-1} to test the gas adsorption-desorption behavior.

S4. Supercapacitive swing adsorption (SSA) testing

A schematic illustration of the SSA experimental setup is shown in Figure S2. A 15 % CO_2/85 % N_2 gas mixture flows through a bubbler filled with 1 M $NaHCO_3$. The bubbler was used to moisten the gas mixture. The moistened gas passes through a mass flow controller adjusted to a flow rate of 1 sccm. The gas mixture enters the SSA module from the center inlet port (1 mm in diameter) and flows radially through the gas diffusion layer inside the module. The gas exits from the outlet port at the corner of the top Ti plate, passes through a drying tube, and is then analyzed by a CO_2 analyzer (Quantek Instruments, Model 906). The gas mixture was flown through the modules for 8 h without applying any bias to complete conventional CO_2 adsorption to the electrodes and conventional CO_2 absorption by the electrolyte. After that time, the concentration of the exiting gas attained a constant value of 15% showing that conventional ad/absorption was complete. The module was then charged at a rate of 50 mA/g to different voltage windows. The potential was held at the highest charging voltage for an additional time (90 minutes for GR-AC) to allow for maximum saturation of the electrode with CO_2. After that, the module was discharged to 0 V at 50 mA/g followed by a holding step (60 min) to complete the desorption of CO_2 gas from the electrode.

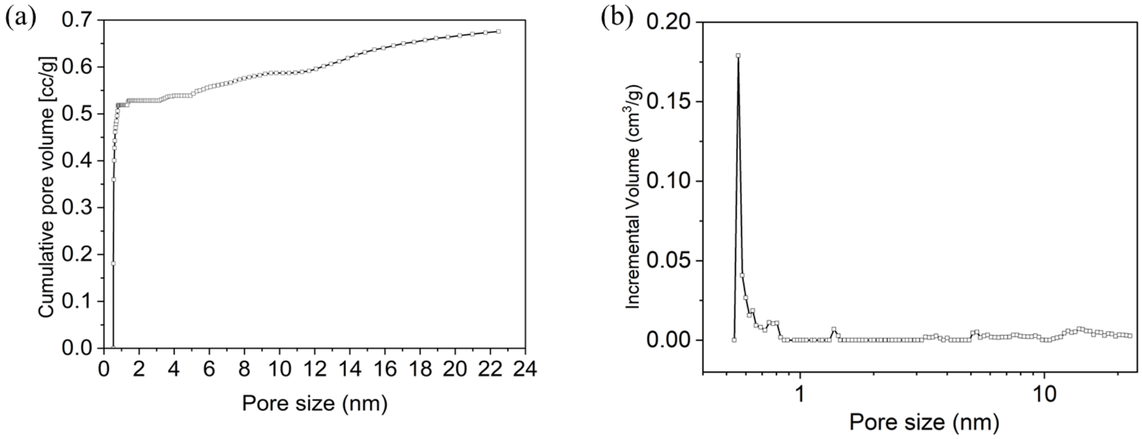

Figure S1 Pore size versus cumulative pore volume (a) and incremental pore volume (b) of GR-AC.

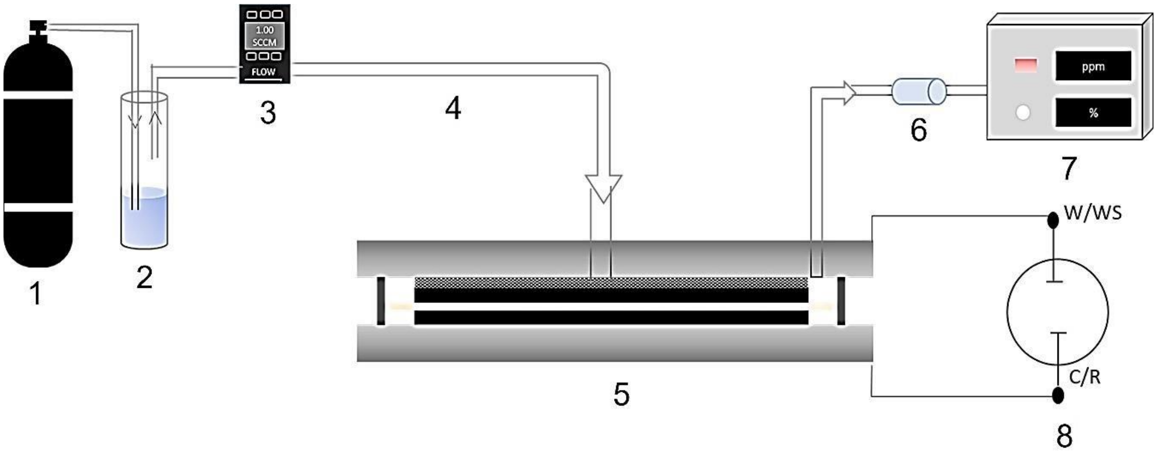

Figure S2 Schematic illustration of supercapacitive swing adsorption (SSA) apparatus in flow-through mode. 1: N_2/CO_2 gas cylinder, 2: Bubbler containing 1 M $NaHCO_3$, 3: Mass flow controller, 4: Cu tubing, 5: supercapacitor module, 6: Drying tube, 7: CO_2 analyzer, 8: Potentiostat.

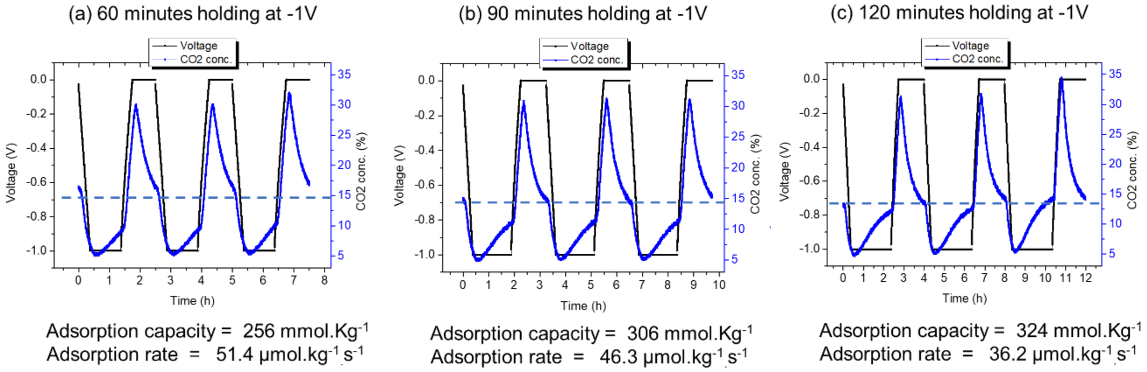

Adsorption capacity = 256 mmol.Kg^{-1}
Adsorption rate = 51.4 μmol.kg^{-1} s^{-1}

Adsorption capacity = 306 mmol.Kg^{-1}
Adsorption rate = 46.3 μmol.kg^{-1} s^{-1}

Adsorption capacity = 324 mmol.Kg^{-1}
Adsorption rate = 36.2 μmol.kg^{-1} s^{-1}

Figure S3 Voltage and CO_2 concentration profiles versus time at different holding times, (a) 60 min, (b) 90 min, (c) 120 min. Gas flow rate of 1 sccm was used. The adsorption capacity and adsorption rates shown in figures were calculated from equations shown in section S5.2.

Table S1 SSA energetic and adsorptive performance metrics of GR-AC electrodes at different potential windows.

Voltage windows		**-1.0 V**	**-1.2 V**	**-1.4 V**	**-1.6 V**
Energetic metrics					
ESR (Ω.cm^2)	at low V	14.9 ± 0.2	10.1 ± 1.0	15.7 ± 1.0	10.5 ± 1.3
	at high V	15.6 ± 0.3	10.4 ± 0.1	17.0 ± 0.9	13.8 ± 1.0
C_s (F.g^{-1})		173 ± 0.3	181 ± 1.2	183 ± 0.8	196 ± 1.7
C_V (F.cm^{-3})		63.7 ± 0.1	67.4 ± 0.4	67.0 ± 0.3	72.4 ± 0.6
t_g (s)		1340 ± 2.3	1685 ± 2.5	1965 ± 8.6	2430 ± 21.5
η_c (%)		98.8 ± 0.1	98.8 ± 0.3	91.4 ± 0.6	82.4 ± 0.1
η_e (%)		63.0 ± 0.03	60.1 ± 0.1	49.6 ± 0.3	39.7 ± 0.05
ΔE (J)		22.0 ± 0.06	37.0 ± 0.3	75.7 ± 0.8	149 ± 1.1
Adsorptive metrics					
n avg. (μmol)		306 ± 2.0	379 ± 7.5	455 ± 2.5	479 ± 4.5
AC (mmol.kg^{-1})		312 ± 2.0	384 ± 7.6	461 ± 2.5	485 ± 4.6
AC (mmol.m^{-2})		85.7 ± 0.6	105 ± 2.1	126 ± 0.7	133 ± 1.25
AC (mol.m^{-3})		85.7 ± 0.6	105 ± 2.1	126 ± 0.7	133 ± 1.25
AR (μmol.kg^{-1}.s^{-1})		46.3 ± 0.3	54.2 ± 1,1	62.5 ± 0.3	62.0 ± 0.4
P (mmol.h^{-1}.m^{-2})		45.8 ± 0.3	53.5 ± 1.1	61.8 ± 0.3	61.2 ± 0.4
CE (_)		0.29 ± 0.00	0.28 ± 0.00	0.26 ± 0.00	0.21 ± 0.00
EC (KJ.mol^{-1})		72.1 ± 0.7	97.2 ± 1.8	166 ± 0.8	311 ± 0.6

TEE (µmol.KJ^{-1}.s^{-1})	2.06 ± 0.02	1.45 ± 0.02	0.82 ± 0.00	0.4 ± 0.00

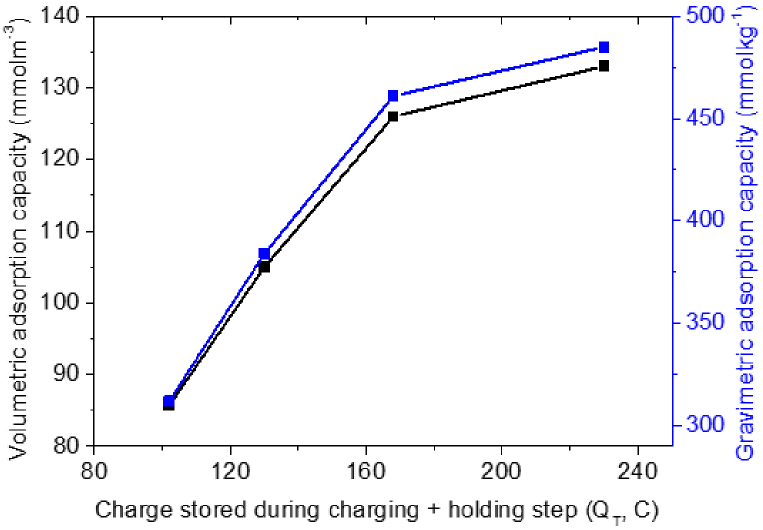

Figure S4 Gravimetric and volumetric adsorption capacities versus total charge stored in the supercapacitor during charging plus holding step.

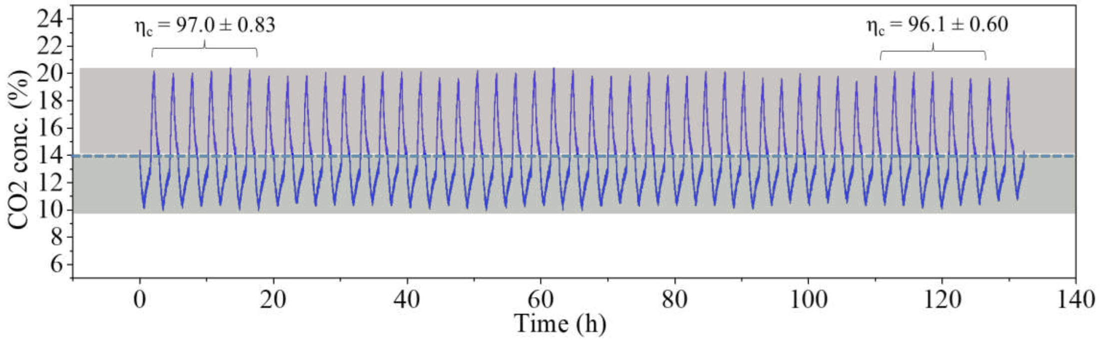

Figure S5 SSA performance of GR-AC electrodes at -1.4 V and 5 sccm flowrate showing stable performance.

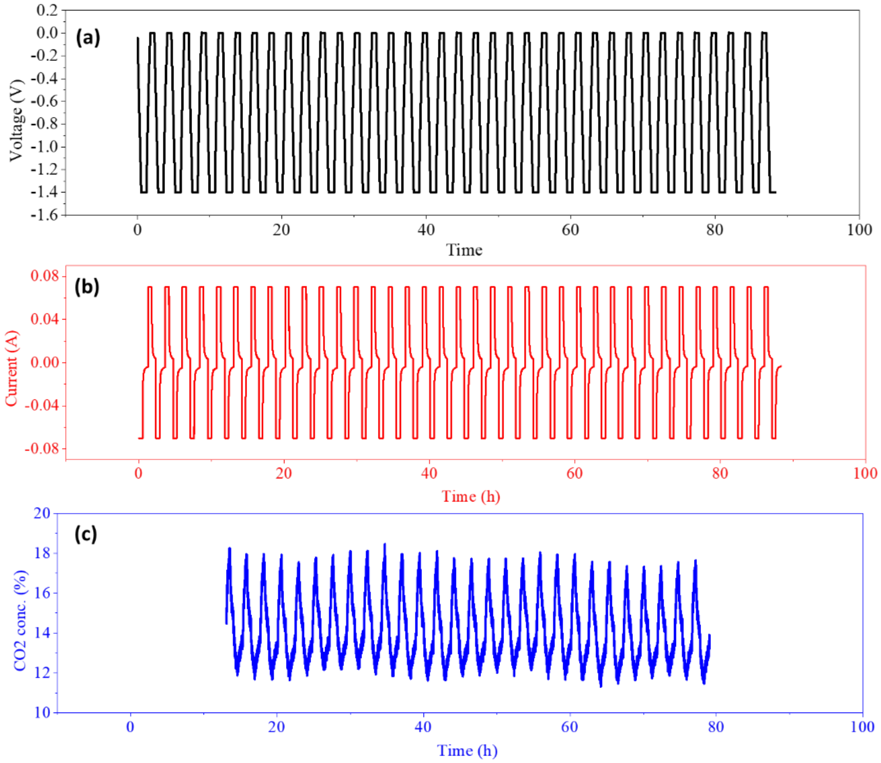

Figure S6 Voltage curves (a), current profiles (b), and CO_2 concentration changes (c) during SSA tests at -1.4 V and 8 scum flowrate. These tests were performed after the SSA tests shown in Figure 5.

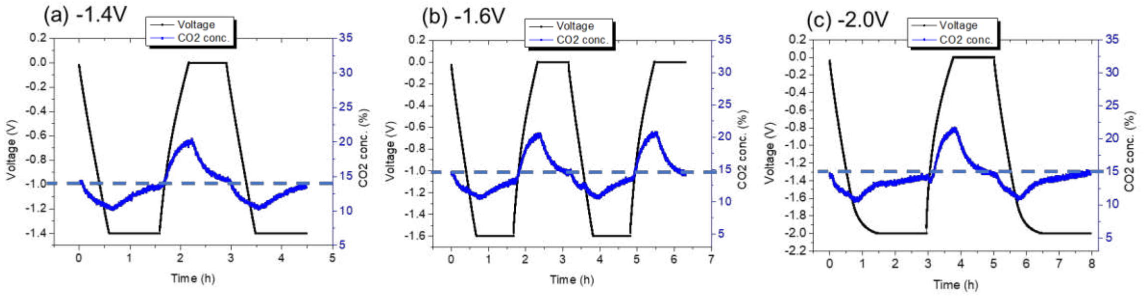

Figure S7 Voltage and CO_2 concentration profiles versus time at higher flowrate of 5 sccm, (a) -1.4 V, (b) -1.6V, (c) -2.0V. The tests were conducted using the same supercapacitor 5 days after the tests conducted at 1 sccm flowrate.

Table S2 Energetic and adsorptive performance metrics of SSA at higher voltage window and 5 sccm flowrate.

Voltage window		**-1.4 V**	**-1.6 V**	**-2.0 V**
Energetic metrics @ 50 m.Ag^{-1}				
ESR (Ω.cm^{2})	at 0 V	12.8	15.8	23.0
	at –high V	14.9	17.2	39.3
C_s (F.g^{-1})		186	190	337
C_V (F.cm^{-3})		68.8	71.1	125
t_g (s)		2120	2360	5220
η_c (%)		93.6	86.0	39.7
η_e (%)		52.6	45.3	12.0
ΔE (J)		67.6	110	921
Adsorptive metrics @ 50 m.Ag^{-1}				
n avg. (μmol)		518	572	663

AC (mmol.kg^{-1})	524	578	671
AC (mmol.m^{-2})	144	159	184
AC (mol.m^{-3})	144	159	184
AR (µmol.kg^{-1} s^{-1})	91.6	97.1	76.0
P (mmol.h^{-1}.m^{-2})	90.5	95.9	71.8
CE (_)	0.3	0.26	0.10
EC (KJ.mol^{-1})	130	191	1430
TEE (µmol.KJ^{-1}.s^{-1})	1.34	0.88	0.07

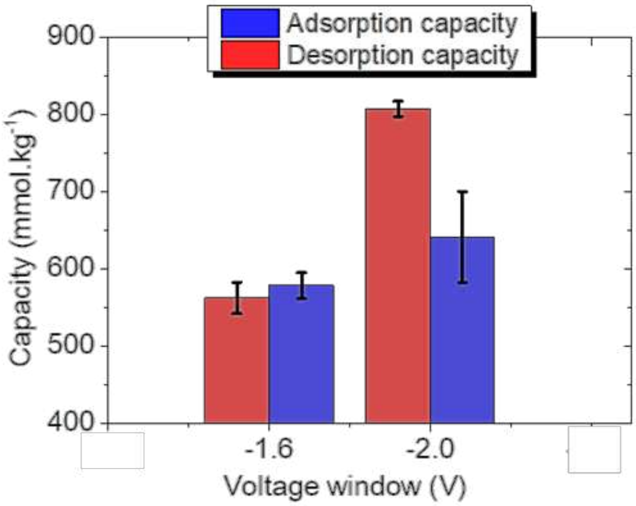

Figure S8 A comparison of SSA adsorption and desorption capacities at -1.6 V and -2.0 V six days after ageing the electrodes.

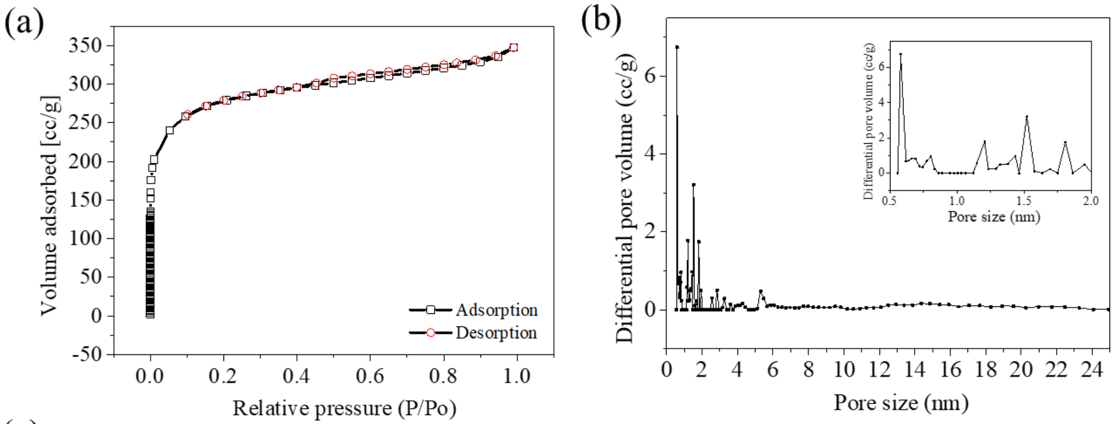

(c)

Samples	**S $_{BET}$ ($m^2.g^{-1}$)**	**S $_{micro}$ ($m^2.g^{-1}$)**	**V $_{pore}$ ($cm^3.g^{-1}$)**	**V $_{micro}$ ($cm^3.g^{-1}$)**
GR-AC	1464	1208	0.75	0.47
BPL-AC	1023	659.5	0.54	0.27

Results of BPL 4 x 6 electrodes

Figure S9 N_2 sorption isotherm of BPL-AC (a), pore size distribution of BPL-AC (b), and comparison of surface areas and pore volumes of GR-AC and BPL-AC.

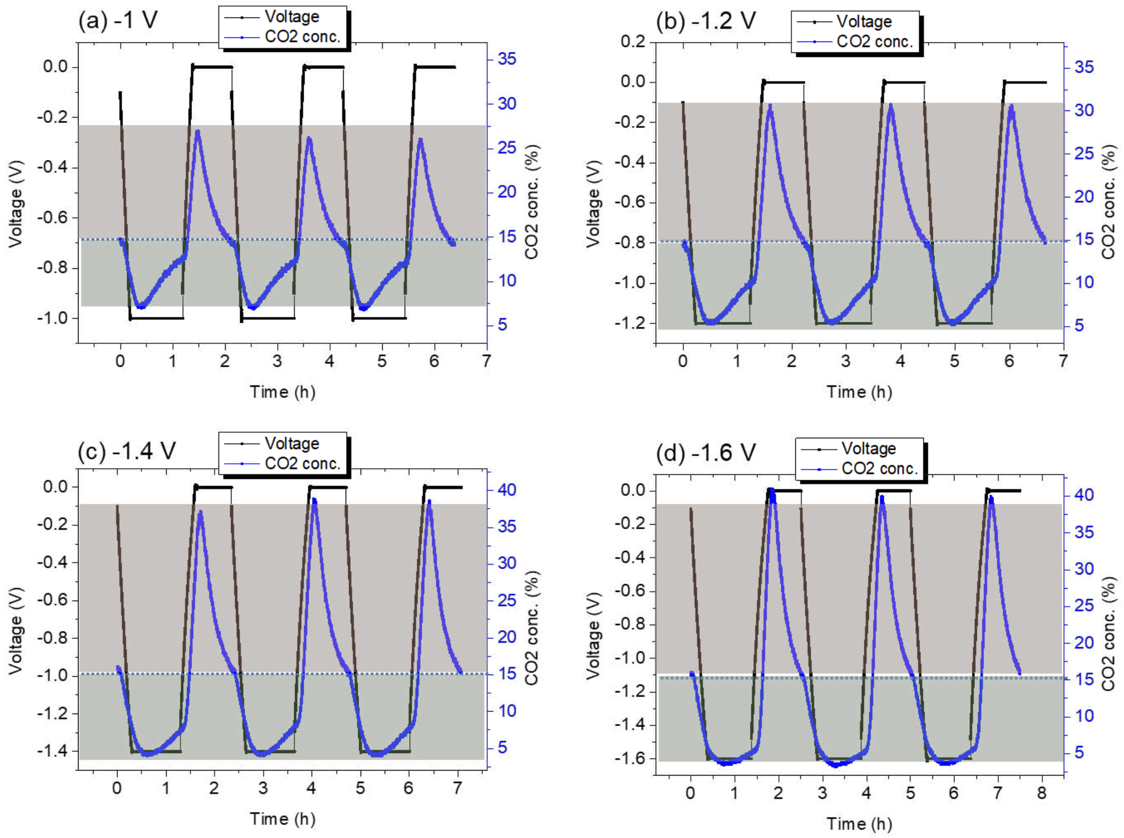

Figure S10 Voltage response (black) and CO_2 concentration profiles (blue) versus time at different potential windows (a-d) for BPL electrodes. The green and red shaded areas above and below the equilibrium concentration of 15 % CO_2 indicate adsorption and desorption during charging and discharging cycles. Gas flow rate of 1 sccm was used for these experiments.

Table S3 SSA energetic and adsorptive metrics for BPL electrodes at different voltage windows. The flowrate of 1 sccm was used for the experiments.

Voltage window		**-1.0 V**	**-1.2 V**	**-1.4 V**	**-1.6 V**
Energetic metrics					
ESR (Ω.cm^2)	at low V	32.3	32.6	32.9	34.0
	at high V	32.6	33.2	34.6	38.9
C_s (F.g^{-1})		81.0	83.8	92.2	101
C_V (F.cm^{-3})		48.6	50.3	55.3	60.9
t_g (s)		672	834	1069	1347
η_c (%)		97.9	95.9	92.0	75.7
η_e (%)		48.0	46.0	44.4	31.8
ΔE (J)		30.1	49.4	87.6	178
Adsorptive metrics					
n avg. (μmol)		144	203	276	320
AC (mmol.kg^{-1})		89.8	127	173	200
AC (mmol.m^{-2})		39.9	56.3	76.7	88.8
AC (mol.m^{-3})		39.9	56.3	76.7	88.8
AR (μmol.kg^{-1}.s^{-1})		21.0	28.6	37.0	40.4
P (mmol.h^{-1}.m^{-2})		33.6	45.7	59.1	64.6
CE (_)		0.16	0.17	0.17	0.14
EC (KJ.mol^{-1})		210	244	318	555
TEE (μmol.KJ^{-1}.s^{-1})		1.12	0.93	0.67	0.36

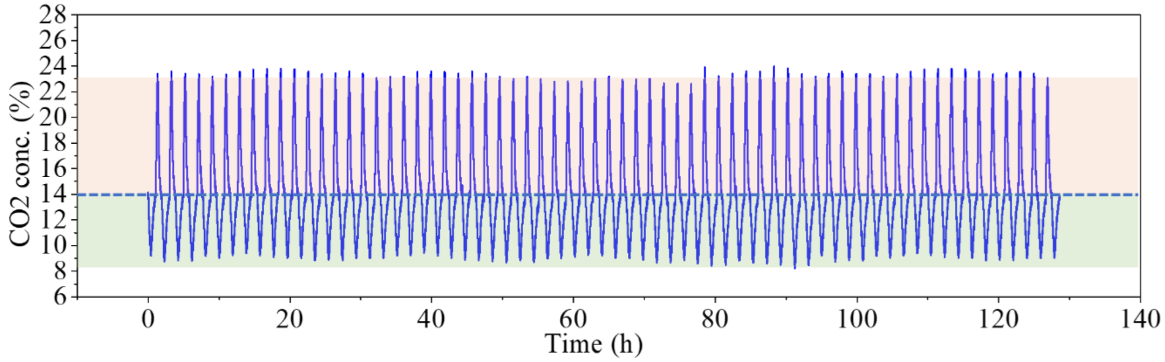

Figure S11 SSA performance of BPL electrodes at -1.4 V at 5 sccm flowrate for 130 hours showing reproducible adsorption-desorption capacity.

CHAPTER 5: INFLUENCE OF OXYGEN ON SUPERCAPACITIVE SWING ADSORPTION OF CO_2

This chapter has been published as: Oxygen-assisted supercapacitive swing adsorption of carbon dioxide, ***chemrxiv***, 2024 10.26434/chemrxiv-2024-z6966

5.1 Introduction

Electrochemical methods for CO_2 capture and concentration have emerged as potentially safer, energy efficient, modular and scalable alternative to traditional thermochemical methods which tend to be energy-intensive, and frequently use toxic, and corrosive chemicals such as amines, and hydroxides. Unlike thermochemical methods, electrochemical methods can be done isothermally, which avoids the energy penalty associated with temperature changes.[11,21,31,32] Most electrochemical capture methods are based on redox reactions, that capture CO_2 either through electrochemical modulation of proton concentration (pH swing),[25,35] electrochemical generation of nucleophiles by reducing redox-active organic molecules,[23,29,36] or electrochemically mediated amine regeneration (EMAR).[24,37,38] The current challenges with redox-based techniques revolve around oxygen sensitivity, high materials cost, cycle stability, and energy losses due the overpotentials associated with the redox process.[33] The presence of oxygen significantly lowers the coulombic/energy efficiencies either by deactivating the redox active compound or by directly participating in redox reactions.

Supercapacitive techniques are attractive alternatives to redox-based techniques, and can be divided into membrane capacitive deionization (MCDI), and supercapacitive swing adsorption (SSA).[39,45] In contrast to redox-based techniques, the potential window is continuously variable, and the methods are based on inexpensive, non-toxic activated carbon materials and aqueous solutions. Moreover, supercapacitors are known for high round-trip energy efficiency, and cycle stability offering potential advantages pertaining energy consumption, and system lifetime. Compared to MCDI, SSA does not require membranes, and the gas mixture is fed directly through the SSA module, whereas in MCDI, the gas is first dissolved in water, and this solution is then fed through the MCDI module.

Since the first report on SSA by our group, significant technological progress has been made towards improving the cell design, increasing the CO_2 adsorption capacity, and demonstrating the scalability potential through bipolar electrode stacks.[60,148,149] Fundamental studies on SSA focused on the collection of energetics and adsorptive performance metrics as a function of charging protocols, electrolyte composition, and concentration.[61,63,100] Recent studies from us and other researchers highlighted the possibility of enhancing the CO_2 sorption capacity by tuning the voltage window, investigated critical factors contributing towards performance improvements, and proposed biomass- and non-biomass derived carbon-based materials with high surface areas and capacitances for enhancing SSA performance.[95,110,148,150] To date, a maximum sorption capacity of ~520 $mmol.kg^{-1}$ at an energy consumption of ~130 $kJ.mol^{-1}$ CO_2 is reported with 15% CO_2/85% N_2 gas mixtures.[110] Recently, Forse et el. reported the supercapacitive swing adsorption of pure O_2, and 20% CO_2/15% O_2/ 65% N_2 gas mixtures.[22] Partially reversible O_2 adsorption was measured in experiments with pure O_2 when the negative electrode was the gas-exposed electrode, but the amounts were not quantified. No significant O_2 adsorption was measured with the positive electrode as gas-exposed electrode. Ultra-low energy consumption as low as 0.3 kJ/mol were reported with the positive electrode as gas-exposed electrode, and the adsorption rates were as high as 300 $\mathrm{mmol.kg^{1}.h^{-1}}$ ($83\mu\mathrm{mol.kg^{-1}.s^{-1}}$) for the gas mixture. However, the investigations were performed in closed adsorption cells using pressure changes, and did not allow for actual gas separation. No data was provided for the adsorptive and energetic performance of the $CO_2/N_2/O_2$ mixtures with the negative electrode as gas-exposed electrode.[22]

Here, we report that oxygen assists the supercapacitive swing adsorption of carbon dioxide when the negative electrode is the gas-exposed electrode, leading to adsorption capacities that are up to 11 times enhanced. All experiments were performed in batch-mode under continuous gas flow allowing for actual gas separation. In our study, we used gas mixtures containing 15% CO_2 and 5-20% O_2 balanced with N_2. Coal-derived BPL 4x6 carbon (Calgon) and garlic roots-derived micro-mesoporous carbon were used as electrode materials, and two different aqueous solutions (3M $MgBr_2$, 3M $MgCl_2$) as deliquescent electrolytes. Deliquescent electrolytes avoid water evaporation under continuous gas flow at relative humidity ranges typical for air (20-100%) and flue gases (close to 100%). We further present strategies for improving energy efficiency in the presence of oxygen. Scheme 1 shows the experimental setup, and the individual components of the SSA cell. details are presented in the experimental section. of the paper

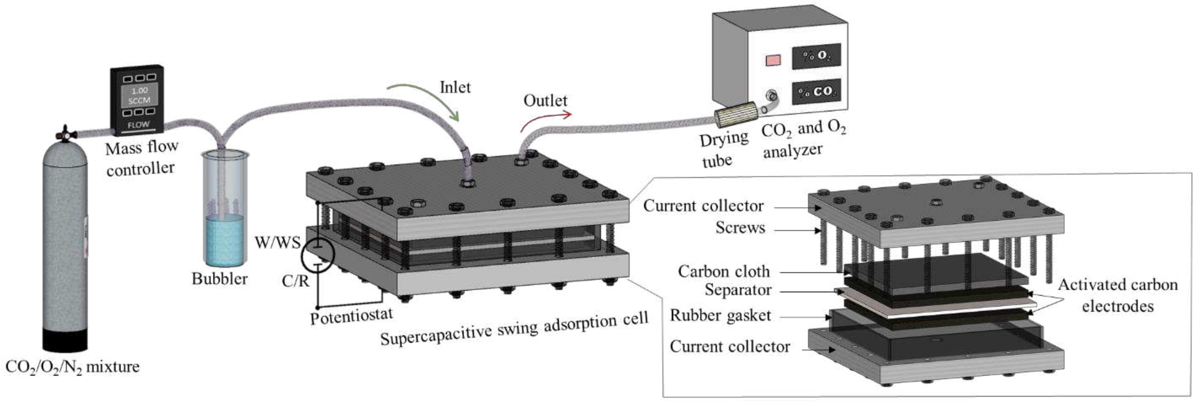

Scheme 1 controller, then passes through a bubbler filled with electrolyte which moistens the gas and enters the SSA cell through the center inlet port. The gas flows radially through the SSA cell, exits from the side outlet port, passes through a drying tube, and enters the CO2/O2 detector. The images are not according to the scale. W/WS and C/R stands for working, working sense, counter, and reference electrode.

5.2 Results and Discussion

Figure 5-1 shows the voltage changes and CO_2 concentration profiles during charging and discharging of an SSA module with 3M $MgBr_2$ as the electrolyte and 4x6 BPL carbon as electrode material. When a 15% CO_2/85% N_2 gas mixture is flown through the SSA module, the CO_2 concentration decreases during charging from 0V to -1V and goes back to the equilibrium concentration during the 20 min voltage holding step at -1V (Figure 5-1a). The CO_2 concentration increases upon discharging the module from -1V to 0V and reaches the equilibrium concentration during the 20 min voltage holding step at 0V. The voltage curves are linear, and the adsorption/desorption is reversible. As the gas mixture is replaced with 15% CO_2/5% O_2/80% N_2, a large deviation from the linear behavior of voltage change is observed, and charging/discharging cycles and CO_2 concentration changes are no longer reversible (Figure 5-1b). A much larger change in CO_2 concentration is observed. The non-linear behavior of the voltage curves beyond -0.8 V and below -0.2 V is attributed to the onset of irreversible faradaic reactions due to the presence of oxygen. To avoid these faradaic reactions and improve the reversibility of CO_2 adsorption and desorption during SSA experiments with oxygen, the voltage window was reduced from 1V to 0.6V (between -0.2 to -0.8V). Lowering the voltage window led to linear charge-discharge curves indicating capacitive behavior, and reversible CO_2 adsorption and desorption, respectively (Figure 5-1c). However, the CO_2 concentration curves did not fully return to the original value (15%) despite the much longer voltage holding times of 90 min, indicating that the equilibrium sorption capacity has not been reached yet. Further lowering of the voltage window from 0.6 to 0.4 V led to CO_2 concentration curves that achieved their equilibrium adsorption capacity during the first 20 minutes of voltage holding step (Figure 5-1d), similar to the CO_2/N_2 gas mixture without oxygen.

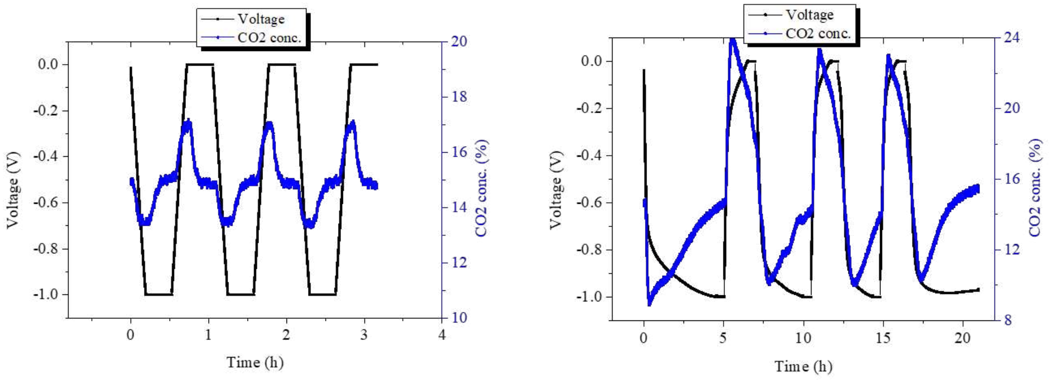

(a) 15% CO_2/85% N_2 (0 to -1V)

(b) 15% CO_2/5% O_2/80% N_2 (0 to -1V)

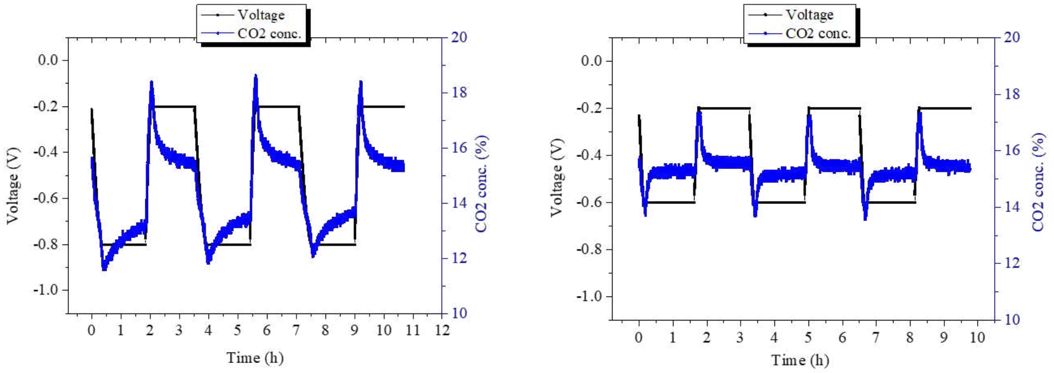

(c) 15% CO_2/5% O_2/80% N_2 (-0.2 to -0.8V)

(d) 15% CO_2/5% O_2/80% N_2 (-0.2 to -0.6V)

Figure 5-1 Voltage curves and CO2 concentration profiles during SSA tests with 15% CO2/85% N2 gas mixture at 1V (a), with 15% CO2/5% O2/80% N2 gas mixture at 1V (b), 0.6V (c), 0.4V (d). 3M MgBr2 is used as the electrolyte.

The energetic and adsorptive performance of SSA with 15% CO_2/5% O_2/80% N_2 gas mixture at 1 V, 0.6 V, and 0.4 V was compared with 15% CO_2/85% N_2 gas mixture at 1V (Figure 5-2 and Table S1). In the absence of oxygen, a capacitance value of 90 $F.g^{-1}$ and resistance of 8 $\Omega.cm^2$ resulted in CO_2 adsorption capacity of ~65 $mmol.kg^{-1}$ at an adsorption rate of ~40 $\mu mol.kg^{-1}.s^{-1}$ (Figure 5-2a and 5-2b). High coulombic efficiency (~97%) and energy efficiency (~80%) was achieved during cyclic charging, voltage holding after charging, discharging, voltage holding after discharging sequence (Figure 2c). An energy loss of 4J and a sorption capacity of 65 $mmol.kg^{-1}$ resulted in an energy consumption value of ~80 kJ.mol^{-1} (Figure 2d). In the presence of 5% oxygen, a large deviation from capacitive to faradaic behavior of the electrodes at 1V resulted in high resistance, very large charge storage capacity, and low coulombic and energy efficiency values (Figure 5-1b and Table S1). Although a higher CO_2 adsorption capacity of 1590 mmol.kg^{-1} was calculated for the first 3 SSA cycles, the continuously declining and irreversible performance of the electrodes along with large energy loss and energy consumption values restricted the use of the 1V voltage window in the presence of oxygen. Lowering the voltage window to 0.6 V (from -0.2 to -0.8V) restored the capacitive behavior of the electrodes as seen in Figure 1c. Capacitance values of ~250 F.g^{-1} and resistance of ~9 Ω.cm^2 at 0.6 V resulted in CO_2 adsorption capacity of ~750 mmol.kg^{-1} and adsorption rate of 120 μmol.kg^{-1}.s^{-1} at an energy consumption of ~300 kJ.mol^{-1}. This is ~11 times higher than the adsorption capacity calculated without oxygen in the gas mixture. It should be noted that this amount is still not an equilibrium amount because the concentration curves did not return to 15% despite the much longer potential holding times, showing that CO_2 was still appreciably adsorbed at the end of the potential holding step. For this reason, the reversibility of the adsorption could not be accurately determined. The desorption begins at a CO_2 concentration <15% which creates uncertainties pertaining to the size of the desorption integral. Assuming integrals as shown in Figure S1b, the ratio of moles of CO_2 adsorbed to desorbed is between 1 (595 μmol CO_2 captured during the charging step and 593 μmol CO_2 released during the discharging step, Table S1) as the upper limit and 0.26 (158 μmol desorbed CO_2) as the lower limit. Sequentially charging and discharging of the electrodes within a voltage window of 0.6V resulted in reproducible CO_2 adsorption and desorption behavior which was not possible at 1V (Figure S1a). However, large energy loss (~190 J) and higher leakage currents resulted in poor coulombic efficiency (~33%) and energy efficiency (~8 %) values even at lower voltage window of 0.6V. Further lowering the voltage window to 0.4V (-0.2 to -0.6V) resulted in reduced capacitance (~90 $F.g^{-1}$), reduced adsorption capacity (~66 $mmol.kg^{-1}$) and adsorption rate (~38 $\mu mol.kg^{-1}.s^{-1}$), higher coulombic efficiency (~88%) and energy efficiency (~67%), and lower energy loss (~4.6 J) and energy consumption (85 $kJ.mol^{-1}$) values (Figure 5-2 a-d). The energetic and adsorptive performance of the electrodes with 5% oxygen at 0.4 V (-0.2 V to -0.6 V) is similar to the performance with CO_2/N_2 mixture without oxygen at 1V. Cycling the electrodes for over 100 charge-discharge cycles at 0.4V in the presence of 5% oxygen resulted in nearly constant coulombic and energy efficiency values, and showed reversible, reproducible CO_2 capture and concentration profiles, signifying oxygen stability (Figure 5-2e).

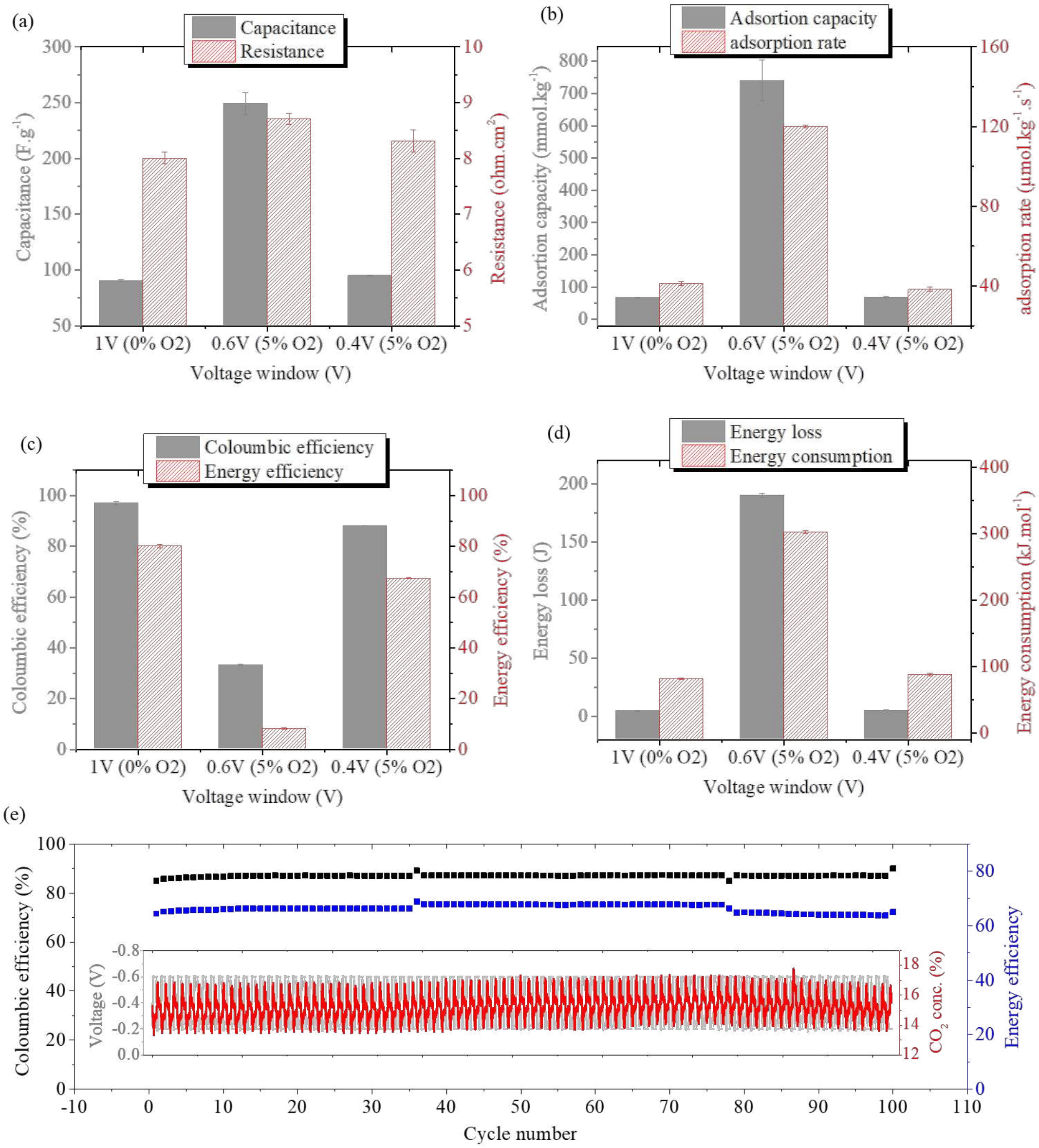

Figure 5-2 Energetics and adsorptive performance metrics of SSA with BPL electrodes and 3M MgBr2 electrolyte. (a) Capacitance and resistance, (b) CO_2 adsorption capacity and adsorption rate, (c) coulombic efficiency and energy efficiency, (d) energy loss and energy consumption without O_2 at 1V, with 5% O_2 at 0.6V and 0.4V, respectively. Long-term stability of SSA at 0.4V in the presence of 5% O_2 is achieved (e).

The influence of oxygen on the charge storage behavior during SSA tests was investigated by cyclic voltammetry (CV) and electrochemical impedance spectroscopy (EIS), Figure 5-3. Without oxygen, a quasi-rectangular shaped CV was obtained during charging and discharging of the supercapacitor from 0 to -1V, referring to the double-layer capacitive type charge storage (red curve in Figure 5-3a). With oxygen, the CV curve somewhat deviates from the rectangular shaped behavior and show increasing currents at voltages above -0.6 V and below -0.2 V (black curve). When the voltage window was reduced between -0.2 to -0.6V, the capacitive-like behavior was restored (blue curve). These results argue that the presence of O_2 in the gas mixture lowers the electrochemical capacitive window of carbon electrodes. Nyquist plots from EIS data showed a slight increase in solution resistance, slight decrease in diffusion resistance, deviation from the quasi-vertical behavior at low frequencies, and smaller imaginary impedance in the presence of 5% oxygen (Figure 5-3b). The capacitance increases from ~90F/g to ~150F/g when O_2 is present in the gas mixture (Figure 5-3c), suggesting reversible charge-transfer between the electrodes and adsorbed O_2, indicating the reversible formation of oxygen functionalities on the pore surface, which enhance the adsorption. In addition, there may also be partially reversible hydrogen peroxide formation at the negative electrode, which was recently proposed in capacitive deionization of aqueous solutions containing dissolved O_2.[151] Since the formation of hydrogen peroxide must be accompanied with hydroxide formation, enhanced CO_2 adsorption can also be explained via this mechanism. When the negative electrode is discharged, protons are produced as hydrogen peroxide is converted back into O_2, explaining CO_2 desorption. The irreversible fraction of the oxygen functionalization and hydrogen peroxide formation is likely responsible to the irreversible fraction of the adsorption and the low Coulomb efficiency. However, more investigations beyond the scope of this work are necessary to clarify these questions.

The lower diffusion resistance and larger capacitance from EIS plots suggest improved pore accessibility and increased pore wettability enhancing specific capacitcance.[109,140,151–153] Overall, SSA experiments with 15% CO_2/5% O_2/80% N_2 gas mixture using 3M $MgBr_2$ attained record adsorption capacity of ~750 mmol.kg^{-1} at an energy consumption of ~300 kJ.mol^{-1} at 0.6V, while low energy consumption of 85 kJ.mol^{-1} with a reversible adsorption capacity of ~66 mmol.kg^{-1} was achieved at 0.4 V.

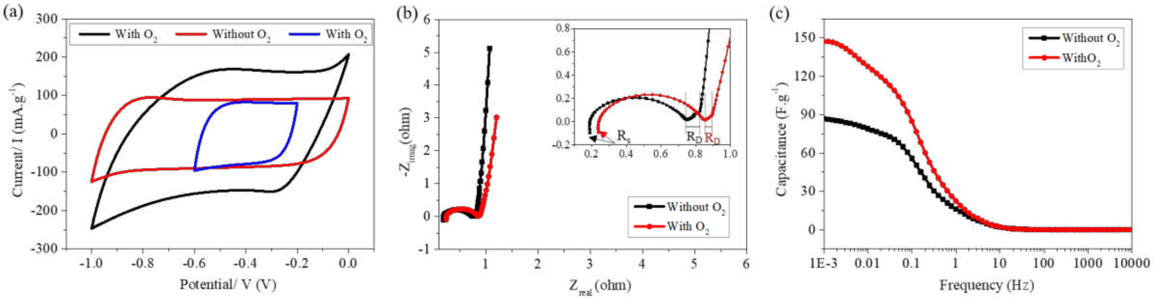

Figure 5-3 Influence of oxygen on electrochemical performance of the supercapacitor as the CO2/O2/N2 gas mixture is flown through the SSA module. (a) CV curves at 1V without O_2 (shown in red), at 1V with 5% O_2 (shown in black), at 0.4V with 5% O_2 (shown in blue), (b) Nyquist plots from EIS data showing changes in solution resistance (R_s) and diffusion resistance (R_d) in the presence of O_2, (c) Capacitance changes at different frequencies with and without O_2.

The influence of oxygen on CO_2 adsorption was further investigated with 3M $MgCl_2$ (Figure 5-4 and Figure S2), another deliquescent electrolyte. When a 15% CO_2/85% N_2 gas mixture is used, CO_2 sorption profiles during charging and discharging behave very similarly to those shown by electrodes infiltrated with 3M $MgBr_2$ electrolyte (Figure 5-4a and Figure 5-2a). A capacitance of ~80 $F.g^{-1}$, a resistance of ~9 $\Omega.cm^2$, a CO_2 adsorption capacity of 75 $mmol.kg^{-1}$, an adsorption rate of ~32 $\mu mol.kg^{-1}.s^{-1}$, a coulombic efficiency of ~98%, an energy efficiency of ~80%, an energy loss of ~4J and an energy consumption of ~73 $kJ.mol^{-1}$ were measured (Figure 4c-f). These numbers are similar to the results obtained with 3M $MgBr_2$.

The presence of 5% O_2 in the gas mixture resulted in much enhanced CO_2 sorption (Figure 5-4b). Unlike 3M $MgBr_2$, the use of 3M $MgCl_2$ electrolyte in the presence of oxygen allowed the use of a 1V voltage window with reversible and reproducible charging/discharging and CO_2 sorption profiles. This shows that Br^- becomes reactive at 1V in the presence of O_2, while Cl^- does not. A capacitance value of ~109 $F.g^{-1}$ and a sorption capacity of 320 $mmol.kg^{-1}$ was obtained, four times higher than without oxygen (Figure 4c-d). Unlike for 3M $MgBr_2$, the CO_2 concentration returned close to the 15% value at the end of the potential holding step, hence the uncertainty with regards to the reversibility is substantially smaller compared to the $MgBr_2$ electrolyte. The ratio of adsorbed to desorbed CO_2 is between 0.86 and 1.23, compared to 0.89 without O_2 at 1V (Figure S2). The electrodes were able to reversibly adsorb CO_2 for over 100 h at 1V (Figure S2e). Values smaller than 1 (0.86 and 0.89) may be attributed to CO_2 formation due to minor oxidation of the carbon electrode.[148] To investigate the possibility of increased CO_2 adsorption at higher voltages, the voltage window was increased from 1V to 1.2V. However, the GCD curve irreversibly deviated from the capacitive to faradaic behavior beyond 1V, suggesting that at voltages above 1V also Cl^- becomes reactive in the presence of O_2, and cannot be used (Figure S2f). Possibly, H_2O_2 diffuses from the negative to the positive electrode where it irreversibly oxidizes chloride ions in the double layer. The same mechanism may also explain the irreversible behavior of the bromide electrolyte at 1V. The different on-set voltage for Br^- and Cl^- degradation may be attributed to the more facile oxidation of Br^- relative to Cl^-. More studies beyond the scope of this work are needed to unambiguously answer these questions.

The coulombic efficiency, energy efficiency, and energy consumption at 1V is 60%, 22%, and 300 $kJ.mol^{-1}$ CO_2, respectively (Figure 5-4e-f). The low energy efficiency and higher energy consumption values in the presence of oxygen were attributed to the much longer voltage holding times (30 min without O_2 vs 90 min with O_2) required to achieve equilibrium CO_2 sorption and longer charging times (11 min without O_2 vs 15 min with O_2) due to the higher capacitance. To reduce the energy consumption of SSA in the presence of oxygen, additional experiments were performed by setting the voltage window between -0.2 to -0.8V and between 0 to -0.5V (Figure S2c-d). The smallest energy consumption in the presence of 5% O_2 (88 $kJ.mol^{-1}$ CO_2) was obtained at 0.5V, with other energetics and adsorptive performance metrics approaching the performance metrics obtained with CO_2/N_2 mixture without oxygen at 1V (Figure 5-4c-f). The reduced energy consumption, higher energy efficiency, and capacitive behavior of the electrodes at lower voltage-window was further confirmed from the quasi-rectangular CV curve at 0.5V compared to the CV curves at 0.6V and 1V (Figure S2g). Overall, the electrodes infiltrated with 3M $MgCl_2$ electrolyte allowed the use of a voltage window up to 1V in the presence of oxygen with stable cyclic performance, and a tradeoff between higher adsorption capacity and lower energy efficiency was observed. Overall, the adsorption capacities measured with Br^- as electrolyte are significantly higher compared to Cl^-. Possibly, bromide reacts with peroxo-surface functionalities, and H_2O_2 formed at the negative electrode to produce hypobromide (OBr^-) and H_2O. Hypobromide is a weak base, which may further increase the pH near the negative electrode leading to more CO_2 adsorption. Future in-situ pH and spectroscopic studies, which will be subject of future work may clarify these questions.

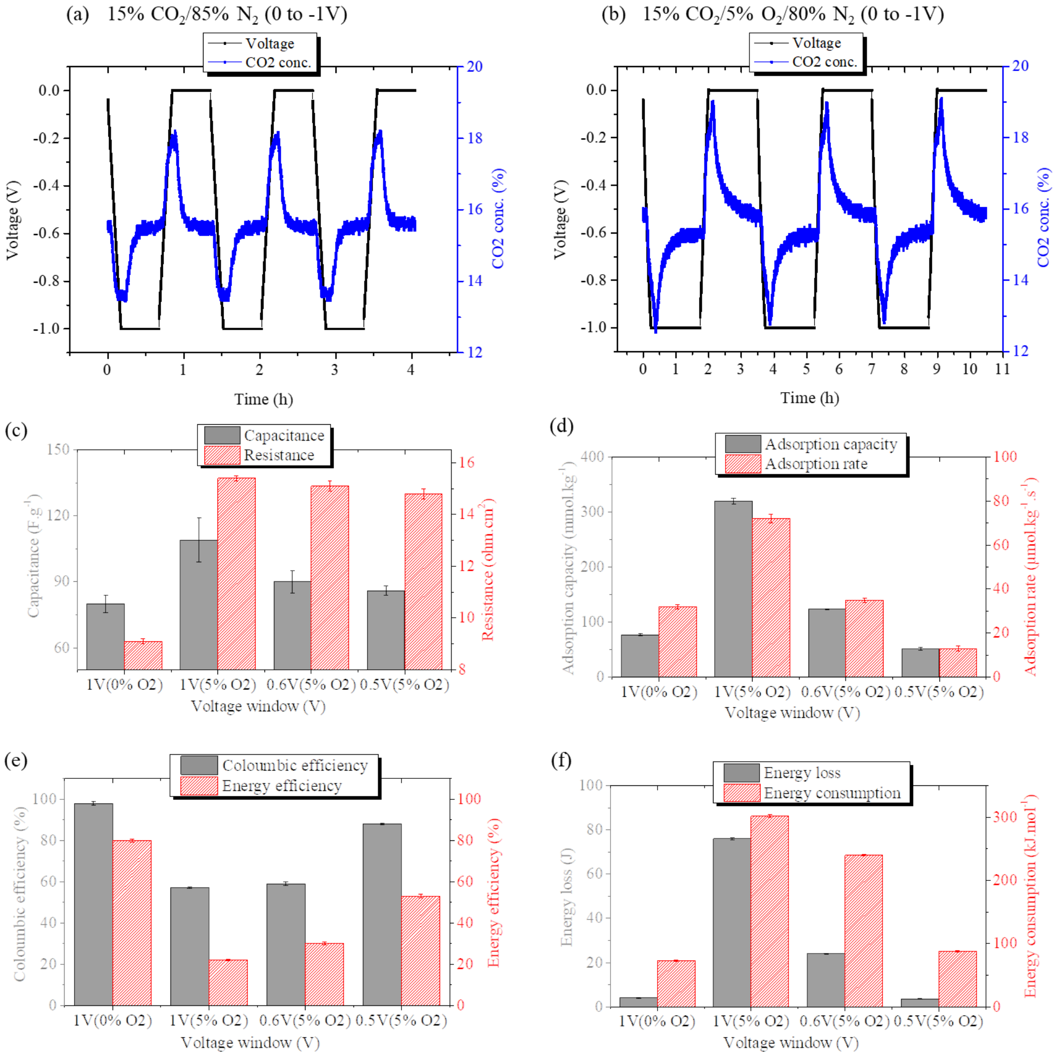

Figure 5-4 Voltage vs CO2 sorption profiles and corresponding energetics and adsorptive performance metrics of SSA with BPL electrodes and 3M MgCl2 electrolyte. (a) Voltage vs CO_2 at 1V with 15% CO_2/85% N_2 gas mixture, and (b) 15% CO_2/5% O_2/80% N_2 gas mixture. (c) Capacitance and resistance, (d) CO_2 adsorption capacity and adsorption rate, (e) coulombic efficiency and energy efficiency, (f) energy loss and energy consumption without O_2 at 1V, with 5% O_2 at 1V, 0.6V and 0.5V, respectively.

Further enhanced adsorption capacity and reduced energy consumption of SSA was observed with micro-mesoporous type garlic roots-derived activated carbon electrodes and $MgCl_2$ electrolyte (Figure 5-5 and Figure S3). The voltage changes and CO_2 sorption profiles during charging and discharging exhibit a reversible and reproducible behavior at different voltage windows (Figure S3). The capacitance increases from ~135 F.g^{-1} to ~250 F.g^{-1} while the sorption capacity increases remarkably from 150 mmol.kg^{-1} to 780 mmol.kg^{-1} at 1V as the gas mixture is switched from 15% CO_2/85% N_2 to 15% CO_2/5% O_2 80% N_2 (Figure 5-5a). Upper and the lower limits for the ratio of adsorbed to desorbed CO_2 are 0.98 and 1.49 respectively, signifying that most of the adsorption is reversible. Around 85% increase in capacitance is accompanied with 460% increase in CO_2 adsorption capacity in the presence of 5% O_2. These findings are in line with previously obtained results from BPL carbon where the capacitance increased 40% and CO_2 adsorption capacity increased 320% when 5% O_2 was used in the gas mixture. Nonetheless, an adsorption capacity of ~780 mmol.kg^{-1} obtained at an energy consumption of ~220 kJ.mol^{-1} approaches the benchmarks set in conventional amine-based CO_2 capture methods.[23] Despite the higher adsorption capacity and reduced energy consumption with garlic roots-derived electrodes, the average coulombic efficiency of SSA charging and discharging cycles at 1V stayed around 60 % when O_2 is used in the gas mixture (Figure 5-5a). To find the possibility of improving the coulombic efficiency and energy consumption by minimizing the voltage holding time, the voltage and CO_2 concentration curve in Figure S3b was analyzed for 0 min, 30 min, and 60 min of holding after charging (Table S2). The coulombic efficiency improved to ~84%, and an adsorption capacity of ~350 mmol.kg^{-1} at an energy consumption of 130 kJ.mol^{-1} is obtained at 0 min of voltage hold, signifying the need to minimize the voltage holding times via the enhancement of adsorption rates. Minimizing the voltage window from 1 V to 0.6, 0.5, 0.4 and 0.3 V also improved the coulombic efficiency to as high as 99% (at

0.3V) and energy consumption to as low as 35 kJ.mol^{-1} (at 0.3V), but at smaller sorption capacity of ~40 mmol.kg^{-1} (Figure 5a). In order to understand the influence of the oxygen concentration, we performed additional experiments at 10, 15, and 20% O_2 while keeping the CO_2 concentration constant at 15%. Nearly identical energetic and adsorptive performance was observed at all three concentrations (Figure S4 and Table S3), showing the insensitivity of SSA to variable oxygen concentrations.

The adsorption of CO_2 relative to O_2 was investigated by simultaneously measuring the concentration changes of both gases during charging and discharging cycles at a voltage window of 0.5 V (Figure 5-5b). On the same concentration scale, the changes in O_2 concentration relative to the changes in CO_2 concentration are barely noticeable (only 0.05% change for O_2 compared to ~1.5% for CO_2). Zooming in into the O_2 concentration curves shows that while a charging cycle corresponds to CO_2 adsorption and a discharging cycle corresponds to CO_2 desorption, initial desorption followed by adsorption of O_2 was measured during charging. During discharging, fast adsorption followed by slower adsorption of O_2 is observed. The average moles adsorbed during charging cycles is about 52 mmol CO_2 and 4.4 mmol O_2 per kg of electrode active mass.

To find the changes taking place on the electrodes when exposed to the $CO_2/O_2/N_2$ gas mixture, we conducted in-situ Raman spectroscopy experiments with a modified SSA cell (Figure S5). No additional peak except SiO_2 vibrational modes (around 500 cm^{-1},900 cm^{-1}, 1100 cm^{-1} coming from the Quartz window), D band (~1350 cm^{-1}), and G band (~1600 cm^{-1}) was observed (Figure S5b), regardless the presence or direction (-1V and +1V) of the potential. The results show that the electrodes are stable at the conditions measured, but the measurements were not sensitive enough to reveal changes in the surface functional groups following charge and discharge.

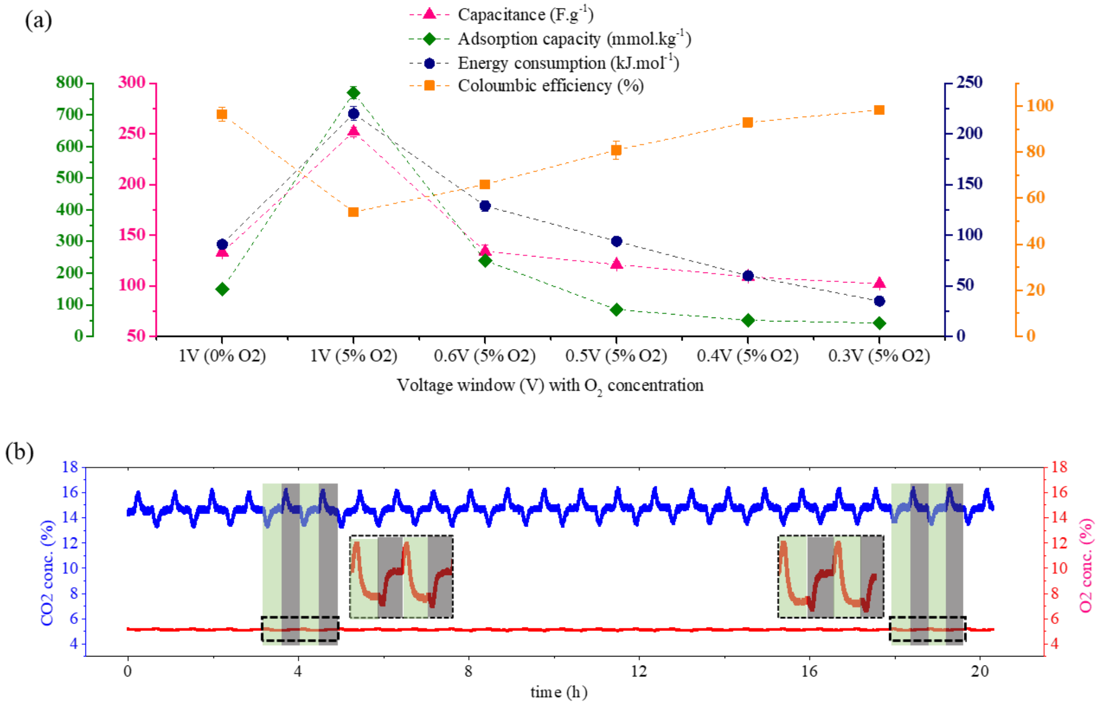

Figure 5-5 Performance metrics of SSA with garlic roots-derived activated carbon electrodes and 3M MgCl2 electrolyte. (a) Capacitance, adsorption capacity, energy consumption, and coulombic efficiency comparison at 1V without oxygen, and 1V, 0.6V, 0.5V, 0.4V, 0.3V with oxygen. (b) Simultaneous measurement of CO_2 and O_2 concentration changes during charging and discharging of the electrodes at 0.5V.

5.3 Conclusions

Greatly enhanced adsorption capacities and adsorption kinetics are observed when a 15% CO_2/85% N_2 gas mixture is replaced with 15% CO_2/5% O_2/80% N_2. We report 11 times increase in CO_2 adsorption capacity (~750 $mmol.kg^{-1}$) with coal-derived BPL electrodes using 3M $MgBr_2$ electrolyte at 0.6V, and 4-5 times increase in CO_2 adsorption capacity with coal-derived BPL electrodes (320 $mmol.kg^{-1}$) and garlic roots-derived micro-mesoporous electrodes (~780 $mmol.kg^{-1}$) using 3M $MgCl_2$ electrolyte at 1V in the presence of oxygen. The coulombic efficiency, energy efficiency and energy consumption improved significantly as the voltage window was systematically reduced from 1V to 0.3V, or the voltage holding time was lowered from 60 min to 0 min, but at the expense of lower adsorption capacity. Small, partially reversible changes in O_2 concentrations were observed during the charge-discharge cycles, indicating selectivity of CO_2 over O_2 at 0.5 V. Varying the oxygen concentrations (10%, 15%, 20%) gave similar energetic and adsorptive performance. The enhanced reversible CO_2 adsorption in the presence of O_2 can be attributed to the enhanced specific capacitance in the presence of O_2, which may be due to reversible formation of oxygen surface functionalities, and oxygen reduction to form hydrogen peroxide.

5.4 Supporting Information

Table S1 Energetics and adsorptive performance metrics with BPL electrodes and 3M $MgBr_2$ electrolyte.

Parameter		**Without Oxygen (0 to -1V)**	**With Oxygen (0 to -1V)**	**With Oxygen (-0.2 to -0.8V)**	**With Oxygen (-0.2 to -0.6V)**
Energetic metrics					
ESR (Ω.cm^2)	at low V	8.04 ± 0.1	29.2 ± 4.1	8.77 ± 0.1	8.3 ± 0.2
	at high V	8.24 ± 0.1	53.4 ± 2.3	15.4 ± 0.2	9.2 ± 0.1
C_s (F.g^{-1})		90.1 ± 0.8	1451 ± 438*	249 ± 10.5	94.5 ± 0.4
t_g		699 ± 6.2	11679 ± 3529	1173 ± 49.6	453 ± 1.1
η_c (%)		97.2 ± 0.7	39.6 ±5.9	33.4 ± 0.2	88.0 ± 0.1
η_e (%)		80.8 ± 0.7	7.01 ± 1.3	8.1 ± 0.3	67.3 ± 0.1
ΔE (J)		4.07 ± 0.2	498 ± 151	190 ± 1.7	4.62 ± 0.1
Adsorptive metrics					
n avg. adsorbed (µmol) n avg. desorbed, upper limit (µmol)		50.9 ± 1.4 (51.4 ± 1.1)	1220 ± 318	595 ± 5.1 (593 ± 8.0)	54.0 ± 1.5 (54.6 ± 1.7)
AC (mmol.kg^{-1})		64.9 ± 1.7	1590 ± 334	742 ± 63.1	66.3 ± 1.7
AC (mmol.m^{-2})		16.4 ± 0.4	394 ± 102	191 ± 16.2	17.6 ± 0.5
AC (mol.m^{-3})		23.5 ± 0.6	606 ± 158	273 ± 23.2	25.1 ± 0.7
AR (µmol.kg^{-1}.s^{-1})		40.9 ± 1.0	49.5 ± 6.2	120 ± 0.7	38.4 ± 1.0
P (mmol.h^{-1}.m^{-2})		14.6 ± 0.4	44.0 ± 7.8	111 ± 0.6	34.5 ± 1.0
CE (_)		0.13 ± 0.0	0.17 ± 0.0	0.22 ± 0.0	0.17 ± 0.0
EC (kJ.mol^{-1})		80.4 ± 1	485 ± 32.8	302 ± 1.7	85.0 ± 2.0

* The much higher number is due to faradaic reactions and does not refer to capacitance.

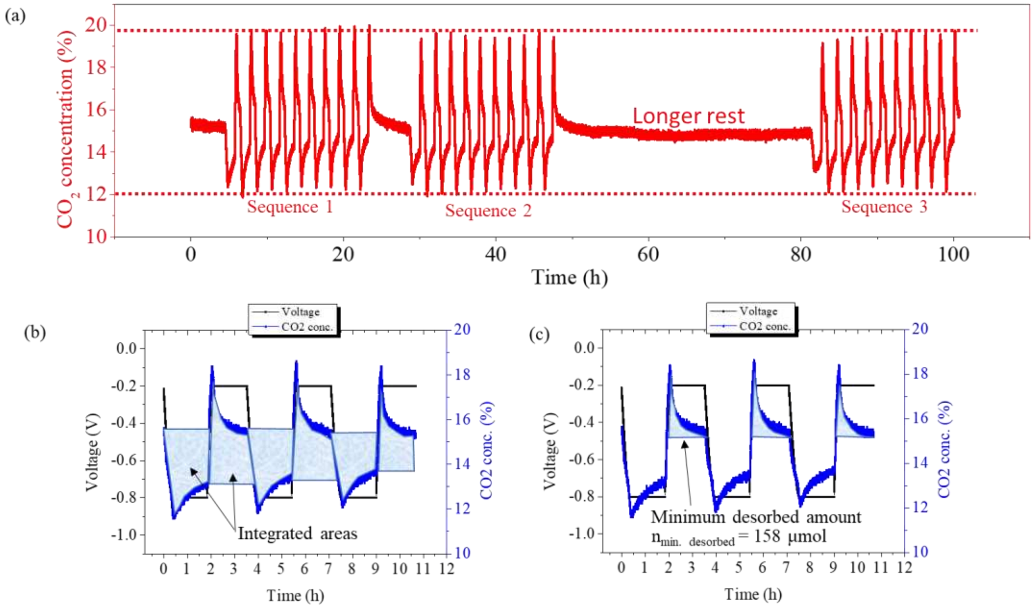

Figure S1 Changes in CO_2 concentration during SSA cycling from -0.2 to -0.8V with BPL electrodes and 3M $MgBr_2$ electrolyte (a), Maximum integrated areas during incomplete sorption (b), integrated areas showing minimum moles desorbed (c).

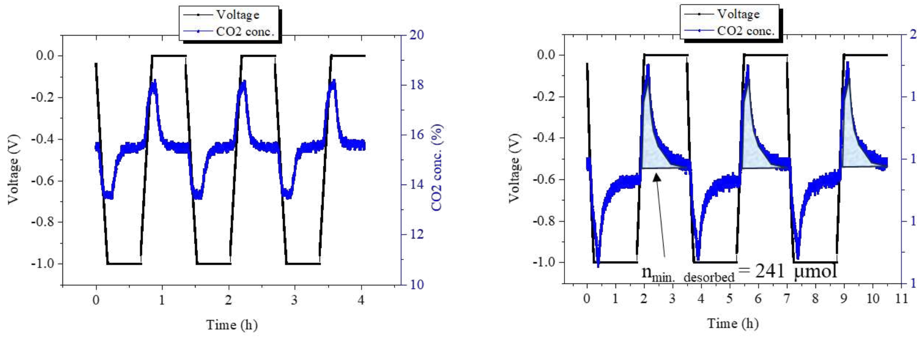

(a) 15% CO_2/85% N_2 (0 to -1V)

(b) 15% CO_2/5% O_2/80% N_2 (0 to -1V)

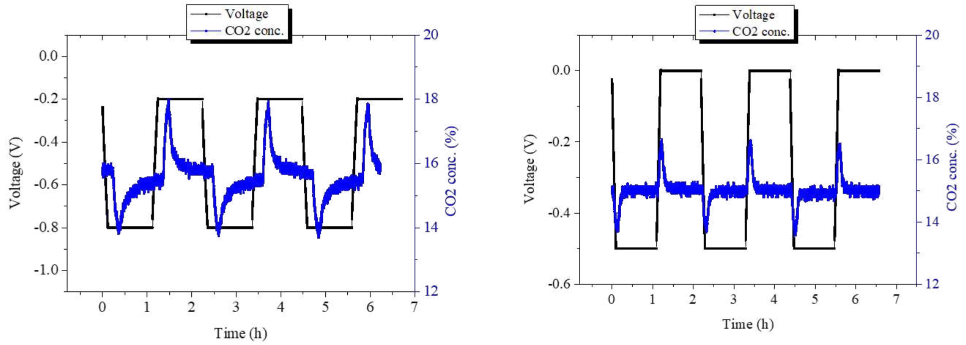

(c) 15% CO_2/5% O_2/80% N_2 (-0.2 to -0.8V)

(d) 15% CO_2/5% O_2/80% N_2 (-0.2 to -0.6V)

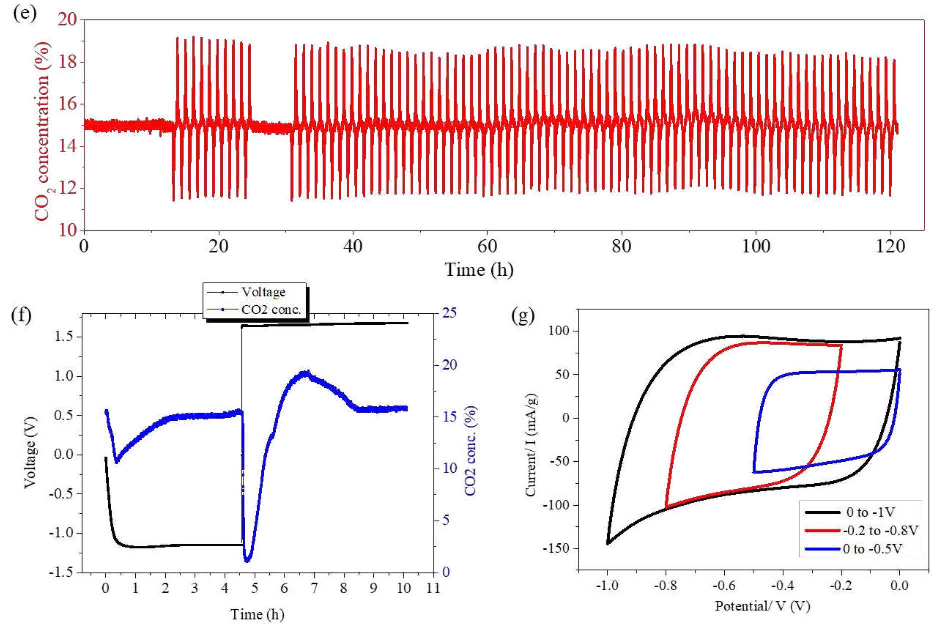

Figure S2 SSA experiments with BPL electrodes and 3M $MgCl_2$ electrolyte. Voltage and CO_2 concentration changes from 0 to -1V without oxygen (a) and from 0 to -1V (b), -0.2

to -0.8 (c), 0 to -0.5 (d) with oxygen. Cyclic stability for over 100 h in the presence of oxygen (e). SSA experiments at 1.2 V showing large irreversibility in the presence of 15% CO_2/5% O_2/80% N_2 (f). CV curves at different voltage windows in the presence of 15% CO_2/5% O_2/80% N_2 gas mixture (g).

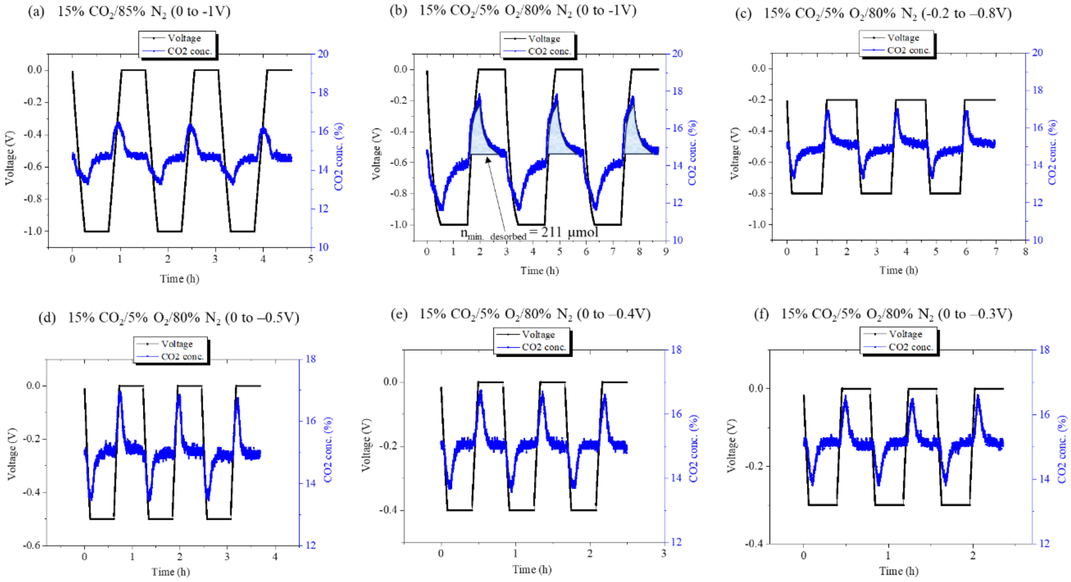

Figure S3 SSA experiments with garlic roots derived carbon electrodes and 3M $MgCl_2$ electrolyte. Voltage and CO_2 concentration changes from 0 to -1V without oxygen (a) and from 0 to -1V (b), -0.2 to -0.8 (c), 0 to -0.5 (d) 0 to -0.4V (e), 0 to -0.3V (f) with oxygen, respectively.

Table S2 Energetics and adsorptive performance metrics with garlic roots derived electrodes and 3M $MgCl_2$ electrolyte at different voltage holding times. The data is extracted from Figure S4b

Parameter	**0 min hold**	**30 min hold**	**60 min hold**
Energetic metrics			
η_c (%)	84.2	63.4	54.0
η_e (%)	53.5	28.0	21.3
ΔE (J)	16.1	48.0	69.0
Adsorptive metrics			
n avg. adsorbed (µmol)	139	266	313
n avg. desorbed, upper limit (µmol)	143	271	319
AC (mmol.kg^{-1})	352	665	783
AR (µmol.kg^{-1}.s^{-1})	195	180	146
EC (KJ.mol^{-1})	130	187	221

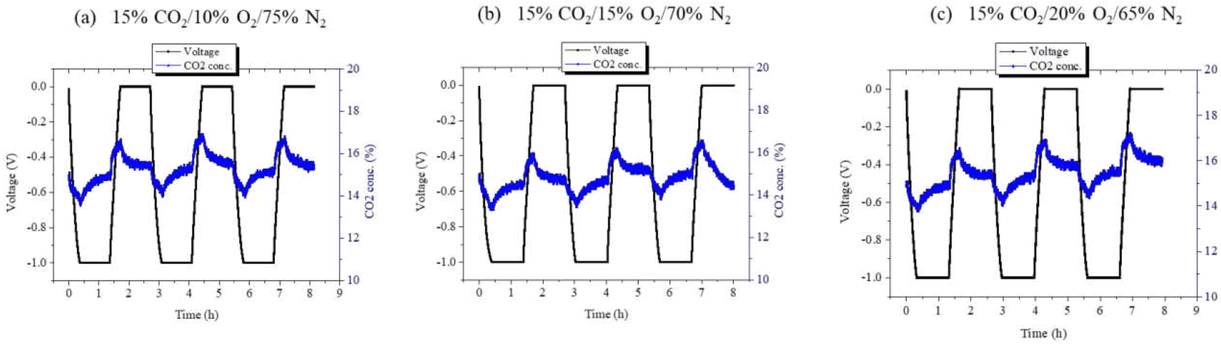
(a) 15% CO_2/10% O_2/75% N_2

(b) 15% CO_2/15% O_2/70% N_2

(c) 15% CO_2/20% O_2/65% N_2

Figure S4 Voltage and CO_2 concentration changes at using 10% (a), 15% (b), and 20% O_2 during SSA cycles.

Table S3 Energetics and adsorptive performance metrics with garlic roots derived electrodes and 3M $MgCl_2$ electrolyte at different oxygen concentrations.

Gas composition		**10% O_2/15% CO_2**	**15% O_2/15% CO_2**	**20% O_2/15% CO_2**
Energetic metrics				
ESR (Ω.cm^2)	at 0 V	10.5	9.6	12.2
	at -1 V	12.6	12.2	14.4
C_s (F.g^{-1})		186	187	166
t_g		1310	1313	1170
η_c (%)		54.1	56.1	60.2
η_e (%)		24.7	24.8	26.9
ΔE (J)		50.2	48.4	42.8
Adsorptive metrics				
n avg. (µmol)		**216 (270)**	**195 (238)**	**217 (286)**
AC (mmol.kg^{-1})		541	488	543
AC (mmol.m^{-2})		70.1	62.8	70.0
AC (mol.m^{-3})		63.6	57.2	63.6
AR (µmol.kg^{-1}.s^{-1})		111	100	114
P (mmol.h^{-1}.m^{-2})		25.7	23.3	26.4
CE (_)		0.26	0.24	0.28
EC (KJ.mol^{-1})		232	250	213

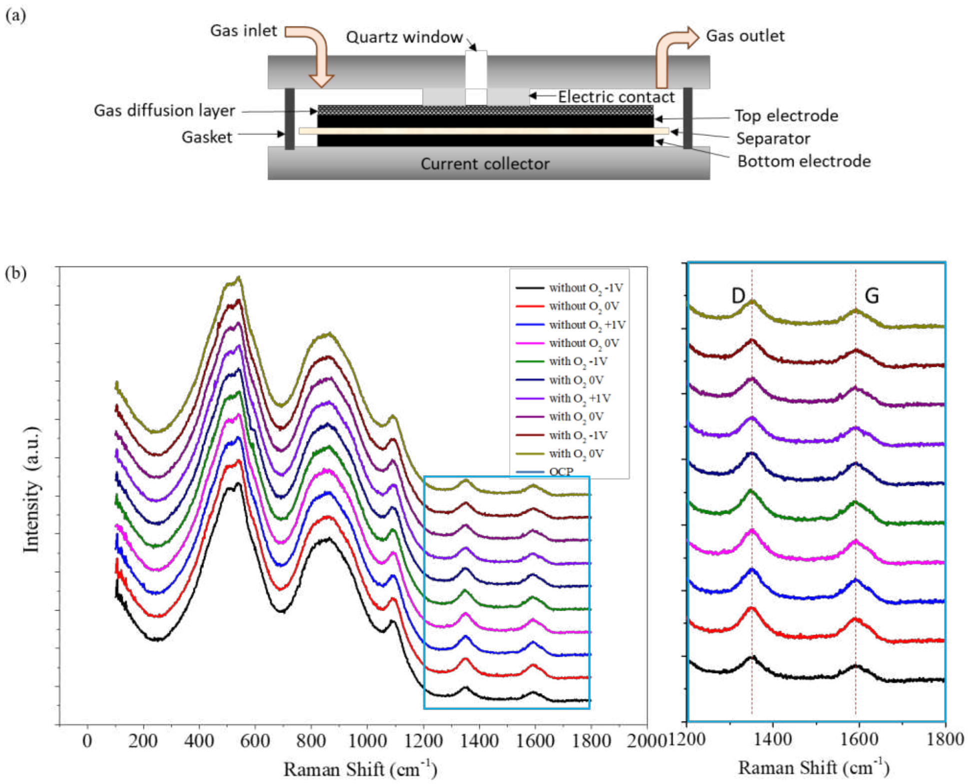

Figure S5 SSA cell designed for in-situ Raman spectroscopy (a), Raman spectra of the electrodes exposed to $CO_2/N_2/O_2$ gas mixture at differnet voltages showing negligible differences.

In situ Raman characterization of the electrodes

In situ Raman spectra were collected on a Horiba LabRam-HR Raman spectrometer using a 532 nm excitation wavelength laser source (Oxxius, filtered to 1.5 mW) and a thermoelectrically cooled Horiba Synapse BIDD scientific CCD camera detector. The laser was focused through a quartz window onto the top electrode as shown in Figure S5a, with a 5x objective (Olympus MPLN5X) while the spectrometer was used with a 500 nm grating and a 100 μm hole, resulting in a spectral resolution of ~1.7 cm^{-1}. The

520.7 cm^{-1} band of a silicon wafer standard was used for calibration prior to spectral acquisition. Spectra was collected at several different voltages with and without oxygen in the gas mixture.

CHAPTER 6: CONCLUSION AND FUTURE DIRECTIONS

6.1 Key takeaways

The systematic research presented in this thesis proves the following hypothesis:

1. New activated carbons with high surface areas and high specific capacitances are indispensable to improve the SSA performance.

2. Biomass-derived carbon from garlic roots show the best CO_2 sorption capacity among all tested carbons due to its high surface area and micro-mesoporous nature.

3. High-mass loading, hot-pressed garlic roots derived activated carbons provide much improved areal and volumetric sorption capacities compared to the electrodes prepared through rolling method without hot pressing.

4. A voltage window of 1.4V provides the highest adsorption capacity of 524 mmol/kg (at energy consumption of 130 kJ/mol) and stable performance up to 100 h of operation with 15% CO_2/85% N_2 gas mixture. The capacitive behavior is maintained up to 1.4V.

5. Using 15% CO_2/5% O_2/80% N_2 gas mixture, a record adsorption capacity of 780 mmol/kg at an energy consumption of 220 kJ/mol is achieved with garlic roots-derived activated carbon electrodes.

6. SSA in the presence of oxygen results in improved the CO_2 adsorption capacity of the electrodes at the expense of increased energy consumption. Energetics and adsorptive performance of SSA with 3M $MgCl_2$ electrolyte in the presence of oxygen at 0.5 V are similar to the energetics and adsorptive performance metrics in the absence of oxygen at 1V.

6.2 Remaining challenges and Future directions

6.2.1 Improving the kinetics

In this research, the kinetics of CO_2 sorption improved from ~20 μmol kg^{-1} s^{-1} to ~80 μmol kg^{-1} s^{-1} by using biomass-derived electrodes. However, further improvements are required to reduce the cost and increase productivity. The use of activators and additives can increase the CO_2 hydrolysis rate. A naturally occurring enzyme that is known to catalyze the conversion of carbon dioxide to bicarbonate at high rates is carbonic anhydrase (CA). The activity of this enzyme is derived from Zn^{2+} cation in the center attached with three histidines. CO_2 hydration occurs when Zn^{2+} abstracts an H^+ from surrounding H_2O, forming an OH^- which can attack the electrophilic carbon to form HCO_3^-.[154,155] However, the preliminary SSA testing in the presence of carbonic anhydrase did not show any improvements in the sorption kinetics (Figure 6-1). The CO_2 adsorption capacity decreased from 38 mmol.Kg^{-1} to 29 mmol.Kg^{-1} upon the addition of carbonic anhydrase (CA), arguing that the size of CA molecule is too big, and it may have blocked the pores of the electrodes which can hinder the capacitive carbon capture. Other CA mimics with Zn containing ion and smaller size needs to be investigated. Additives such as Boric acid, borate salts, amino acids, and amines have also shown improved CO_2 hydrolysis rates in conventional alkali CO_2 capture processes.[156] In situ pH studies are needed to study the influence of additives on SSA kinetics.

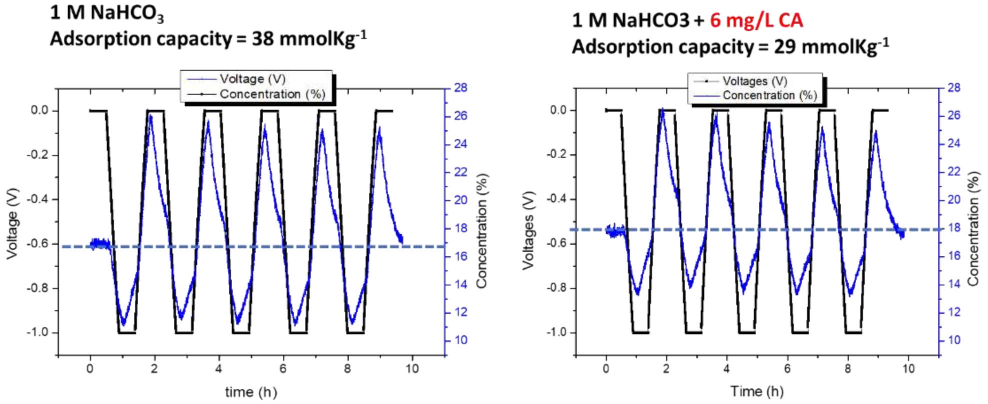

Figure 6-1 SSA tests without (left) and with (right) using carbonic anhydrase. The black lines show voltage profiles during charging, discharging, and holding steps. The blue lines show the CO2 concentration changes during charging and discharging

6.2.2 Improving current densities

Applying higher currents also improved the sorption kinetics but results in higher voltage drop and increased energy consumption (Figure 6-2). A systematic study on minimizing the energy consumption and maintaining the sorption kinetics by using thinner electrodes and developing different pore architectures will be helpful to optimize the SSA kinetics. Recent advances in supercapacitor materials which provide ultra-fast charge storage kinetics at higher current densities with minimal resistive losses can be a helpful starting point for SSA research in this direction.[157–160]

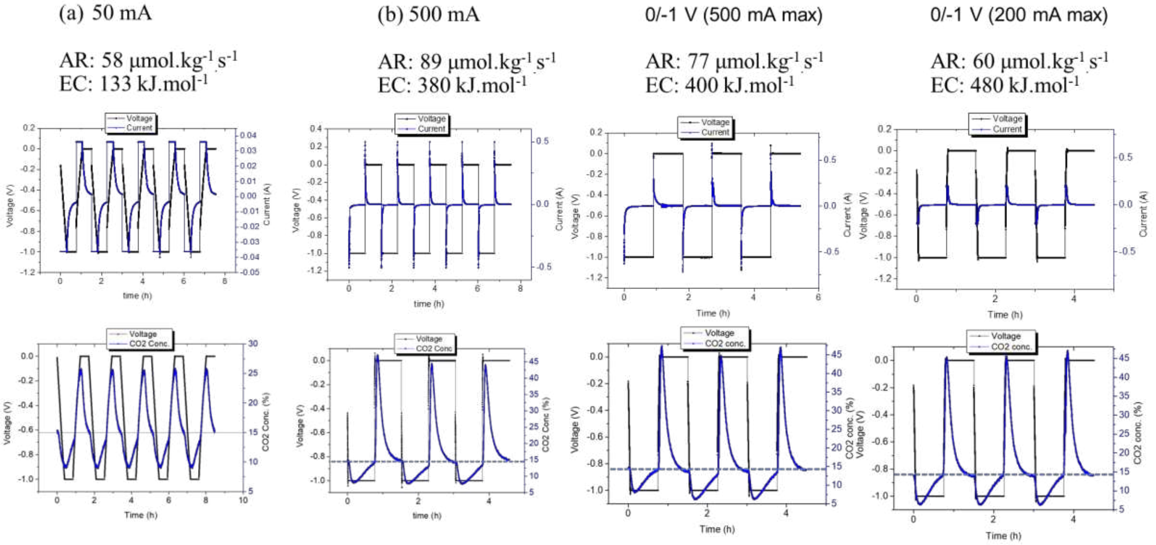

(a) 50 mA
AR: 58 μmol.kg^{-1} s^{-1}
EC: 133 kJ.mol^{-1}

(b) 500 mA
AR: 89 μmol.kg^{-1} s^{-1}
EC: 380 kJ.mol^{-1}

0/-1 V (500 mA max)
AR: 77 μmol.kg^{-1} s^{-1}
EC: 400 kJ.mol^{-1}

0/-1 V (200 mA max)
AR: 60 μmol.kg^{-1} s^{-1}
EC: 480 kJ.mol^{-1}

Figure 6-2 Higher currents leads to improved kinetics but increased energy consumption

6.3 SSA; A promising CO$_2$ capture technology

Although great room for improvement is available to further increase the SSA sorption capacity, minimize the energy consumption, and improve the sorption kinetics, the research presented in this thesis provides a deeper understanding of the relationship between different performance metrics and a step forward towards commercialization. SSA has the potential to easily scale-up and can be applied to a variety of small and large-scale applications including natural gas purification, CO$_2$ enrichment for green houses, and water carbonation. Future research towards new materials development and optimizing different performance parameters (as shown in Figure 6-3) will help chemists and engineers to generate a novel flue gas as well as direct air capture technology having significant energy, environmental, cost, scalability, and stability advantages over existing methods. In addition, SSA can serve as energy-storage technology and the capacitive energy can be utilized for specific, on-demand applications.

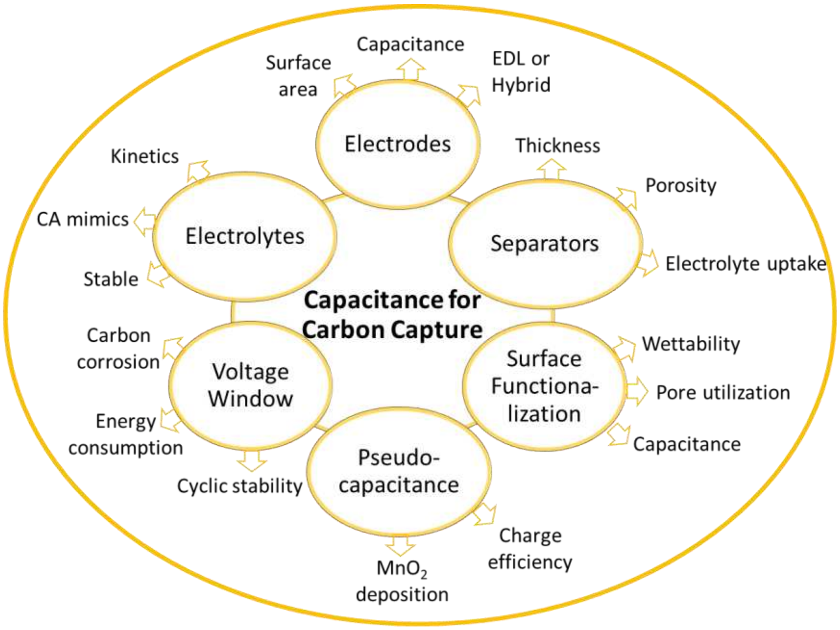

Figure 6-3 Potential research directions to improve the energetics and adsorptive performance metrics of SSA

References

(1) Arrhenius, S. XXXI. On the Influence of Carbonic Acid in the Air onthe Temperature of the Ground. *London, Edinburgh, Dublin Philos. Mag. J. Sci.* **1896**, *41* (251), 237–276.

(2) Keeling, R. F.; Graven, H. D. Insights from Time Series of Atmospheric Carbon Dioxide and Related Tracers. *Annu. Rev. Environ. Resour.* **2021**, *46*, 85–110. https://doi.org/10.1146/annurev-environ-012220-125406.

(3) Lindsey, R. Climate Change: Atmospheric Carbon Dioxide. *NOAA Clim.* **2020**, 1–5.

(4) Sharifian, R.; Wagterveld, R. M.; Digdaya, I. A.; Xiang, C.; Vermaas, D. A. Electrochemical Carbon Dioxide Capture to Close the Carbon Cycle. *Energy Environ. Sci.* **2021**, *14* (2), 781–814. https://doi.org/10.1039/d0ee03382k.

(5) IPCC. Technical Summary. *Ocean Cryosph. a Chang. Clim.* **2022**, 39–70. https://doi.org/10.1017/9781009157964.002.

(6) Fuss, S.; Lamb, W. F.; Callaghan, M. W.; Hilaire, J.; Creutzig, F.; Amann, T.; Beringer, T.; De Oliveira Garcia, W.; Hartmann, J.; Khanna, T.; Luderer, G.; Nemet, G. F.; Rogelj, J.; Smith, P.; Vicente, J. V.; Wilcox, J.; Del Mar Zamora Dominguez, M.; Minx, J. C. Negative Emissions - Part 2: Costs, Potentials and Side Effects. *Environ. Res. Lett.* **2018**, *13* (6), 2016–2050. https://doi.org/10.1088/1748-9326/aabf9f.

(7) Sharifian, R.; Wagterveld, R. M.; Digdaya, I. A.; Xiang, C.; Vermaas, D. A. Electrochemical Carbon Dioxide Capture to Close the Carbon Cycle. *Energy Environ. Sci.* **2021**, *14* (2), 781–814. https://doi.org/10.1039/d0ee03382k.

(8) Choi, S.; Drese, J. H.; Jones, C. W. Adsorbent Materials for Carbon Dioxide Capture from Large Anthropogenic Point Sources. *ChemSusChem* **2009**, *2* (9), 796–854. https://doi.org/10.1002/cssc.200900036.

(9) Shi, X.; Xiao, H.; Azarabadi, H.; Song, J.; Wu, X.; Chen, X.; Lackner, K. S. Sorbents for the Direct Capture of CO 2 from Ambient Air. *Angew. Chemie - Int. Ed.* **2020**, 6984–7006.

https://doi.org/10.1002/anie.201906756.

(10) Bottoms, R. R. Process for Separating Acidic Gases, 1930.

(11) Renfrew, S. E.; Starr, D. E.; Strasser, P. Electrochemical Approaches toward CO2Capture and Concentration. *ACS Catal.* **2020**, *10* (21), 13058–13074. https://doi.org/10.1021/acscatal.0c03639.

(12) Shi, X.; Lin, Y.; Chen, X. Development of Sorbent Materials for Direct Air Capture of CO2. *MRS Bull.* **2022**, *47* (April). https://doi.org/10.1557/s43577-022-00320-7.

(13) Yaumi, A. L.; Bakar, M. Z. A.; Hameed, B. H. Recent Advances in Functionalized Composite Solid Materials for Carbon Dioxide Capture. *Energy* **2017**, *124*, 461–480. https://doi.org/10.1016/j.energy.2017.02.053.

(14) Gelles, T.; Lawson, S.; Rownaghi, A. A.; Rezaei, F. *Recent Advances in Development of Amine Functionalized Adsorbents for CO2 Capture*; Springer US, 2020; Vol. 26. https://doi.org/10.1007/s10450-019-00151-0.

(15) Fasihi, M.; Efimova, O.; Breyer, C. Techno-Economic Assessment of CO 2 Direct Air Capture Plants. *J. Clean. Prod.* **2019**, *224*, 957–980. https://doi.org/10.1016/j.jclepro.2019.03.086.

(16) Zhang, W.; Liu, H.; Sun, Y.; Cakstins, J.; Sun, C.; Snape, C. E. Parametric Study on the Regeneration Heat Requirement of an Amine-Based Solid Adsorbent Process for Post-Combustion Carbon Capture. *Appl. Energy* **2016**, *168*, 394–405. https://doi.org/10.1016/j.apenergy.2016.01.049.

(17) Anderson, C.; Hooper, B.; Qader, A.; Harkin, T.; Smith, K.; Mumford, K.; Pandit, J.; Ho, M.; Lee, A.; Nicholas, N.; Indrawana, I.; Gouw, J.; Xiao, J.; Thanumurthy, N.; Temple, N.; Stevens, G.; Wiley, D. Recent Developments in the UNO MK 3 Process - A Low Cost, Environmentally Benign Precipitating Process for CO2 Capture. *Energy Procedia* **2014**, *63*, 1773–1780. https://doi.org/10.1016/j.egypro.2014.11.184.

(18) Zeman, F. Energy and Material Balance of CO2 Capture from Ambient Air. *Environ. Sci. Technol.* **2007**, *41* (21), 7558–7563. https://doi.org/10.1021/es070874m.

(19) Keith, D. W.; Holmes, G.; St. Angelo, D.; Heidel, K. A Process for Capturing CO2 from the

Atmosphere. *Joule* **2018**, *2* (8), 1573–1594. https://doi.org/10.1016/j.joule.2018.05.006.

(20) HUEBSCHER RG; BABINSKY AD. Electrochemical Concentration and Separation of Carbon Dioxide for Advanced Life Support Systems. Carbonation Cell System. *SAE-Paper 690640* **1969**, *78*, 2164–2170.

(21) Zito, A. M.; Clarke, L. E.; Barlow, J.; Bím, D.; Zhang, Z.; Ripley, K.; Li, C.; Kummeth, A.; Leonard, M. E.; Alexandrova, A. N.; Brushett, F.; Yang, Y. Electrochemical Carbon Dioxide Capture and Concentration. *Chem. Rev.* **2023**, 1–52. https://doi.org/10.1021/acs.chemrev.2c00681.

(22) Kang, M. P.; Winnick, J. Concentration of Carbon Dioxide by a High-Temperature Electrochemical Membrane Cell. *J. Appl. Electrochem.* **1985**, *15* (3), 431–439. https://doi.org/10.1007/BF00615996.

(23) Seo, H.; Rahimi, M.; Hatton, T. A. Electrochemical Carbon Dioxide Capture and Release with a Redox-Active Amine. *J. Am. Chem. Soc.* **2022**, *144* (5), 2164–2170. https://doi.org/10.1021/jacs.1c10656.

(24) Rahimi, M.; Diederichsen, K. M.; Ozbek, N.; Wang, M.; Choi, W.; Hatton, T. A. An Electrochemically Mediated Amine Regeneration Process with a Mixed Absorbent for Postcombustion CO2Capture. *Environ. Sci. Technol.* **2020**, *54* (14), 8999–9007. https://doi.org/10.1021/acs.est.0c02595.

(25) Jin, S.; Wu, M.; Jing, Y.; Gordon, R. G.; Aziz, M. J. Low Energy Carbon Capture via Electrochemically Induced PH Swing with Electrochemical Rebalancing. *Nat. Commun.* **2022**, *13* (1). https://doi.org/10.1038/s41467-022-29791-7.

(26) Bachman, E.; Tavasoli, A.; Hatton, T. A.; Maravelias, C. T.; Haites, E.; Styring, P.; Macintosh, J.; Ozin, G. Rail-Based Direct Air Carbon Capture Ll Future Energy. *Joule* **2022**, 1368–1381. https://doi.org/10.1016/j.joule.2022.06.025.

(27) Kang, J. S.; Kim, S.; Hatton, T. A. Redox-Responsive Sorbents and Mediators for Electrochemically Based CO2 Capture. *Curr. Opin. Green Sustain. Chem.* **2021**, *31*, 100504. https://doi.org/10.1016/j.cogsc.2021.100504.

(28) Alan Hatton. Redox-Tunable Lewis Bases for Electrochemical Carbon Dioxide Capture. *Nat. Energy* **2022**.

(29) Voskian, S.; Hatton, T. A. Faradaic Electro-Swing Reactive Adsorption for CO2 Capture. *Energy Environ. Sci.* **2019**, *12* (12), 3530–3547. https://doi.org/10.1039/c9ee02412c.

(30) Diederichsen, K. M.; Liu, Y.; Ozbek, N.; Seo, H.; Hatton, T. A. Toward Solvent-Free Continuous-Flow Electrochemically Mediated Carbon Capture with High-Concentration Liquid Quinone Chemistry. *Joule* **2022**, *6* (1), 221–239. https://doi.org/10.1016/j.joule.2021.12.001.

(31) Rahimi, M.; Khurram, A.; Hatton, T. A. Electrochemical Carbon Capture Processes for Mitigation of CO2 Emissions. *Chem Soc Rev* **2022**. https://doi.org/10.1039/d2cs00443g.

(32) Kyle M. Diederichsen; Sharifian, R.; Jin Soo Kang; Yayuan Liu; Kim, S.; Gallant, B. M.; Vermaas, D.; T. Alan Hatton. Electrochemical Methods for Carbon Dioxide Separations. *Nat. Rev. Methods Prim.* **2022**, *68*. https://doi.org/10.1038/s43586-022-00148-0.

(33) Massen-Hane, M.; Diederichsen, K. M.; Hatton, T. A. Engineering Redox-Active Electrochemically Mediated Carbon Dioxide Capture Systems. *Nat. Chem. Eng.* **2024**, *1* (1), 35–44. https://doi.org/10.1038/s44286-023-00003-3.

(34) Seo, H.; Nitzsche, M. P.; Hatton, T. A. Redox-Mediated PH Swing Systems for Electrochemical Carbon Capture. *Acc. Chem. Res.* **2023**, *56* (22), 3153–3164. https://doi.org/10.1021/acs.accounts.3c00430.

(35) Jin, S.; Wu, M.; Gordon, R. G.; Aziz, M. J.; Kwabi, D. G. PH Swing Cycle for CO2capture Electrochemically Driven through Proton-Coupled Electron Transfer. *Energy Environ. Sci.* **2020**, *13* (10), 3706–3722. https://doi.org/10.1039/d0ee01834a.

(36) Li, X.; Zhao, X.; Liu, Y.; Hatton, T. A. Redox-Tunable Lewis Bases for Electrochemical Carbon Dioxide Capture. *Nat. Energy* **2022**.

(37) Wang, M.; Herzog, H. J.; Hatton, T. A. CO2 Capture Using Electrochemically Mediated Amine Regeneration. *Ind. Eng. Chem. Res.* **2020**, *59* (15), 7087–7096. https://doi.org/10.1021/acs.iecr.9b05307.

(38) Stern, M. C.; Simeon, F.; Herzog, H.; Hatton, T. A. Post-Combustion Carbon Dioxide Capture Using Electrochemically Mediated Amine Regeneration. *Energy Environ. Sci.* **2013**, *6* (8), 2505–2517. https://doi.org/10.1039/c3ee41165f.

(39) Landskron, K. Capacitance for Carbon Capture. *Angew. Chemie - Int. Ed.* **2018**, *57* (14), 3548–3550. https://doi.org/10.1002/anie.201800941.

(40) Rheinhardt, J. H.; Singh, P.; Tarakeshwar, P.; Buttry, D. A. Electrochemical Capture and Release of Carbon Dioxide. *ACS Energy Lett.* **2017**, *2* (2), 454–461. https://doi.org/10.1021/acsenergylett.6b00608.

(41) Yan Jing, Kiana Amini , Dawei Xi , Shijian Jin , Abdulrahman Alfaraidi , Emily Kerr , Roy Gordon, M. A. Electrochemically Induced CO2 Capture Enabled by Aqueous Quinone Flow Chemistry. *ChemRxiv* **2023**, 1–14.

(42) Environ, E.; Eisaman, M. D.; Alvarado, L.; Larner, D.; Wang, P.; Littau, K. A. CO2 Desorption Using High-Pressure Bipolar Membrane Electrodialysis. *Energy Environ. Sci.* **2011**, 4031–4037. https://doi.org/10.1039/c1ee01336j.

(43) Smith, W. A.; Burdyny, T.; Vermaas, D. A.; Geerlings, H. Pathways to Industrial-Scale Fuel Out of Thin Air from CO2 Electrolysis. *Joule* **2019**, *3* (8), 1822–1834. https://doi.org/10.1016/j.joule.2019.07.009.

(44) Stern, M. C. Electrochemically-Mediated Amine Regeneration for Carbon Dioxide Separations. *PhD Thesis* **2013**, 200.

(45) Legrand, L.; Schaetzle, O.; De Kler, R. C. F.; Hamelers, H. V. M. Solvent-Free CO2 Capture Using Membrane Capacitive Deionization. *Environ. Sci. Technol.* **2018**, *52* (16), 9478–9485. https://doi.org/10.1021/acs.est.8b00980.

(46) Legrand, L.; Shu, Q.; Tedesco, M.; Dykstra, J. E.; Hamelers, H. V. M. Role of Ion Exchange Membranes and Capacitive Electrodes in Membrane Capacitive Deionization (MCDI) for CO2 Capture. *J. Colloid Interface Sci.* **2020**, *564*, 478–490. https://doi.org/10.1016/j.jcis.2019.12.039.

(47) Huang, Z. H.; Yang, Z.; Kang, F.; Inagaki, M. Carbon Electrodes for Capacitive Deionization. *J.*

Mater. Chem. A **2017**, *5* (2), 470–496. https://doi.org/10.1039/c6ta06733f.

(48) Legrand, L. *Capacitive Processes for Carbon Capture and Energy Recovery from CO2 Emissions : Shaping a New Technology Going from Water to Gas Applications*; 2020.

(49) Conway, B. E. Transition from "supercapacitor" to "Battery" Behavior in Electrochemical Energy Storage. *Proc. Int. Power Sources Symp.* **1991**, 319–327. https://doi.org/10.1149/1.2085829.

(50) Miller, J. R. Introduction to Electrochemical Capacitor Technology. *IEEE Electr. Insul. Mag.* **2010**, *26* (4), 40–47. https://doi.org/10.1109/MEI.2010.5511188.

(51) Rightmire, R. A. Electrical Energy Storage Apparatus Patent. *US Pat.* **1966**.

(52) Boos, D. L.; Heights, G. Electrolytic Capactor Having Carbon Pasteelectrodes. *US Pat. 3536963* **1970**.

(53) Simon, P.; Gogotsi, Y.; Dunn, B. And Supercapacitors Begin ? *Science (80-.).* **2014**, *343* (March), 1210–1211.

(54) Zhang, S.; Zheng, M.; Tang, Y.; Zang, R.; Zhang, X.; Huang, X.; Chen, Y.; Yamauchi, Y.; Kaskel, S.; Pang, H. Understanding Synthesis – Structure – Performance Correlations of Nanoarchitectured Activated Carbons for Electrochemical Applications and Carbon Capture. *Adv. Funct. Mater.* **2022**, *2204714*, 1–59. https://doi.org/10.1002/adfm.202204714.

(55) Guan, L.; Yu, L.; Chen, G. Z. Capacitive and Non-Capacitive Faradaic Charge Storage. *Electrochim. Acta* **2016**, *206*, 464–478. https://doi.org/10.1016/j.electacta.2016.01.213.

(56) Mathis, T. S.; Kurra, N.; Wang, X.; Pinto, D.; Simon, P.; Gogotsi, Y. Energy Storage Data Reporting in Perspective—Guidelines for Interpreting the Performance of Electrochemical Energy Storage Systems. *Adv. Energy Mater.* **2019**, *9* (39), 1–13. https://doi.org/10.1002/aenm.201902007.

(57) Bilal, M. Improving the Multifunctionality of Structural Composites for Electrical Energy Storage. *Tech. Rep.* **2019**, No. August. https://doi.org/10.13140/RG.2.2.10457.34408.

(58) Kokoszka, B.; Jarrah, N. K.; Liu, C.; Moore, D. T.; Landskron, K. Supercapacitive Swing Adsorption of Carbon Dioxide. *Angew. Chemie - Int. Ed.* **2014**, *53* (14), 3698–3701. https://doi.org/10.1002/anie.201310308.

(59) Liu, J.-C.; Huang, Z.-H.; Ma, T.-Y. Aqueous Supercapacitor with Ultrahigh Voltage Window Beyond 2.0 Volt. *Small Struct.* **2020**, *1* (1), 2000020. https://doi.org/10.1002/sstr.202000020.

(60) Liu, C.; Landskron, K. Design, Construction, and Testing of a Supercapacitive Swing Adsorption Module for CO2 Separation. *Chem. Commun.* **2017**, *53* (26), 3661–3664. https://doi.org/10.1039/c7cc01055a.

(61) Zhu, S.; Ma, K.; Landskron, K. Relationships between the Charge-Discharge Methods and the Performance of a Supercapacitive Swing Adsorption Module for CO2 Separation. *J. Phys. Chem. C* **2018**, *122* (32), 18476–18483. https://doi.org/10.1021/acs.jpcc.8b03968.

(62) Zhu, S.; Li, J.; Toth, A.; Landskron, K. Relationships between Electrolyte Concentration and the Supercapacitive Swing Adsorption of CO2. *ACS Appl. Mater. Interfaces* **2019**. https://doi.org/10.1021/acsami.9b03598.

(63) Zhu, S.; Li, J.; Toth, A.; Landskron, K. Relationships between the Elemental Composition of Electrolytes and the Supercapacitive Swing Adsorption of CO2. *ACS Appl. Energy Mater.* **2019**, *2* (10), 7449–7456. https://doi.org/10.1021/acsaem.9b01435.

(64) Forghani, M.; Donne, S. W. Method Comparison for Deconvoluting Capacitive and Pseudo-Capacitive Contributions to Electrochemical Capacitor Electrode Behavior. *J. Electrochem. Soc.* **2018**, *165* (3), A664–A673. https://doi.org/10.1149/2.0931803jes.

(65) Gogotsi, Y.; Penner, R. M. Energy Storage in Nanomaterials - Capacitive, Pseudocapacitive, or Battery-Like? *ACS Nano*. American Chemical Society March 27, 2018, pp 2081–2083. https://doi.org/10.1021/acsnano.8b01914.

(66) Béguin, F.; Presser, V.; Balducci, A.; Frackowiak, E. Carbons and Electrolytes for Advanced Supercapacitors. *Adv. Mater.* **2014**, *26* (14), 2219–2251. https://doi.org/10.1002/adma.201304137.

(67) Zhang, S.; Pan, N. Supercapacitors Performance Evaluation. *Adv. Energy Mater.* **2015**, *5* (6). https://doi.org/10.1002/aenm.201401401.

(68) Mei, B. A.; Munteshari, O.; Lau, J.; Dunn, B.; Pilon, L. Physical Interpretations of Nyquist Plots for EDLC Electrodes and Devices. *J. Phys. Chem. C* **2018**, *122* (1), 194–206.

https://doi.org/10.1021/acs.jpcc.7b10582.

(69) MacDonald, D. D. Reflections on the History of Electrochemical Impedance Spectroscopy. *Electrochim. Acta* **2006**, *51* (8–9), 1376–1388. https://doi.org/10.1016/j.electacta.2005.02.107.

(70) Javaid, A.; Zafrullah, M. B.; Khan, F. ul H.; Bhatti, G. M. Improving the Multifunctionality of Structural Supercapacitors by Interleaving Graphene Nanoplatelets between Carbon Fibers and Solid Polymer Electrolyte. *J. Compos. Mater.* **2019**, *53* (10), 1401–1409. https://doi.org/10.1177/0021998318802622.

(71) Ko, J. S.; Sassin, M. B.; Rolison, D. R.; Long, J. W. Deconvolving Double-Layer, Pseudocapacitance, and Battery-like Charge-Storage Mechanisms in Nanoscale LiMn2O4 at 3D Carbon Architectures. *Electrochim. Acta* **2018**, *275*, 225–235. https://doi.org/10.1016/j.electacta.2018.04.149.

(72) Masarapu, C.; Zeng, H. F.; Hung, K. H.; Wei, B. Effect of Temperature on the Capacitance of Carbon Nanotube Supercapacitors. *ACS Nano* **2009**, *3* (8), 2199–2206. https://doi.org/10.1021/nn900500n.

(73) Taberna, P. L.; Simon, P.; Fauvarque, J. F. Electrochemical Characteristics and Impedance Spectroscopy Studies of Carbon-Carbon Supercapacitors. *J. Electrochem. Soc.* **2003**, *150* (3), A292. https://doi.org/10.1149/1.1543948.

(74) Ko, J. S.; Lai, C. H.; Long, J. W.; Rolison, D. R.; Dunn, B.; Nelson Weker, J. Differentiating Double-Layer, Psuedocapacitance, and Battery-like Mechanisms by Analyzing Impedance Measurements in Three Dimensions. *ACS Appl. Mater. Interfaces* **2020**, *12* (12), 14071–14078. https://doi.org/10.1021/acsami.0c02020.

(75) Qu, Y.; Baumann, T. F.; Santiago, J. G.; Stadermann, M. Characterization of Resistances of a Capacitive Deionization System. *Environ. Sci. Technol.* **2015**, *49* (16), 9699–9706. https://doi.org/10.1021/acs.est.5b02542.

(76) Zhang, Q.; Han, K.; Li, S.; Li, M.; Li, J.; Ren, K. Synthesis of Garlic Skin-Derived 3D Hierarchical Porous Carbon for High-Performance Supercapacitors. *Nanoscale* **2018**, *10* (5), 2427–2437.

https://doi.org/10.1039/c7nr07158b.

(77) Kumar, K. V.; Gadipelli, S.; Wood, B.; Ramisetty, K. A.; Stewart, A. A.; Howard, C. A.; Brett, D. J. L.; Rodriguez-Reinoso, F. Characterization of the Adsorption Site Energies and Heterogeneous Surfaces of Porous Materials. *J. Mater. Chem. A* **2019**, *7* (17), 10104–10137. https://doi.org/10.1039/c9ta00287a.

(78) Thommes, M.; Kaneko, K.; Neimark, A. V.; Olivier, J. P.; Rodriguez-Reinoso, F.; Rouquerol, J.; Sing, K. S. W. Physisorption of Gases, with Special Reference to the Evaluation of Surface Area and Pore Size Distribution (IUPAC Technical Report). *Pure Appl. Chem.* **2015**, *87* (9–10), 1051–1069. https://doi.org/10.1515/pac-2014-1117.

(79) Instrument Manual. Microactive Asap ® 2020 Accelerated Surface Area and Porosimetry System. **2019**, *2019*.

(80) Hulicova-Jurcakova, D.; Seredych, M.; Lu, G. Q.; Bandosz, T. J. Combined Effect of Nitrogen- and Oxygen-Containing Functional Groups of Microporous Activated Carbon on Its Electrochemical Performance in Supercapacitors. *Adv. Funct. Mater.* **2009**, *19* (3), 438–447. https://doi.org/10.1002/adfm.200801236.

(81) Frost, R. L.; Hales, M. C.; Wain, D. L. Raman Spectroscopy of Smithsonite. *J. Raman Spectrosc.* **2008**, *39* (1), 108–114. https://doi.org/10.1002/jrs.1835.

(82) Lindsey, R. If Carbon Dioxide Hits a New High Every Year, Why Isn't Every Year Hotter than the Last? *NOAA Clim.* **2021**, 3–7.

(83) Oschatz, M.; Antonietti, M. A Search for Selectivity to Enable CO2 Capture with Porous Adsorbents. *Energy Environ. Sci.* **2018**, *11* (1), 57–70. https://doi.org/10.1039/c7ee02110k.

(84) Balogun, H. A.; Bahamon, D.; AlMenhali, S.; Vega, L. F.; Alhajaj, A. Are We Missing Something When Evaluating Adsorbents for CO 2 Capture at the System Level? . *Energy Environ. Sci.* **2021**. https://doi.org/10.1039/d1ee01677f.

(85) Danaci, D.; Webley, P. A.; Petit, C. Guidelines for Techno-Economic Analysis of Adsorption Processes. *Front. Chem. Eng.* **2021**, *2* (January), 1–11. https://doi.org/10.3389/fceng.2020.602430.

(86) Luis, P. Use of Monoethanolamine (MEA) for CO2 Capture in a Global Scenario: Consequences and Alternatives. *Desalination* **2016**, *380*, 93–99. https://doi.org/10.1016/j.desal.2015.08.004.

(87) Zou, L.; Sun, Y.; Che, S.; Yang, X.; Wang, X.; Bosch, M.; Wang, Q.; Li, H.; Smith, M.; Yuan, S.; Perry, Z.; Zhou, H. C. Porous Organic Polymers for Post-Combustion Carbon Capture. *Adv. Mater.* **2017**, *29* (37). https://doi.org/10.1002/adma.201700229.

(88) Younas, M.; Sohail, M.; Kong, L. L.; Bashir, M. J. K.; Sethupathi, S. Feasibility of CO2adsorption by Solid Adsorbents: A Review on Low-Temperature Systems. *Int. J. Environ. Sci. Technol.* **2016**, *13* (7), 1839–1860. https://doi.org/10.1007/s13762-016-1008-1.

(89) Shao, H.; Wu, Y. C.; Lin, Z.; Taberna, P. L.; Simon, P. Nanoporous Carbon for Electrochemical Capacitive Energy Storage. *Chem. Soc. Rev.* **2020**, *49* (10), 3005–3039. https://doi.org/10.1039/d0cs00059k.

(90) Javaid, A.; Zafrullah, M. B.; Khan, F. ul H.; Bhatti, G. M. Improving the Multifunctionality of Structural Supercapacitors by Interleaving Graphene Nanoplatelets between Carbon Fibers and Solid Polymer Electrolyte. *J. Compos. Mater.* **2019**, *53* (10), 1401–1409. https://doi.org/10.1177/0021998318802622.

(91) Raj, A.; Alvi, S. M. A. A.; Islam, K.; Motalab, M.; Xu, S. An Atomistic Study of the Tensile Deformation of Carbon Nanotube–Polymethylmethacrylate Composites. *Polymers (Basel).* **2023**, *15* (13). https://doi.org/10.3390/polym15132956.

(92) Hemmatifar, A.; Kang, J. S.; Ozbek, N.; Tan, K. J.; Hatton, T. A. Electrochemically Mediated Direct CO2 Capture by a Stackable Bipolar Cell. *ChemSusChem* **2022**, *15* (6). https://doi.org/10.1002/cssc.202102533.

(93) Youn, M. H.; Park, K. T.; Lee, Y. H.; Kang, S.; Lee, S. M.; Kim, S. S. Carbon Dioxide Sequestration Process for the Cement Industry. *J. CO2 Util.* **2019**, *34* (July), 325–334. https://doi.org/10.1016/j.jcou.2019.07.023.

(94) Rahimi, M.; Catalini, G.; Hariharan, S.; Wang, M.; Puccini, M.; Hatton, T. A. Carbon Dioxide Capture Using an Electrochemically Driven Proton Concentration Process. *Cell Reports Phys. Sci.*

2020, *1* (4), 100033. https://doi.org/10.1016/j.xcrp.2020.100033.

(95) Binford, T. B.; Mapstone, G.; Temprano, I.; Forse, A. C. Enhancing the Capacity of Supercapacitive Swing Adsorption CO2 Capture by Tuning Charging Protocols. *Nanoscale* **2022**. https://doi.org/10.1039/D2NR00748G.

(96) Ji, T.; Han, K.; Teng, Z.; Li, J.; Wang, M.; Zhang, J.; Cao, Y.; Qi, J. Synthesis of Activated Carbon Derived from Garlic Peel and Its Electrochemical Properties. *Int. J. Electrochem. Sci.* **2021**, *16* (1), 1–14. https://doi.org/10.20964/2021.01.61.

(97) Gogotsi, Y.; Nikitin, A.; Ye, H.; Zhou, W.; Fischer, J. E.; Yi, B.; Foley, H. C.; Barsoum, M. W. Nanoporous Carbide-Derived Carbon with Tunable Pore Size. *Nat. Mater.* **2003**, *2* (9), 591–594. https://doi.org/10.1038/nmat957.

(98) Grady, T. M. O.; Arthur, G.; Mcclain, W. T. United States Patent (19). **1978**, *4* (19).

(99) Data. BPL ® 4x6. *Calgon Caron* **2015**, 2015.

(100) Zhu, S.; Li, J.; Toth, A.; Landskron, K. Relationships between Electrolyte Concentration and the Supercapacitive Swing Adsorption of CO2. *ACS Appl. Mater. Interfaces* **2019**, 1–17. https://doi.org/10.1021/acsami.9b03598.

(101) Miao, L.; Duan, H.; Zhu, D.; Lv, Y.; Gan, L.; Li, L.; Liu, M. Boron "Gluing" Nitrogen Heteroatoms in a Prepolymerized Ionic Liquid-Based Carbon Scaffold for Durable Supercapacitive Activity. *J. Mater. Chem. A* **2021**, *9* (5), 2714–2724. https://doi.org/10.1039/d0ta09985f.

(102) S.Ardizzone, G. F.; S.Trasatti. "Inner" and "Outer" Active Surface of RuO2 Electrodes. *Electrochim. Acta* **1990**, *35* (1), 263–267. https://doi.org/10.1109/icdm.2002.1184004.

(103) Zhang, C.; He, D.; Ma, J.; Tang, W.; Waite, T. D. Faradaic Reactions in Capacitive Deionization (CDI) - Problems and Possibilities: A Review. *Water Res.* **2018**, *128*, 314–330. https://doi.org/10.1016/j.watres.2017.10.024.

(104) Xiao, J.; Wang, Y.; Zhang, T. C.; Ouyang, L.; Yuan, S. Phytic Acid-Induced Self-Assembled Chitosan Gel-Derived N, P–Co-Doped Porous Carbon for High-Performance CO2 Capture and Supercapacitor. *J. Power Sources* **2022**, *517* (November 2021), 230727.

https://doi.org/10.1016/j.jpowsour.2021.230727.

(105) Yuan, X.; Xiao, J.; Yılmaz, M.; Zhang, T. C.; Yuan, S. N, P Co-Doped Porous Biochar Derived from Cornstalk for High Performance CO2 Adsorption and Electrochemical Energy Storage. *Sep. Purif. Technol.* **2022**, *299* (July), 121719. https://doi.org/10.1016/j.seppur.2022.121719.

(106) Song, G.; Romero, C.; Lowe, T.; Driscoll, G.; Kreglow, B.; Schobert, H.; Baltrusaitis, J.; Yao, Z. Multistage Activation of Anthracite Coal-Based Activated Carbon for High-Performance Supercapacitor Applications. *Energy and Fuels* **2023**, *37* (2), 1327–1343. https://doi.org/10.1021/acs.energyfuels.2c03487.

(107) Tang, W.; He, D.; Zhang, C.; Kovalsky, P.; Waite, T. D. Comparison of Faradaic Reactions in Capacitive Deionization (CDI) and Membrane Capacitive Deionization (MCDI) Water Treatment Processes. *Water Res.* **2017**, *120*, 229–237. https://doi.org/10.1016/j.watres.2017.05.009.

(108) Dykstra, J. E.; Keesman, K. J.; Biesheuvel, P. M.; van der Wal, A. Theory of PH Changes in Water Desalination by Capacitive Deionization. *Water Res.* **2017**, *119*, 178–186. https://doi.org/10.1016/j.watres.2017.04.039.

(109) He, Y.; Zhang, Y.; Li, X.; Lv, Z.; Wang, X.; Liu, Z.; Huang, X. Capacitive Mechanism of Oxygen Functional Groups on Carbon Surface in Supercapacitors. *Electrochim. Acta* **2018**, *282*, 618–625. https://doi.org/10.1016/j.electacta.2018.06.103.

(110) Bilal, M.; Li, J.; Guo, H.; Landskron, K. High-Voltage Supercapacitive Swing Adsorption of Carbon Dioxide. *Small* **2023**, *2207834*, 2207834. https://doi.org/10.1002/smll.202207834.

(111) NWE contributors. List of Countries by Garlic Production. *New World Encycl.* **2020**, 1–7.

(112) Rahman, M. M.; Hossain, M.; Rahman, M. H.; Rahim, M. A.; Islam, M. T. Growth and Yield Performance of Garlic Varieties under Zero-Tillage and Tillage System. *Int. J. Hortic. Sci.* **2020**, *26*, 46–54. https://doi.org/10.31421/ijhs/26/2020/6065.

(113) Heidarinejad, Z.; Dehghani, M. H.; Heidari, M.; Javedan, G.; Ali, I.; Sillanpää, M. Methods for Preparation and Activation of Activated Carbon: A Review. *Environ. Chem. Lett.* **2020**, *18* (2), 393–415. https://doi.org/10.1007/s10311-019-00955-0.

(114) Le, M.; Silva, J.; Carrasco, S.; Barrientos, N. Design , Cost Estimation and Sensitivity Analysis for a Production Process of Activated Carbon from Waste Nutshells by Physical Activation. **2020**.

(115) Hand, S.; Guest, J. S.; Cusick, R. D. Technoeconomic Analysis of Brackish Water Capacitive Deionization: Navigating Tradeoffs between Performance, Lifetime, and Material Costs. *Environ. Sci. Technol.* **2019**, *53* (22), 13353–13363. https://doi.org/10.1021/acs.est.9b04347.

(116) Metzger, M.; Besli, M. M.; Kuppan, S.; Hellstrom, S.; Kim, S.; Sebti, E.; Subban, C. V.; Christensen, J. Techno-Economic Analysis of Capacitive and Intercalative Water Deionization. *Energy Environ. Sci.* **2020**, *13* (6), 1544–1560. https://doi.org/10.1039/d0ee00725k.

(117) Price, G. Https://Www.Alibaba.Com//Trade/Search?Fsb=y&IndexArea=product_en&CatId=&tab=all&SearchText=gluten+price+per+Kg. 1–11.

(118) Carlson, E.J.; Kopf, K.; Sinha, S. Cost Analysis of PEM Fuel Cell Systems for Transportation. Subcontract Report NREL/SR-560-39104. **2005**, No. December.

(119) Evanko, B.; Yoo, S. J.; Lipton, J.; Chun, S. E.; Moskovits, M.; Ji, X.; Boettcher, S. W.; Stucky, G. D. Stackable Bipolar Pouch Cells with Corrosion-Resistant Current Collectors Enable High-Power Aqueous Electrochemical Energy Storage. *Energy Environ. Sci.* **2018**, *11* (10), 2865–2875. https://doi.org/10.1039/c8ee00546j.

(120) Pamela Porter and David Laird. Biochar: Prospects of Commercialization. *https://farm-energy.extension.org/biochar-prospects-of-commercialization/* **2014**, *2014* (20141031), 1–12.

(121) U.S. Department of Energy. DOE / NETL CARBON CAPTURE PROGRAM R & D COMPENDIUM of CARBON CAPTURE. **2015**, No. July.

(122) Xia, Y.; Feng, Y.; Shakouri, M.; Yoon, J.; Kim, T.; Fang, Z. Continuous Carbon Capture in an Electrochemical Solid-Electrolyte Reactor. *Nature* **2023**, *618* (May 2022). https://doi.org/10.1038/s41586-023-06060-1.

(123) Shi, L.; Zhao, Y.; Matz, S.; Gottesfeld, S.; Setzler, B. P.; Yan, Y. A Shorted Membrane Electrochemical Cell Powered by Hydrogen to Remove CO2 from the Air Feed of Hydroxide

Exchange Membrane Fuel Cells. *Nat. Energy* **2022**. https://doi.org/10.1038/s41560-021-00969-5.

(124) Tang, J.; Yuan, H.; Duan, Q.; Liu, Y.; Wang, Y.; Yuan, S. Phosphorus-Functionalized Low-Crystallinity Transition-Metal Oxide Nanorod Arrays Grown on Carbon Cloth for High-Performance Asymmetric Supercapacitors. *Colloids Surfaces A Physicochem. Eng. Asp.* **2022**, *654* (September), 130189. https://doi.org/10.1016/j.colsurfa.2022.130189.

(125) Yang, C.; Jiang, K.; Zheng, Q.; Li, X.; Mao, H.; Zhong, W.; Chen, C.; Sun, B.; Zheng, H.; Zhuang, X.; Reimer, J. A.; Liu, Y.; Zhang, J. Chemically Stable Polyarylether-Based Metallophthalocyanine Frameworks with High Carrier Mobilities for Capacitive Energy Storage. *J. Am. Chem. Soc.* **2021**, *143* (42), 17701–17707. https://doi.org/10.1021/jacs.1c08265.

(126) Lee, Y. H.; Chang, K. H.; Hu, C. C. Differentiate the Pseudocapacitance and Double-Layer Capacitance Contributions for Nitrogen-Doped Reduced Graphene Oxide in Acidic and Alkaline Electrolytes. *J. Power Sources* **2013**, *227*, 300–308. https://doi.org/10.1016/j.jpowsour.2012.11.026.

(127) Lee, J. S. M.; Briggs, M. E.; Hu, C. C.; Cooper, A. I. Controlling Electric Double-Layer Capacitance and Pseudocapacitance in Heteroatom-Doped Carbons Derived from Hypercrosslinked Microporous Polymers. *Nano Energy* **2018**, *46* (December 2017), 277–289. https://doi.org/10.1016/j.nanoen.2018.01.042.

(128) Biswal, M.; Banerjee, A.; Deo, M.; Ogale, S. From Dead Leaves to High Energy Density Supercapacitors. *Energy Environ. Sci.* **2013**, *6* (4), 1249–1259. https://doi.org/10.1039/c3ee22325f.

(129) Guo, N.; Luo, W.; Guo, R.; Qiu, D.; Zhao, Z.; Wang, L.; Jia, D.; Guo, J. Interconnected and Hierarchical Porous Carbon Derived from Soybean Root for Ultrahigh Rate Supercapacitors. *J. Alloys Compd.* **2020**, *834*, 155115. https://doi.org/10.1016/j.jallcom.2020.155115.

(130) Zhang, Y.; Gao, H.; Song, X.; Kong, X.; Xu, H. Preparation of Hierarchical Porous Carbon from Wheat Bran for Free-Standing Electrode of High Areal Capacitance Supercapacitor. *ChemElectroChem* **2019**, *6* (21), 5486–5491. https://doi.org/10.1002/celc.201901440.

(131) Wang, C.; Xiong, Y.; Wang, H.; Sun, Q. All-Round Utilization of Biomass Derived All-Solid-State

Asymmetric Carbon-Based Supercapacitor. *J. Colloid Interface Sci.* **2018**, *528*, 349–359. https://doi.org/10.1016/j.jcis.2018.05.103.

(132) Li, H.; Yuan, D.; Tang, C.; Wang, S.; Sun, J.; Li, Z.; Tang, T.; Wang, F.; Gong, H.; He, C. Lignin-Derived Interconnected Hierarchical Porous Carbon Monolith with Large Areal/Volumetric Capacitances for Supercapacitor. *Carbon N. Y.* **2016**, *100*, 151–157. https://doi.org/10.1016/j.carbon.2015.12.075.

(133) Pérez-Rodríguez, S.; Pinto, O.; Izquierdo, M. T.; Segura, C.; Poon, P. S.; Celzard, A.; Matos, J.; Fierro, V. Upgrading of Pine Tannin Biochars as Electrochemical Capacitor Electrodes. *J. Colloid Interface Sci.* **2021**, *601*, 863–876. https://doi.org/10.1016/j.jcis.2021.05.162.

(134) Choi, J. H.; Kim, Y.; Kim, B. su. Multifunctional Role of Reduced Graphene Oxide Binder for High Performance Supercapacitor with Commercial-Level Mass Loading. *J. Power Sources* **2020**, *454* (November 2019), 227917. https://doi.org/10.1016/j.jpowsour.2020.227917.

(135) Yang, X.; Lv, T.; Qiu, J. High Mass-Loading Biomass-Based Porous Carbon Electrodes for Supercapacitors: Review and Perspectives. *Small* **2023**, *19* (22), 1–32. https://doi.org/10.1002/smll.202300336.

(136) Cohen, I.; Avraham, E.; Noked, M.; Soffer, A.; Aurbach, D. Enhanced Charge Efficiency in Capacitive Deionization Achieved by Surface-Treated Electrodes and by Means of a Third Electrode. *J. Phys. Chem. C* **2011**, *115* (40), 19856–19863. https://doi.org/10.1021/jp206956a.

(137) Bilal, M.; Li, J.; Landskron, K. Activated Carbon Electrodes with Improved Sorption Capacity for Supercapacitive Swing Adsorption of Carbon Dioxide. *chemrxiv* **2022**.

(138) Guo, W.; Yu, C.; Li, S.; Qiu, J. Toward Commercial-Level Mass-Loading Electrodes for Supercapacitors: Opportunities, Challenges and Perspectives. *Energy Environ. Sci.* **2021**, *14* (2), 576–601. https://doi.org/10.1039/d0ee02649b.

(139) Khuong, D. A.; Trinh, K. T.; Nakaoka, Y.; Tsubota, T.; Tashima, D.; Nguyen, H. N.; Tanaka, D. The Investigation of Activated Carbon by K2CO3 Activation: Micropores- and Macropores-Dominated Structure. *Chemosphere* **2022**, *299* (March), 134365.

https://doi.org/10.1016/j.chemosphere.2022.134365.

(140) Hsieh, C. T.; Teng, H. Influence of Oxygen Treatment on Electric Double-Layer Capacitance of Activated Carbon Fabrics. *Carbon N. Y.* **2002**, *40* (5), 667–674. https://doi.org/10.1016/S0008-6223(01)00182-8.

(141) Qian, W.; Sun, F.; Xu, Y.; Qiu, L.; Liu, C.; Wang, S.; Yan, F. Human Hair-Derived Carbon Flakes for Electrochemical Supercapacitors. *Energy Environ. Sci.* **2014**, *7* (1), 379–386. https://doi.org/10.1039/c3ee43111h.

(142) Y. Pocker and D. W. Bjorkquist. Stopped-Flow Studies of Carbon Dioxide Hydration and Bicarbonate Dehydration in H2O and D2O. Acid-Base and Metal Ion Catalysis. *J. Am. Chem. Soc.* **1976**, No. 3, 6537–6543.

(143) Gao, Q.; Demarconnay, L.; Raymundo-Piñero, E.; Béguin, F. Exploring the Large Voltage Range of Carbon/Carbon Supercapacitors in Aqueous Lithium Sulfate Electrolyte. *Energy Environ. Sci.* **2012**, *5* (11), 9611–9617. https://doi.org/10.1039/c2ee22284a.

(144) Ratajczak, P.; Jurewicz, K.; Béguin, F. Factors Contributing to Ageing of High Voltage Carbon/Carbon Supercapacitors in Salt Aqueous Electrolyte. *J. Appl. Electrochem.* **2014**, *44* (4), 475–480. https://doi.org/10.1007/s10800-013-0644-0.

(145) He, M.; Fic, K.; Frackowiak, E.; Novák, P.; Berg, E. J. Ageing Phenomena in High-Voltage Aqueous Supercapacitors Investigated by in Situ Gas Analysis. *Energy Environ. Sci.* **2016**, *9* (2), 623–633. https://doi.org/10.1039/c5ee02875b.

(146) Przygocki, P.; Ratajczak, P.; Béguin, F. Quantification of the Charge Consuming Phenomena under High-Voltage Hold of Carbon/Carbon Supercapacitors by Coupling Operando and Post-Mortem Analyses. *Angew. Chemie* **2019**, *131* (50), 18137–18145. https://doi.org/10.1002/ange.201907914.

(147) Shao, Y.; El-Kady, M. F.; Sun, J.; Li, Y.; Zhang, Q.; Zhu, M.; Wang, H.; Dunn, B.; Kaner, R. B. Design and Mechanisms of Asymmetric Supercapacitors. *Chem. Rev.* **2018**, *118* (18), 9233–9280. https://doi.org/10.1021/acs.chemrev.8b00252.

(148) Bilal, M.; Li, J.; Landskron, K. Enhancing Supercapacitive Swing Adsorption of CO 2 with

Advanced Activated Carbon Electrodes. *Adv. Sustain. Syst.* **2023**, *2300250*, 1–13. https://doi.org/10.1002/adsu.202300250.

(149) Li, J.; Bilal, M.; Landskron, K. Scaling Supercapacitive Swing Adsorption of CO2 Using Bipolar Electrode Stacks. *ChemRxiv* **2016**, 1–23.

(150) Xu, Z.; Mapstone, G.; Coady, Z.; Wang, M.; Spreng, T. L.; Liu, X.; Forse, A. C.; Hamied, Y. Impacts of Supercapacitor Electrode Structure on Electrochemical CO2 Capture. *chemrxiv* **2024**. https://doi.org/10.26434/chemrxiv-2023-nj817.

(151) Kang, J. S.; Kim, S.; Kang, J.; Joo, H.; Jang, J.; Jo, K.; Park, S.; Kim, H.; Yoo, S. J.; Yoon, J.; Sung, Y.; Hatton, T. A. Surface Electrochemistry of Carbon Electrodes and Faradaic Reactions in Capacitive Deionization. *Environ. Sci. Technol.* **2022**. https://doi.org/10.1021/acs.est.2c03913.

(152) Dyatkin, B.; Zhang, Y.; Mamontov, E.; Kolesnikov, A. I.; Cheng, Y.; Meyer, H. M.; Cummings, P. T.; Gogotsi, Y. Influence of Surface Oxidation on Ion Dynamics and Capacitance in Porous and Nonporous Carbon Electrodes. *J. Phys. Chem. C* **2016**, *120* (16), 8730–8741. https://doi.org/10.1021/acs.jpcc.6b01204.

(153) Kang, J. S.; Kim, S.; Chung, D. Y.; Son, Y. J.; Jo, K.; Su, X.; Lee, M. J.; Joo, H.; Hatton, T. A.; Yoon, J.; Sung, Y. E. Rapid Inversion of Surface Charges in Heteroatom-Doped Porous Carbon: A Route to Robust Electrochemical Desalination. *Adv. Funct. Mater.* **2019**. https://doi.org/10.1002/adfm.201909387.

(154) Yong, J. K. J.; Stevens, G. W.; Caruso, F.; Kentish, S. E. The Use of Carbonic Anhydrase to Accelerate Carbon Dioxide Capture Processes. *J. Chem. Technol. Biotechnol.* **2015**, *90* (1), 3–10. https://doi.org/10.1002/jctb.4502.

(155) Jin, C.; Zhang, S.; Zhang, Z.; Chen, Y. Mimic Carbonic Anhydrase Using Metal-Organic Frameworks for CO2 Capture and Conversion. *Inorg. Chem.* **2018**, *57* (4), 2169–2174. https://doi.org/10.1021/acs.inorgchem.7b03021.

(156) Ochedi, F. O.; Yu, J.; Yu, H.; Liu, Y.; Hussain, A. Carbon Dioxide Capture Using Liquid Absorption Methods: A Review. *Environmental Chemistry Letters*. Springer Science and Business

Media Deutschland GmbH February 1, 2021, pp 77–109. https://doi.org/10.1007/s10311-020-01093-8.

(157) Lukatskaya, M. R.; Kota, S.; Lin, Z.; Zhao, M. Q.; Shpigel, N.; Levi, M. D.; Halim, J.; Taberna, P. L.; Barsoum, M. W.; Simon, P.; Gogotsi, Y. Ultra-High-Rate Pseudocapacitive Energy Storage in Two-Dimensional Transition Metal Carbides. *Nat. Energy* **2017**, *6* (July), 1–6. https://doi.org/10.1038/nenergy.2017.105.

(158) Chen, W.; Gu, J.; Liu, Q.; Yang, M.; Zhan, C.; Zang, X.; Pham, T. A.; Liu, G.; Zhang, W.; Zhang, D.; Dunn, B.; Morris Wang, Y. Two-Dimensional Quantum-Sheet Films with Sub-1.2 Nm Channels for Ultrahigh-Rate Electrochemical Capacitance. *Nat. Nanotechnol.* **2021**. https://doi.org/10.1038/s41565-021-01020-0.

(159) Li, Z.; Gadipelli, S.; Li, H.; Howard, C. A.; Brett, D. J. L.; Shearing, P. R.; Guo, Z.; Parkin, I. P.; Li, F. Tuning the Interlayer Spacing of Graphene Laminate Films for Efficient Pore Utilization towards Compact Capacitive Energy Storage. *Nat. Energy* **2020**, *5* (2), 160–168. https://doi.org/10.1038/s41560-020-0560-6.

(160) Yao, B.; Chandrasekaran, S.; Zhang, J.; Xiao, W.; Qian, F.; Zhu, C.; Duoss, E. B.; Spadaccini, C. M.; Worsley, M. A.; Li, Y. Efficient 3D Printed Pseudocapacitive Electrodes with Ultrahigh MnO 2 Loading. *Joule* **2019**, *3* (2), 459–470. https://doi.org/10.1016/j.joule.2018.09.020.

Muhammad Bilal

linkedin.com/in/bilal947
bilal.zafarullah947@gmail.com
484 666 7290
Bethlehem, PA

OBJECTIVE

A passionate Ph.D. Chemist specializing in electrochemistry and materials science, driven to propel advancements in energy storage and CO_2 capture through pioneering research and technology development.

EDUCATION

Lehigh University, Dept. of Chemistry Bethlehem, PA
Ph.D. in Chemistry (GPA: 3.64/4.00, concentration: electrochemistry) Aug 2020–May 2024

Hokkaido University, Dept. of Materials Science and Engineering Hokkaido, Japan
M.S in Materials Science and Engineering (GPA: 3.90/4.00, concentration: electrochemistry) Aug 2018–July 2020

University of Engineering and Technology Lahore, Faculty of Chemical Engineering Lahore, Pakistan
B.S in Polymer and Process Engineering (GPA: 3.65/4.00, concentration: materials chemistry) Aug 2013–June 2017

WORK EXPERIENCE

Graduate Researcher Lehigh University, 2020–2024

Dissertation Project: Development of high-performance supercapacitors for energy storage and CO_2 capture.

- Synthesized activated carbon-based electrodes from biomass, coke, coal, and carbide sources. Developed supercapacitive swing adsorption modules for simultaneous energy storage and CO_2 capture with 10 times improved sorption performance than previously investigated materials.
- Electrochemically characterized organic (carbon-based) and inorganic (metal-oxide) electrode materials using cyclic voltammetry (CV), electrochemical impedance spectroscopy (EIS), and galvanostatic/potentiostatic charge-discharge tests for quantitative analysis of the energetic performance.
- Performed techno-economic analysis of the optimized supercapacitive swing adsorption (SSA) to demonstrate its commercialization potential and identified key requirements to reduce the cost to $40/ton CO_2 captured compared to existing technologies costing more than $100/ton.

Secondary Projects:

- Developed and characterized metal organic framework (MOF) supercapacitors with superior volumetric energy.
- Developed and characterized fuel cell electrocatalysts for anodic oxidation and cathodic reduction reactions.

Master's Research Hokkaido University, 2018–2020

Dissertation Project: High-throughput electrochemical fabrication of localized surface patterns using 3D printed solution flow type microdroplet cells.

- Designed and fabricated 3D printed electrochemical flow cells for localized anodizing and electrodeposition of metals, offering faster and precise formation of localized surface patterns compared to previously existing methods.

Undergraduate Research University of Engineering and Technology, 2013–2017

Final year project: Development of multifunctional nanocomposites for electrochemical energy storage.

- Developed graphene, carbon fiber, and solid polymer electrolyte-based nanocomposite supercapacitors for load-bearing applications. Mechanical (UTM, DMTA), electrochemical (CV, EIS, CCD), and surface characterizations (FTIR, TGA, DSC) indicated greatly improved performance compared to previous state of the art.

INDUSTRIAL EXPERIENCE

Business Development Engineer Bin Rasheed Colors and Chemicals Mfg. Ltd., 2017–2018

- Applied engineering knowledge to analyze processing and post-processing issues faced by customers during Injection molding, blow molding, rotomolding, and extrusion of their plastic products. Provided solutions to the clients facing processing issues by recommending the accurate percentage of additives and setting up optimized processing parameters. Conducted around 100 on-site trails at our customers' facilities.
- Analyzed the masterbatch market potential of the company in different application areas, held telephonic and in-person meetings on daily basis with new and existing customers. Market analysis, networking with potential customers and adding new customers eventually led to about 10 % increase in the company's annual masterbatch sales.

Sales Engineer Diversey, 2018

- Provided building, floor, kitchen, and personal care chemicals to 50 plus clients withing Pakistan.

RESEARCH SKILLS

Materials Synthesis: inorganic, organic, electrochemical, nanoscale
Materials Characterization: SEM, EDX, XPS, XRD, UV-Vis, FTIR, Raman, BET, CV, EIS, GCD, LSV, Tafel**,** TGA, DSC, DMTA
Data Analysis, 3D Design, and coding: MS-Office, Excel, Origin, Igor Pro, Blender, Solidworks, Matlab

LEADERSHIP, AWARDS & FELLLOWSHIPS

- **Teaching Assistant** *(Organic chemistry, Physical chemistry, Chemical principles, and Equilibria)* Bethlehem, PA, 2020-23
- **Japanese Government Fellowship** *(MEXT Super Global University Award)* Hokkaido, Japan, 2018-20
- **Gold Medal Award** *(for best overall performance in undergraduate studies)* Lahore, Pakistan, 2017

ORAL & POSTER PRESENTATIONS

- 243rd ECS Meeting with the 18th International Symposium on Solid Oxide Fuel Cells (SOFC-XVIII) Spring 2023
- Lehigh Materials Symposium, Institute for Functional Materials and Devices (I-FMD) Spring 2023
- 26th Northeast Corridor Zeolite Association meeting in Philadelphia Fall 2022
- The Electrochemical Society of Japan Fall 2020 meeting Fall 2020
- 100th Japan Chemical Society (CSJ) Annual Meeting Spring 2020
- The Electrochemical Society of Japan Fall 2019 meeting Fall 2019

PUBLICATIONS *(Google scholar)*

1. ***Chemrxiv***, 2024 10.26434/chemrxiv-2024-z6966
2. ***Small***, 2207834 (2023) https://doi.org/10.1002/smll.202207834
3. ***Advanced Sustainable Systems***, 2300250 (2023) https://doi.org/10.1002/adsu.202300250
4. ***Chemrxiv***, 2023 10.26434/chemrxiv-2023-62xjd
5. ***Journal of The Electrochemical Society,*** 168 061505 (2021) https://doi.org/10.1149/1945-7111/ac07c1
6. ***Materials Today Communications***, 26 (2021) 102053 https://doi.org/10.1016/j.mtcomm.2021.102053
7. ***Journal of Advanced Research***, 26 (2020) 43-51 https://doi.org/10.1016/j.jare.2020.06.019
8. ***Journal of The Electrochemical Society***, 167 081501(2020) https://doi.org/10.1149/1945-7111/ab8877
9. ***Journal of Composite Materials***, 53 (2018) 1401-1409 https://doi.org/10.1177/0021998318802622

MEDIA HIGHLIGHTS

1. Garlic root electrodes show promise for efficient and cost-effective carbon capture, Chemistry and Industry.

2. Supercharging Carbon Dioxide Capture, Advanced Science News.